UNIVERSITY OF SOUTHAMPTON

FACULTY OF ENGINEERING AND PHYSICAL SCIENCES

SCHOOL OF CHEMISTRY

Transient Studies of Oxygen Species Adsorbed on Platinum Microelectrodes

by

Oliver Rodríguez Martínez

Thesis for the degree of Doctor of Philosophy

September 2019

UNIVERSITY OF SOUTHAMPTON

Abstract

Faculty of Engineering and Physical Sciences

School of Chemistry

Thesis for the degree of Doctor of Philosophy

Transient Studies of Oxygen Species Adsorbed on Platinum Microelectrodes

by

Oliver Rodríguez Martínez

Perry and Denuault reported the presence of an oxygen species that adsorbed on Pt microelectrodes after the electrode was exposed to dissolved oxygen [1, 2, 3]. This species could only be detected at the millisecond scale and when using a neutral and unbuffered media. Although they suggested that the species was oxygenated in nature, its true identity and relation with O_2 remained unknown. In the present work, the species were studied with the use of Pt microelectrodes of different sizes, in different electrolytes and with sampled current voltammetry and scanning electrochemical microscopy. The results show strong evidence that the adsorbed species are oxides formed under a higher local *p*H, where OH^- is being produced by the oxygen reduction reaction proceeding through the alkaline path. This was observed by exploiting hindered diffusion in the presence of O_2, where the oxide formation region appeared as a continuous wave, similar to results in bulk alkaline media. Furthermore, a diffusion controlled oxidation wave appeared that was limited by the local concentration of OH^-. Throughout this work, sampled current voltammetry was exploited to study the oxygen reduction reaction and the reduction of adsorbed oxygen species, and as such, methodologies to obtain kinetic information were proposed. An equivalent Koutecky-Levich analysis was applied to sampled current voltammograms of the oxygen reduction reaction, obtaining Tafel slopes similar to those reported in the literature, and an analytical solution for sampled current voltammograms of adsorbed species in the absence of diffusion was also derived; comparison with established methodologies is also presented.

Contents

List of Figures

List of Tables

Research Thesis: Declaration of Authorship

Oliver Rodríguez Martínez

Transient Studies of Oxygen Species Adsorbed on Platinum Microelectrodes

I declare that this thesis and the work presented in it are my own and has been generated by me as the result of my own original research.

I confirm that:

1. This work was done wholly or mainly while in candidature for a research degree at this University;
2. Where any part of this thesis has previously been submitted for a degree or any other qualification at this University or any other institution, this has been clearly stated;
3. Where I have consulted the published work of others, this is always clearly attributed;
4. Where I have quoted from the work of others, the source is always given. With the exception of such quotations, this thesis is entirely my own work;
5. I have acknowledged all main sources of help;
6. Where the thesis is based on work done by myself jointly with others, I have made clear exactly what was done by others and what I have contributed myself;
7. None of this work has been published before submission

Signed:

Date:

Acknowledgements

On the shoulders of giants. - Sir Isaac Newton

Several people and organisations have contributed in one way or another to this work. Here, I am acknowledging those who were directly involved.

- To Dr. Guy Denuault for showing me the secrets of Electrochemistry, for his patiance and guidance as my PhD Supervisor and specially, for believing in me by giving me the oportunity to be part of his group. I will allways be grateful.
- To CONACYT and I2T2 for the scolaship given to pursue a PhD.
- To Prof. Andrew Hector, Prof. Andrea Russell and Prof. Philip Bartlett for following my development through my PhD and for many useful discussions.
- To Prof. Robert Forster and Dr. Nuria Garcia-Araez for accepting being my examiners, hoping that you find my work valuable.
- To Prof. Peter Smith for allowing me to use his lab to construct nanoelectrodes.
- To Prof. Mauro Bertotti and Prof. Marcelo Videa and their groups for the research collaborations and discussions about the work.
- To past and present members of the Denuault group that helped me greatly improve my knowledge in Electrochemistry: Tammy Nimmo, Cybelle Soares, Steven Linfield, Ana Perdomo, Saiful Shafiee and Samuel Perry.
- To the students, also part of the Denuault group, that I have had the honour helping with their dissertations: Felix Liew, Carloyn Gustin, Natasha Macfadyen, Zoe Gurnah, Samuel Toft, Francesc Valls and Maria Paula Salinas.
- To future students of the Denuault group, hoping that you can use my work as I have done with other's.
- To my family, Jesus, Ana and Xiomara for always being there for me.
- To RSC, ECS, FAPESP and Newton funds that allowed me to travel around the world doing Electrochemistry.

Symbols and acronyms

α Transfer coefficient

ΔH_{soln} Dissolution enthalpy of oxygen

ϵ Adimensional potential, $\epsilon = \exp(nF\eta/RF)$

η Overpotential, $\eta = E$ - E^0

Γ_{O}, Γ_{R} Coverage of O or R

Γ^0_{O}, Γ^0_{R} Initial coverage of the species

Γ^t_{O}, Γ^t_{R} Transient coverage of the species

κ Conductivity of the solution

ν Scan rate

ω Rotation speed

ϕ Diameter

σ Adimensional time, $\sigma = Dta^{-2}$

τ Characteristic time of a pseudo-capacitor

τ Sampling time

A Area of the electrode

a	Radius of a disc
C	Concentration
C_d	Double layer capacitance
C_{760}	Saturation concentration of O_2 at 760 mmHg
D	Diffusion coefficient
E	Potential applied
E_k	Onset potential
E_r	Rest potential
E_s	Step potential
E_{peak}	Peak potential
F	Faraday constant, $F = 96485$ C mol^{-1}
I	Normalised current for SECM approach curves, $I = i_{lim}/i_{bulk}$
i	Current
i_k	Kinetic current
i_{lim}	Limiting current
j^0	Initial current density
j_{peak}	Peak current density
K	Rate constant, $K = k_f + k_b$
k	Rate constant
k_b	Backward rate constant

k_f	Forward rate constant
k_H	Henry law constant
k_i	Tabulated parameters for the approach curves
k_m	Mass transfer coefficient
k_s	Standard rate constant
L	Normalised tip-substrate distance, $L = d/a$
N	Viscosity of solution
n	Number of electrons
n_{app}	Apparent number of electrons
P	Pressure
P_{atm}	Atmospheric pressure
P_{H2O}	Partial pressure of water vapour
Q	Charge density
Q^0	Initial charge
Q_{lim}	Limiting charge
R	Gas constant, $R = 8.314$ J mol^{-1} K^{-1}
r	Radius of a sphere
R_f	Roughness factor
R_s, R_u	Solution resistance
T	Temperature, $T = 298$ K

t Time

t_s Time step

x Distance between Luggin capillary and working electrode

X, Y, Z Micropositioner axis

CA Chronoamperometry, chronoamperogram

CV Cyclic voltammetry, cyclic voltammogram

LSV Linear sweep voltammetry, linear sweep voltammogram

MSCV Microelectrode sampled current voltammetry

ORR Oxygen reduction reaction

RDE Rotating disc electrode

RG Glass to electrode ratio, RG = $\phi_{glass}/a_{electrode}$

RHE Reversible hydrogen electrode

RRDE Rotating ring disc electrode

SCE Saturated calomel electrode

SCV Sampled current voltammetry

SECM Scanning electrochemical microscopy

SMSE Saturated mercury mercurous sulfate electrode

Chapter 1

Introduction

1.1 Structure of the Thesis

Perry and Denuault have reported the detection of adsorbed oxygen species that are left on Pt microelectrodes after exposure to molecular oxygen [1, 2]. They observed that the adspecies were affected by the electrode material, spectator species and oxygen concentration. Even after their thorough study, the identity and source of the adspecies remained unknown. The present work takes over the project started by Perry [3] and brings new information related to the adsorbed oxygen species, specifically, their relation to Pt oxides and *p*H. In the following paragraphs, a brief summary of the chapters of this work is presented.

Chapter 1 gives a brief introduction of the techniques and concepts that are used throughout this work. Section 1.2 presents the microelectrode theory with emphasis on diffusion and the kinetic parameters that can be obtained at the steady state. Sections 1.3 and 1.4 presents a short introduction to sampled current voltammetry and scanning electrochemical microscopy, techniques that are used in this work. In Section 1.5, a brief review about Pt electrochemistry is presented, with emphasis on Pt oxide formation and reduction. Section 1.6 presents a brief review about the oxygen reduction reaction in acidic and alkaline media, its different pathways, dependence on mass transport and electron transfer kinetics. Section 1.7 shows a summary of the work

done by Perry and Denuault to lay the foundations of this work. Finally, in Section 1.8, the specific objectives of the project are listed.

In Chapter 2, the experimental details used throughout this work are presented. Special care is placed on the calculation of the diffusion coefficient and concentration of oxygen, as they are widely used in this work. The basic potential waveform is also shown, and is reproduced when needed in the rest of the chapters as a reminder of its structure.

Chapter 3 focuses on the detection of the adsorbed oxygen species with electrodes that posses high rates of mass transport. The fast establishment of the steady state response is exploited to ensure that the response of the diffusion controlled current is known at all times; this is done as an improvement to the experiments reported by Perry and Denuault where they assumed a constant number of electrons even though it has been reported that n changes with the mass transfer coefficient [1, 4, 5]. In this way, the charge for the reduction of the adsorbed oxygen species, Q_{ads}, is better estimated. This is graphically shown in Figure 1.1, where a small spherical electrode is used to ensure that the diffusion controlled response is constant at all times; this is possible since the k_m achieved by this electrode is constant on the timescale of the experiment and any deviations in the current can be ascribed to the reduction of the adsorbed oxygen species. Chapter 3 also presents a stripping voltammetric methodology that does not rely on the subtraction of a theoretical current transient. Instead, it exploits the irreversibility behaviour of the adspecies. Briefly, it relies on recording two consecutive voltammograms, where the first one contains the contribution of the ORR and the reduction of the adsorbed species while the second one only shows the ORR. Subtracting both currents allows for the estimation of the coverage of the oxygen adspecies. Since this method does not rely on the subtraction of a specific theoretical response, it can be used with any electrode geometry.

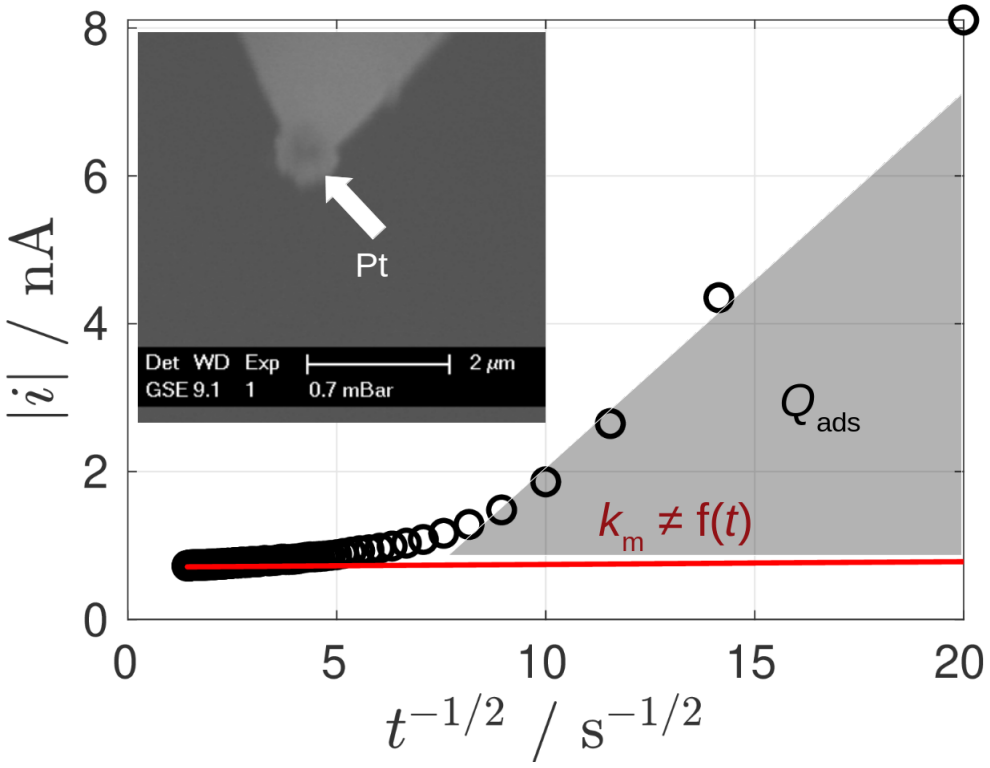

Figure 1.1: Graphical abstract for Chapter 3. A Pt spherical electrode is used to reduce oxygen and the adsorbed oxygen species. The theoretical diffussion controlled current is constant in the timescale of the experiment.

Chapter 4 is focused on the effect of *p*H on the adspecies and their relation with electrochemically grown oxides. The behaviour of the adspecies in neutral unbuffered media is compared with those in acidic and alkaline conditions, and it is observed that the reduction peaks are dependent on the local *p*H. It is also observed that the formation of Pt oxide seems to be unaffected by the presence of O_2 when working in extreme *p*H condition, while in unbuffered and neutral media, the oxide seems strongly affected by O_2. To further test for the effect of O_2 on oxide formation, hindered diffusion was exploited to decrease the contribution of the ORR to the total current. It is found that in neutral and unbuffered media, the local *p*H is increased during the ORR due to the production of OH^-, see Figure 1.2. If an oxidation potential is applied before the bulk pH is recovered, higher oxide coverages would be formed, according to the local pH. When the diffusion is hindered by approaching to an insulator, OH^- is confined in the vecinity of the electrode and so the local pH is even higher compared to bulk

conditions. The results of this chapter show strong evidence that the adsorbed oxygen species are Pt oxides that were formed at a higher *p*H.

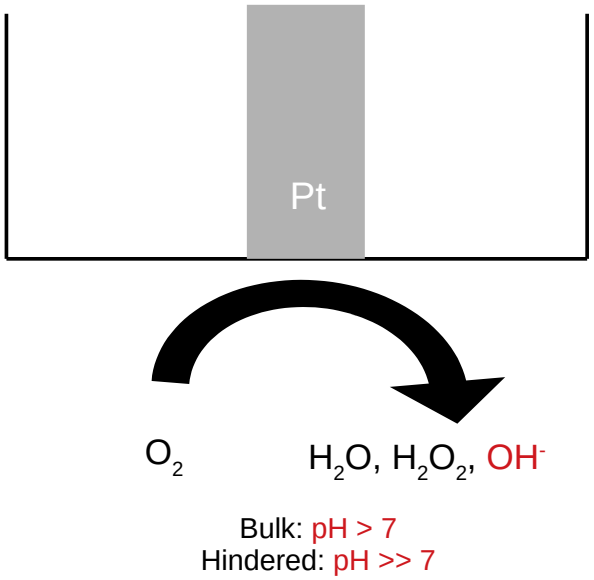

Figure 1.2: Graphical abstract for Chapter 4. During the ORR, OH^- is produced increasing the local pH.

Chapter 5 focuses on the analysis of sampled current voltammograms to study surface processes and the ORR. The chapter starts by showing that the SCV of Pt oxides are peak-shaped, contrary to the sigmoidal wave obtained when studying species in solution. Then, the ORR is studied, observing that under certain conditions, the waves are peak-shaped, demonstrating the presence of oxides. The sigmoidal waves obtained for the ORR, as well as the varying rates of mass transfer that can be obtained in transient conditions, makes SCV a good candidate to replace the rotating disc technique. This could be useful when dealing with materials that can not be converted into RDEs or when higher rates of mass transport are needed. In this chapter, sampled current voltammograms obtained with microelectrodes are turned into equivalent Koutecky-Levich and Tafel plots. The different regimes where the analysis is valid are discussed.

Chapter 5 ends with an analytical derivation of the response of SCVs when study-

ing quasi-reversible adsorbed species in the absence of diffusion. The theory for the coverage is derived assuming simple conditions and converted into charge and current transients. It is found that sampled current voltammograms of adsorbed species are peak shaped, see Figure 1.3. The analytical expression for the current is linearised to extract kinetic information.

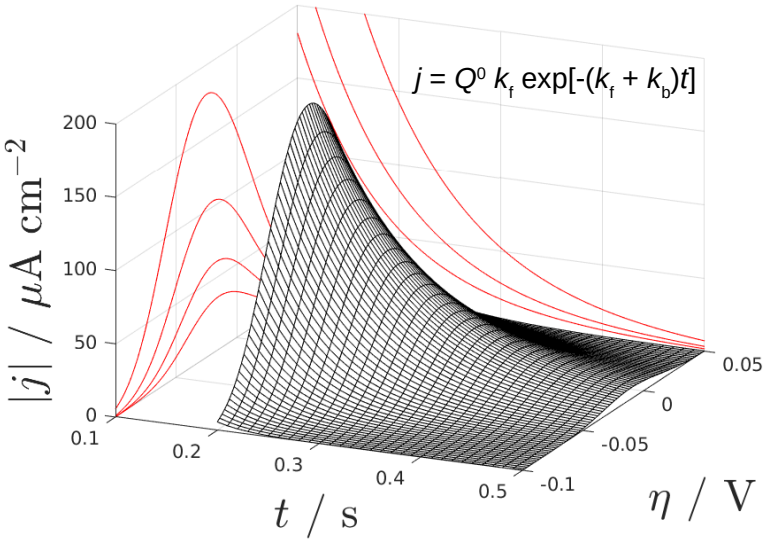

Figure 1.3: Graphical abstract for Chapter 5. Sampled current voltammograms of adsorbed species are peak shaped.

Finally, Chapter 6 presents the conclusions and summary of this work, with special emphasis on the novel contributions related to the adsorbed oxygen species and the use of sampled current voltammetry.

1.2 Microelectrodes

Microelectrodes are defined as those where their properties are a function of a characteristic size [6]. Some of these properties are a low IR distortion, fast charge and discharge of the double layer capacitance and high mass transfer coefficients. The most typical geometry used is the disc ($\phi \leq 50$ μm) but other geometries have been developed (spheres, hemispheres, rings, bands, etc.) [7, 8]. In this work, the theories for the sphere and the disc microelectrodes have been used and only these will be discussed.

1.2.1 Diffusion

Consider a typical chronoamperometry experiment, where the potential is changed from one where a reaction is not driven to one where the current is mass transport controlled. If the general reaction O + ne $\rightarrow$ R is assumed, the second potential will ensure that the concentration of O at the electrode surface is effectively zero. The current at a spherical electrode of radius r can be obtained after solving Fick's laws of diffusion for this case with the appropriate boundary conditions [8]:

$$i = nFADC\Big[\frac{1}{\pi^{1/2}D^{1/2}t^{1/2}} + \frac{1}{r}\Big] \tag{1.1}$$

Two limiting cases exist. If $r \rightarrow \infty$, the current will eventually decay to zero, this corresponds to the current obtained when an infinite planar electrode is used and is formally known as Cottrell equation:

$$i_{planar} = \frac{nFACD^{1/2}}{\pi^{1/2}t^{1/2}} \tag{1.2}$$

A plot of i against $t^{-1/2}$ should produce a straight line and the slope can be used to measure any of the electrochemical parameters provided the others are known. If now, $t \rightarrow \infty$, the planar diffusion term becomes negligible, and the current only depends on the size of the electrode; this current is called the limiting current of the electrode:

$$i_{lim} = 4\pi nFDCr \tag{1.3}$$

In general, a mass transport controlled current can be defined as:

$$i = nFACk_m \tag{1.4}$$

where k_m is the mass transport coefficient, which in the case of the spherical electrode:

$$k_m(t, r) = \frac{D^{1/2}}{\pi^{1/2} t^{1/2}} + \frac{D}{r} \tag{1.5}$$

that is, k_m is a function of time and radius, where the lowest k_m that can be obtained is that of the second term.

For the case of a microdisc, the theory is more complicated. Mathematically, it can be shown that Equation 1.1 predicts the diffusion controlled current at an equivalent sphere of radius $r = a/\pi$, where a is the radius of the disc; nevertheless it was already proven that this is only true for short and long times, where planar and hemispherical diffusions dominate respectively [9]. At long times, the limiting current of a microdisc is then:

$$i_{lim} = 4nFDCa \tag{1.6}$$

with k_m at the steady state:

$$k_m = \frac{4D}{\pi a} \tag{1.7}$$

At intermediate times, the description of the current is more complicated due to the evolution of the diffusion field. At those timescales, the edges of the electrode receive material linearly and radially, increasing the flux compared to the centre of the disc; this is known as the edge effect and it has been observed when electrodepositing metals at a diffusion controlled rate, where a higher current density promotes thicker deposited films at the edges [10, 11]. After a certain time, radial diffusion overcomes planar diffusion, forming the hemispherical diffusion field[1].

An analytical solution to the Fick's laws of diffusion for a microdisc can not be obtained, instead, simulations and empirical equations [12, 13] are normally used. Equation 2.8 was proposed by Shoup and Szabo and it was found to be exact within 0.6% at all

[1]This assumes that the disc is sealed in an infinitely large insulator that prevents back diffusion.

times [9, 12]:

$$i = i_{lim}\Big[\frac{\pi}{4} + \frac{\pi^{1/2}}{4a^2D^{1/2}t^{1/2}} + \Big(1 - \frac{\pi}{4}\Big)\exp\Big(-\frac{\pi^{1/2} - 8\pi^{-3/2}}{(4-\pi)a^2D^{1/2}t^{1/2}}\Big)\Big] \tag{1.8}$$

The mathematical form of the Shoup-Szabo equation has been exploited to measure the diffusion coefficient of species in solution [9]. The normalised current i/i_{lim} is only dependent on a, D and t, and so, if a is known, D can be measured directly. This methodology is very powerful, since a single transient experiment can be used to obtain D without the need of knowing the number of electrons and the concentration of the species beforehand. In Section 2.6.3, this methodology has been used to measure the diffusion coefficient of O_2 in different electrolytes.

Mahon and Oldham proposed a more precise model for predicting the current of a microdisc electrode at all times and is shown in Equation 1.9 [13]:

$$i = \pi nFDCaf(\sigma) \tag{1.9}$$

$$f(\sigma) = \begin{cases} \frac{1}{\sqrt{\pi\sigma}} + 1 + \sqrt{\frac{\sigma}{4\pi}} - \frac{3\sigma}{25} + \frac{3\sigma^{3/2}}{226} & \sigma \leq 1.281 \\ \frac{4}{\pi} + \frac{8}{\sqrt{\pi^5\sigma}} + \frac{25\sigma^{-3/2}}{2792} - \frac{\sigma^{-5/2}}{3880} - \frac{\sigma^{-7/2}}{4500} & \sigma \geq 1.281 \end{cases} \tag{1.10}$$

where $\sigma = Dta^{-2}$ and with k_m:

$$k_m = \frac{D}{a}f(\sigma) \tag{1.11}$$

Figure 1.4 shows current transients obtained with the Mahon-Oldham equation for different microdisc sizes. The red solid lines show the expected currents for planar and hemispherical diffusion. The plot shows that smaller electrodes can reach the steady state faster. In contrast, larger electrodes can retain planar diffusion for longer periods of time, and the current transients can be described with the Cottrell equation. Description of intermediate times require the use of either Shoup-Szabo or Mahon-Oldham equations; in this work, the latter was preferred as its error is minimal [13].

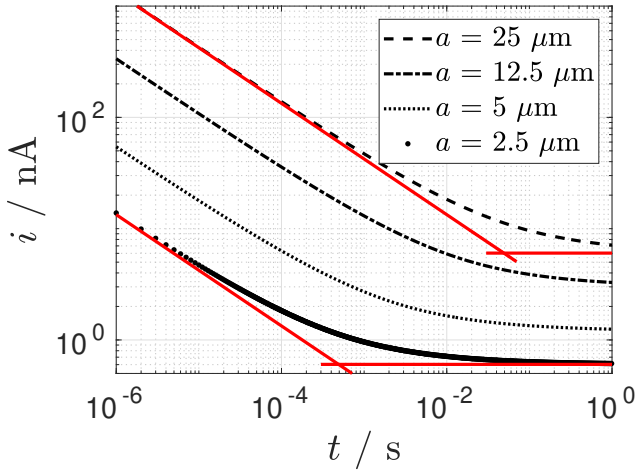

Figure 1.4: Current transients obtained with the Mahon-Oldham equation. The parameters used were $n = 1$, $D = 2.5\text{x}10^{-5}$ cm^2 s^{-1} and $C = 0.25$ mM. The red solid lines represent the expected current for planar and hemispherical diffusion at short and long times respectively.

Figure 1.5 shows the mass transfer coefficient for different microelectrode sizes calculated with Equation 1.11 (transient, markers) and Equation 1.7 (steady sate, red solid line). The lowest value of k_m that can be obtained with a microdisc is that given by the steady state; working in transient conditions results in an increased k_m. With the timescale used here (1 ms to 1 s), the mass transfer coefficients for the 25 and 12.5 μm electrodes are similar; in order to have an appreciable increase, smaller electrodes are needed. It can be seen that the steady state k_m for the 2.5 μm electrode [2] corresponds to the k_m obtained at approximately 2 ms for the 5 μm electrode [3].

[2]Given by the red line.

[3]Each data point on Figure 1.5 represents 1 ms; in the scale given by k_m, time increases in the negative direction.

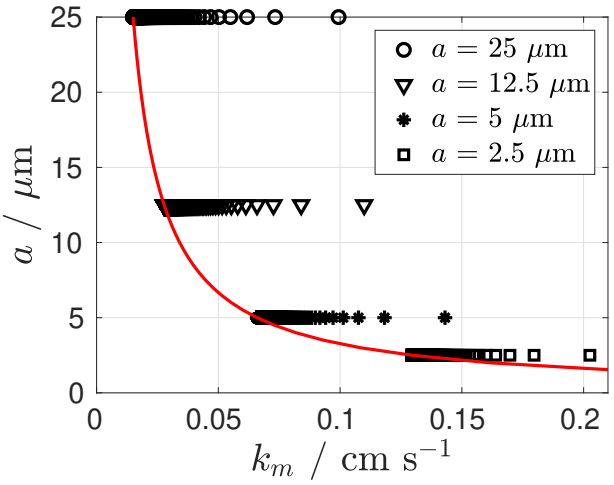

Figure 1.5: Mass transport coefficients calculated with $D = 2.5\text{x}10^{-5}$ cm^2 s^{-1}. The markers show the transient k_m obtained with the Mahon-Oldham equation between 1 ms and 1 s while the red solid line shows the dependence of k_m on a.

The different mass transport regimes can also be seen when varying the scan rate in a typical cyclic voltammetry experiment. Figure 1.6 shows simulated voltammograms obtained with a microdisc electrode ($a = 5$ μm). At low scan rates, a sigmoidal voltammogram is obtained, where the plateau represents the diffusion limited current, Equation 1.6. At high scan rates the voltammogram is peak-shaped, indicative of planar diffusion and similar to voltammograms recorded with macroelectrodes.

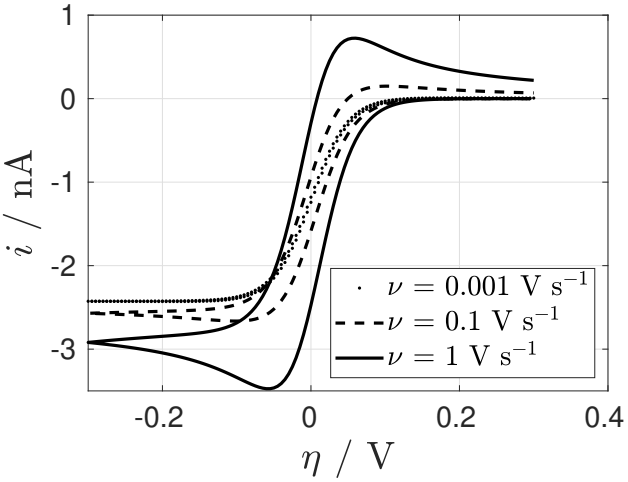

Figure 1.6: Cyclic voltammograms simulated with DigiElch 8 with $E^0 = 0$ V, $n = 1$, $\alpha = 0.5$, $k_s = 10000$ cm s^{-1}, $D = 2.5\text{x}10^{-6}$ cm^2 s^{-1} $C_{ox} = 5$ mM and $a = 0.5$ μm.

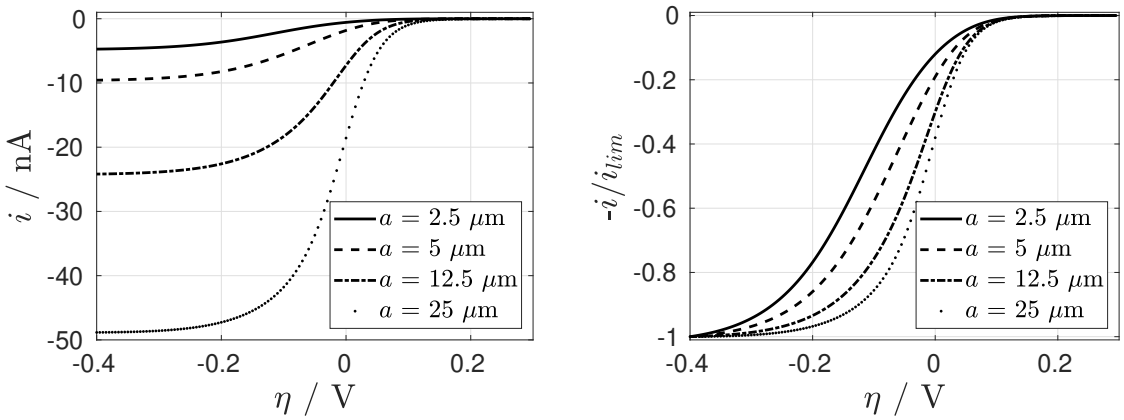

Figure 1.7: Simulated voltammograms for different electrode sizes with $\nu = 1$ mV s^{-1} and $k_s = 0.008$ cm s^{-1}, see Figure 1.6 for the rest of the simulation parameters.

1.2.2 Kinetics

Microelectrodes are generally used to measure rates of electron transfer of fast reactions [7, 14, 15]; voltammograms at the steady state reveal kinetic limitations as shifts in the half-wave potential. Figure 1.7 shows simulated voltammograms for different microelectrode sizes at the steady state. The limiting currents are proportional to the radius, as predicted by Equation 1.6. The shift in potential due to kinetic limitations is evident when normalising the voltammograms with their respective limiting currents.

To measure the kinetic parameters α and k_s, it is common to construct a Tafel plot; a straight line would indicate an electron transfer step. According to Butler-Volmer theory, the current of a fully irreversible system can be expressed as [8]:

$$i_k = nFACk_s \exp\Big(- \frac{\alpha F}{RT}\eta\Big) \tag{1.12}$$

and after linearisation:

$$\ln(i_k) = \ln(nFACk_s) - \frac{\alpha F}{RT}\eta \tag{1.13}$$

that is, the standard rate constant and transfer coefficient can be obtained from the intercept and slope respectively. If the current is affected by mass transport, a correction that accounts for the change in reactant concentration at the surface of the electrode needs to be used. This is normally done when using rotating disc electrodes

through the Koutecky-Levich equation, where a plot of i^{-1} against $\omega^{-1/2}$ should produce a straight line with the intercept given by i_k^{-1}. The Koutecky-Levich equation can be generalised to any diffusion controlled technique by noting that the second term corresponds to the limiting current:

$$\frac{1}{i} = \frac{1}{i_k} + \frac{1}{i_{lim}} \tag{1.14}$$

solving for i_k:

$$i_k = \frac{i\, i_{lim}}{i_{lim} - i} \tag{1.15}$$

With the limiting current for a microdisc, Equation 1.6, i_k can be expressed in terms of the mass transport current.

Figure 1.8 shows Tafel plots from the voltammograms in Figure 1.7. The linear region observed at high potentials corresponds to the kinetically limited region, Equation 1.12, while at low potentials the current is influenced by both, mass transport and electron transfer until the diffusion controlled region located at more negative overpotentials. Table 1.1 shows the calculated values of α and k_s by fitting Equation 1.13 to the kinetic limited region of the simulated voltammograms.

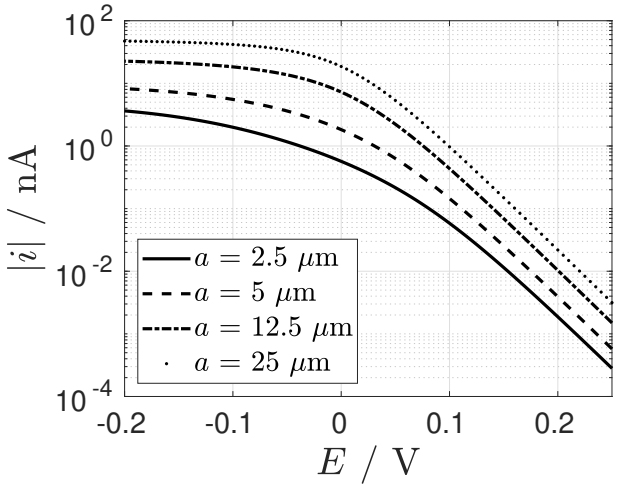

Figure 1.8: Tafel plots constructed from Figure 1.7.

Table 1.1 shows that the transfer coefficient is under estimated, while the value of k_s varies considerably. This error has been ascribed to electrodes that are not uniformly accessible, as it is the case for microdiscs, where the flux of reactant at the edges is

	2.5 μm	5 μm	12.5 μm	25 μm
α	0.43	0.43	0.43	0.43
k_s / cm s^{-1}	0.041	0.022	0.009	0.005

Table 1.1: Parameters obtained by fitting Equation 1.13 to the Tafel plots shown in Figure 1.8. The values used in the simulations were $\alpha = 0.5$, $k_s = 0.008$ cm s^{-1}.

higher than at the centre of the electrode [16, 17, 18]. Even with this error, microelectrodes are continuously used to measure kinetic parameters, specially when the rate of electron transfer is high and can not be measured with commonly used techniques; in this case, electrodes in the sub-micron scale are normally used [5, 19].

To better observe the error in the measurement of the transfer coefficient, Figure 1.9 shows the value of α calculated by taking the derivative of Equation 1.13:

$$\alpha = -\frac{RT}{F}\frac{\mathrm{d}\ln(i_k)}{\mathrm{d}\eta} \tag{1.16}$$

and the mass-transport corrected coefficient from Equation 1.15:

$$\alpha_{corr} = -\frac{RT}{F}\frac{\mathrm{d}}{\mathrm{d}\eta}\ln\Big(\frac{i\, i_{lim}}{i_{lim} - i}\Big) \tag{1.17}$$

In agreement with the results shown in Table 1.1, the smallest error is obtained at low overpotentials, and even though the mass-transport corrected coefficient shows an improvement at higher overpotentials, the value of α is still greatly under estimated. Better estimates of kinetic parameters with microdisc electrodes are obtained when using tabulated data after finding the quartile potentials [18]. In Chapter 5, Tafel plots are constructed from microelectrode sampled current voltammograms and tested for the ORR, the results show that SCV is a promising technique to test for kinetic limitations of electrochemical reactions.

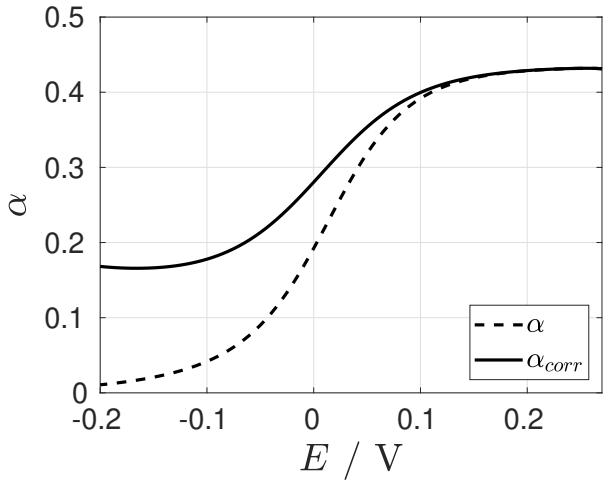

Figure 1.9: α calculated from Equations 1.16 and 1.17 from Figure 1.8.

1.3 Sampled current voltammetry

Sampled Current Voltammetry (SCV) is a technique which produces an $i(\tau) - E$ curve by applying different potential steps and sampling the data to construct a sampled current voltammogram [8]. Figure 1.10 shows how the construction of SCVs is performed. Briefly, different potential steps are applied and the current is recorded, then a sampling time is selected and the magnitude of the currents are plotted against their respective potential. If only the last data point is recorded for each current transient, the technique is called normal pulse voltammetry and the result is a single voltammogram; this technique was commonly used in combination with polarography, where the current was sampled just before the detachment of the mercury drop [8]. With the advent of programmable instruments, the procedure can be automated and the different current transients can be completely recorded, allowing for the construction of a large number of sampled current voltammograms limited only by the sampling time of the instrument.

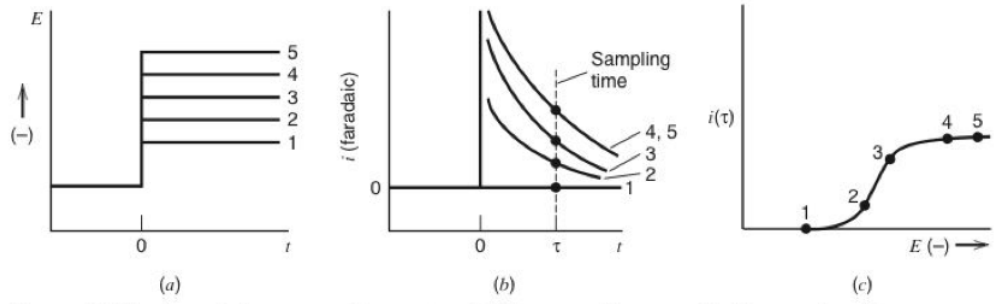

Figure 1.10: Construction of sampled current voltammograms. a) Different potential steps are applied, b) the current is sampled at a specific time, c) the sampled currents are plotted against their respective potential. Figure used with permission from [8].

Sampled current voltammograms for the reaction of species in solution are sigmoidal in nature independently of the diffusion regime and are said to reach a quasi-steady state, due to the dependence of the limiting current on the sampling time. In contrast, sweep voltammetry with macroelectrodes produces a peak-shaped voltammogram where the peak current is proportional to $\nu^{1/2}$. With microelectrodes, the shape of the voltammogram depends on the timescale of the experiment; at low scan rates a sigmoidal waveform is obtained, indicative of hemispherical diffusion, while at high scan rates the voltammogram is peak-shaped as diffusion is affected by the planar component. Perry and Denuault noticed this and decided to perform sampled current voltammetry with microdiscs [20]. While SCV allowed them to construct quasi-steady state voltammograms independently of the time regime, microelectrodes allowed them to record currents at short times, massively increasing the already high rate of mass transfer and accessing timescales where larger electrodes would be influenced by non-Faradaic currents.

As can be seen from Figure 1.10, the magnitude of the currents depends on the sampling time, where shorter sampling times give higher currents. In order to compare the voltammograms irrespective of the timescale of the experiment, Perry and Denuault normalized the current transient with the theoretical current for a microdisc electrode proposed by Mahon and Oldham [13], Equation 1.9. Since Equation 1.9 predicts the diffusion controlled current at all times, after the normalization procedure, the sampled current voltammograms fall on top of each other, provided the reaction under consid-

eration is diffusion controlled. More importantly, if the value of n in Equation 1.9 is set to 1, the plateau at the voltammograms falls into an apparent number of electrons n_{app} that are involved in the reaction.

Perry and Denuault showed that the slope of the voltammograms reveals kinetic information of the reaction, they studied the reduction of $Fe(ClO_4)_3$ at short timescales and observed that the curve was drawn towards more negative potentials. Similar to steady state voltammetry, this is an indication of a more irreversible wave. Faster reactions, as it is the case for the reduction of $Ru(NH_3)_6Cl_3$, require higher rates of mass transport to extract kinetics information. They also modified an equation first proposed by Oldham *et al.* [21] and fitted it to the SCVs; the results showed a good agreement with simulations and literature values. In Chapter 5 of this work, an equivalent Koutecky-Levich methodology is proposed with SCV, simplifying the estimation of kinetic parameters and improving the work done by Perry and Denuault.

1.4 Scanning electrochemical microscopy

Scanning electrochemical microscopy is a powerful electrochemical characterisation technique based on microelectrode theory [22]. Its more fundamental modes are negative and positive feedback, where a microelectrode is approached towards a substrate while driving a reaction at the diffusion controlled rate. Negative feedback occurs when the hemispherical diffusion field gets blocked by an insulator, decreasing the current as the electrode is approached towards the substrate; for this reason, this mode is also called hindered diffusion. In contrast, positive feedback occurs when a conductive substrate regenerates the reactant. Figure 1.11 shows a schematic of both modes of operation.

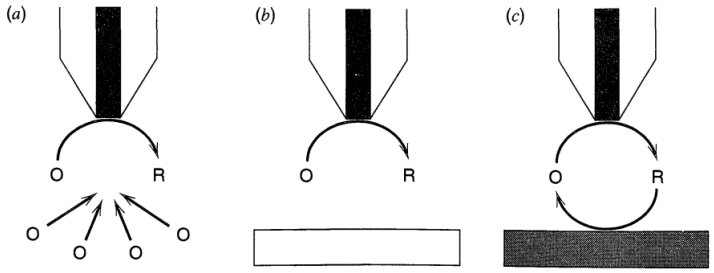

Figure 1.11: SECM operation modes. a) hemispherical diffusion in the bulk, b) hindered diffusion close to an insulating substrate, c) positive feedback close to a conductive substrate. Figure used with permission from [8].

An important parameter in SECM is the distance between the microelectrode tip and the substrate of interest. To calibrate the distance, an approach curve is recorded where the electrode is held at a potential where the current is limited by diffusion and moved towards a substrate at a low speed. Equations for the cases of positive feedback and hindered diffusion exist in the literature [23, 24] and depend on the RG of the electrode, where negative feedback is greatly affected by higher values of RG. For positive feedback and RG values between 1.1 and 10:

$$I(L) = k_1 + k_2/L + k_3 \exp(k_4/L) \tag{1.18}$$

while for hindered diffusion:

$$I(L) = \frac{1}{k_1 + k_2/L + k_3 \exp(k_4/L)} \tag{1.19}$$

where I is the current normalised by i_{lim} at the bulk, L is the distance normalised by the microelectrode radius and k_i are tabulated parameters that depend on RG. Figure 1.12 shows approach curves for both cases with different values of RG.

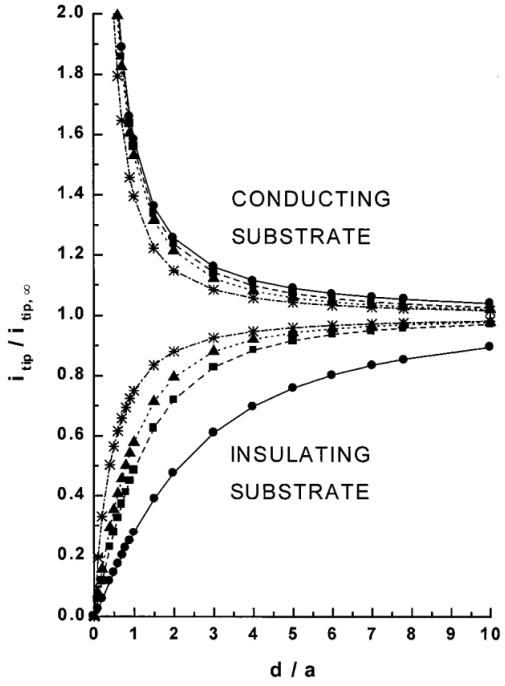

Figure 1.12: Approach curves for conductive and insulating substrates. RG = 1000 (circles), 10 (squares), 5 (triangles), 1.5 (stars). Figure used with permission from [23].

The approach curves shown in Figure 1.12, reflect the accessibility of the reactant to the microelectrode tip, and are an indication of the variation of the mass transfer coefficient as a function of the distance. In hindered diffusion, k_m is lowered at short tip-substrate distances due to the difficulty of the reactant to diffuse towards the electrode. In positive feedback, although reactant from the bulk is also hindered, the substrate can transform the product formed by the tip back to the reactant. The result is an increased mass transfer rate that can be exploited to study quasi-reversible reactions [22, 25]. The positive feedback mode is used as the base for the generation/collection mode of SECM, where any of the surfaces (microelectrode or substrate) can act as generators or collectors [26, 27].

In Chapter 4 of this work, hindered diffusion is exploited to study the effect of O_2 on oxide formation. The blocking of O_2 due to the close proximity to the substrate results in a decreased current contribution from the ORR. This methodology can be used to separate the current responses of adsorbed and diffusion controlled species, specially when their redox potentials are similar.

1.5 Pt surface processes

Pt is considered one of the best catalysts for many electrochemical reactions. As such, it is important to understand its processes since they can compete with the reaction of interest. Pt electrochemistry has been studied intensively for the past decades and although the surface processes on polycrystalline Pt is known, new properties are continuously found. In this section, a short review regarding the polycrystalline Pt surface processes is presented, with emphasis in the Pt oxide section as it is of great importance in this work.

The typical voltammogram of a polycrystalline Pt electrode in 1 M H_2SO_4 is shown in Figure 1.13. The surface processes seen are 1) double layer region, 2) Pt oxide formation, 3) oxygen evolution, 4) Pt oxide reduction, 5) hydrogen adsorption, 6) hydrogen evolution and 7) hydrogen desorption. The presence of well define peaks is generally accepted as a sign of the clean experimental conditions, this is due to the processes being severely affected by poisoning from trace amounts of contaminants and anion adsorption [28, 29, 30]. The following sections present a short review of the main processes.

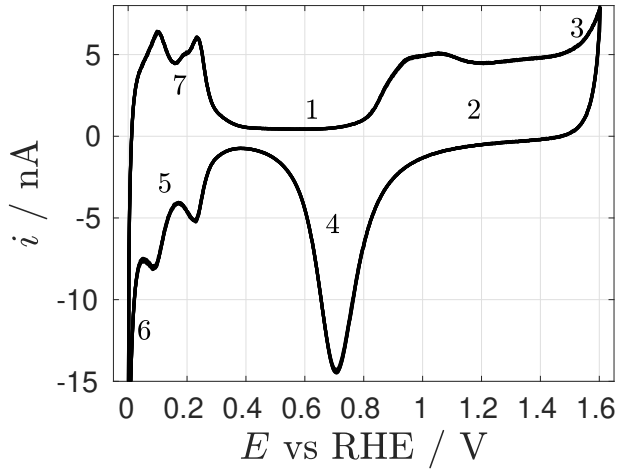

Figure 1.13: Cyclic voltammogram of a Pt electrode ($a = 25$ μm) in a 1 M H_2SO_4 solution saturated with Ar, $\nu = 200$ mV s^{-1}. 1) double layer, 2) oxide formation, 3) oxygen evolution, 4) oxide reduction, 5) hydrogen adsorption, 6) hydrogen evolution, 7) hydrogen desorption.

1.5.1 Double layer and hydrogen regions

The double layer region consists on an electrode-solution interface where charge can accumulate on both sides [8]. At any given time, the electrode would have an excess or deficiency of electrons, while the solution would have an excess of cations or anions [8]. The charging current of the double layer can be modelled with the equations for the charging of a capacitor. For a potential step:

$$i = \frac{E}{R_s}\exp(-t/R_sC_d) \tag{1.20}$$

that is, the current decays exponentially with time constant R_sC_d. Linearisation of Equation 1.20 allows for the estimation of the solution resistance and capacitance from the intercept and slope of Equation 1.21 respectively:

$$\ln(i) = \ln\Big(\frac{E}{R_s}\Big) - \frac{t}{R_sC_d} \tag{1.21}$$

For a potential sweep, Equation 1.22 is used:

$$i = \nu C_d[1 - \exp(-t/R_sC_d)] \tag{1.22}$$

that is, the current is proportional to the scan rate used, and at long times, when the capacitor is fully charged, the maximum current is given by νC_d. This constant value is what is observed in the double layer region shown in Figure 1.13. A plot of i against different ν would produce a straight line with slope C_d and if the specific capacitance is known (in F cm^{-2}), the electroactive area can be estimated [31].

The hydrogen region consist on the adsorption and desorption of H^+, where the peaks observed give information about the crystalline structure of the surface [32]. In acidic and alkaline solutions, the reactions are [33]:

$$\mathrm{Pt} + \mathrm{H_3O^+} + \mathrm{e^-} \rightleftharpoons \mathrm{PtH}_{ads} + \mathrm{H_2O} \tag{1.23}$$

$$\mathrm{Pt} + \mathrm{H_2O} + \mathrm{e^-} \rightleftharpoons \mathrm{PtH}_{ads} + \mathrm{OH^-} \tag{1.24}$$

The hydrogen adsorption region is extensively used to measure the electroactive area of Pt electrodes [31]. The charge of adsorption can be related to a coverage of 0.77 monolayers of hydrogen, equivalent to 210 μC cm^{-2} [34].

1.5.2 Pt oxide

Electrochemical oxide formation and reduction are continuously being studied due to their importance in other electrochemical reactions; oxidised surfaces are a requirement for the oxygen evolution reaction, while they are detrimental for the oxygen reduction reaction and the hydrogen peroxide oxidation and reduction reactions [35, 36, 37, 38]. It is well known that the type of oxide formed as well as its coverage are dependent on potential, pH, the presence of spectator species, among others [33, 39, 40]. Here, a brief review of some of this factors is presented.

It is commonly accepted that at low oxidation potentials ($E < 1$ V vs RHE), PtOH is formed according to the reaction [33, 41]:

$$\mathrm{Pt} + 2\,\mathrm{H_2O} \rightarrow \mathrm{PtOH}_{ads} + \mathrm{H_3O^+} + \mathrm{e^-} \tag{1.25}$$

This has been validated with the use of spectroscopic techniques [42, 43, 44, 45]. The identification of adsorbed species is important in the context of electrocatalysis, as they occupy active sites that could be used to drive the catalytic reaction. The group of Wakisaka used XPS and identified four types of oxygen species adsorbed on Pt-based electrodes, the species corresponded to $\mathrm{OH^-}_{ads}$, O_{ads} and two types of water [44, 45]. They observed that the binding energies of the species were independent on the crystal structure of the electrode and were constant in the potential region studied; in contrast, the measured coverage strongly depended on potentical and crystal orientation.

For a polycrystalline electrode, oxide formation and reduction are considered irreversible reactions [46], and their study is more complicated due to the so called place exchange mechanism and the formation of multilayered oxides. Initially, at low oxidation potentials, $\mathrm{OH^-}$ is adsorbed at the Pt surface. At potentials between 1.1 and 1.2 V, OH_{ads} and the Pt site change places, leaving the latter free for another $\mathrm{OH^-}$; this promotes the formation of multiple oxide layers [39]. This process is commonly referred to as the place exchange mechanism and is responsible for the roughening of the surface due to Pt dissolution observed at higher potentials [39, 47]. At more positive potentials, thicker oxides are formed, probably PtO and even $\mathrm{PtO_2}$ [36, 47, 48].

Sweep voltammetry and chronoamperometry are normally used to quantify oxide cov-

erages. The procedure normally consists on holding the potential in the oxide formation region and stripping it by either sweeping or stepping to a negative potential. Sweep voltammetry is normally preferred since the peak potential of the stripping can provide information about the different oxide species present [37]. Due to the possibility of forming multiple oxide layers with multiple oxide species, charge densities are used as a replacement for coverages. Historically, on Pt this has been done by integrating the current under the oxide reduction peak and normalising it with the charge obtained for the hydrogen adsorption region; a value of 2 would correspond to an equivalent monolayer of oxide [49]. It was observed that at high potentials, the oxide to hydrogen ratio was 2:1, leading to the generally used value of 420 μC cm^{-2} for oxide formed at high potentials ($E > 1.4$ V). In fact, it has been widely reported that the charge has a linear dependency on the oxide formation potential [37, 46, 50], while oxide formation time has a logarithmic effect, requiring long times to increase the charge appreciably [39, 51].

Technologically, it is important to know if the presence of molecular oxygen influences the oxide formation region; an oxidised surface can be detrimental for certain reactions (oxygen reduction, hydrogen peroxide reduction, etc. [35, 36, 37]). Interestingly, little attention has been put into this issue. The groups of Kongkanand and Liu have studied this with quartz crystal microbalance and flow cells [52, 53]. The use of flow cells allowed them to oxidise the surface in the presence of O_2 and strip it in its absence by changing to an O_2-free solution. Their methodology seems to suggest that O_2 does not affect oxide coverages, although it is worth noting that oxide formation and stripping were performed in different conditions. In Chapter 4 of this work, hindered diffusion is exploited to study the effect of O_2 on oxide formation and reduction, and contrary to the work done by the groups of Kongkanand and Liu, here, oxide formation and reduction are performed in the presence of O_2.

Being a surface process, oxide formation is strongly affected by species that can compete for active sites. Anion adsorption on Pt has been intensively studied and the results point towards ClO_4^- having the less effect [54]. On the contrary, Cl^- and Br^- block the surface in a greater extent, where Cl^- concentrations in the micromolar scale

can prevent PtOH formation while Br^- can completely cover the surface [29, 55]. In addition, Cl^- is also known to promote Pt dissolution [56]; it has been reported that intensive cycling and stepping between oxide formation and reduction leads to the roughening of the surface [49, 57]. Overall, special care has to be taken when studying surface processes; clean conditions are required to prevent blocking of the active sites [58, 59]. In Chapter 2, an intensive cleaning procedure is used to minimise the presence of contaminants that could affect the results.

1.6 Oxygen reduction reaction

The oxygen reduction reaction has great technological importance, participating in fuel cells, metal-air batteries, biological studies and others [60]. Despite its importance, the ORR still has several challenges to overcome in order to reach commercial application. One of the major challenges to overcome is the use of precious metals that greatly increases the cost of production. Different metals have been used to studied the ORR; among them, Pt delivers the best performance but the high cost of Pt-based technology makes its introduction to the market difficult to achieve. Reducing the loading of the metal is a commonly used strategy to decrease the cost; this is normally done by embedding nanoparticles in a carbon-based ink, allowing researchers to study the relation between the nanoparticle crystal structure, size, and loading with the ORR [36, 61]. The use of nanoparticles has allowed researchers to optimize morphological properties such as geometry, crystal orientation and surface defects. To reduce the cost even further, some groups have taken different alternatives and designed Pt-based alloys, bimetallics and non-noble metal catalysts [60, 62]. Even though these are better alternatives from an economical point of view, these catalyst are still far from the efficiency given by Pt. In order to rationally design better catalysts, it is necessary to fully understand the ORR mechanism, and for this, fundamental studies are still performed with polycrystalline and single crystal Pt surfaces.

Another challenge to overcome relates to the relatively high overpotential needed to drive the reaction. At the onset of the ORR, the presence of low oxide coverages

is known to inhibit the reaction [36, 37] and it is believed that this is the source of the high overpotential needed. The effect of oxide coverages on the ORR has been studied in acidic and alkaline conditions, observing similar effects regarding the onset potential [36, 37]: at higher coverages, a higher overpotential is needed to drive the reaction.

In general, the onset of the ORR is affected by any site-blocking species, being an oxide [36, 37], anion adsorption [28, 63] and contaminants [58]. In the case of anion adsorption, Cl^- concentrations as low as 10 μM have shown to greatly affect the ORR due to the strong affinity of Cl^- towards noble metals [58]. The ORR in noble metals is then highly sensitive to contamination and requires intensive cleaning procedures to ensure that the true catalytic response is obtained. The care taken by researchers into this, is evidenced by the different cleaning protocols developed that range from the use of concentrated acids and bases, soaking in piranha solutions, intensive rinsing and even boiling [58].

1.6.1 Pathways and pH dependence

Despite the importance of the ORR and the many studies performed, its full mechanism is still unknown probably due to the difficulty of detecting intermediates that participate in the reaction. Different complex mechanism have been proposed that involve soluble and adsorbed intermediates as well as radicals [64, 65]. Instead, reaction paths have been generally used, where the simplest and most commonly used involves the reduction of oxygen through a direct path with the transfer of four electrons or through an indirect path that involves the formation of intermediates [4]. In acidic media, the direct path involves the use of four protons and four electrons:

$$O_2 + 4H^+ + 4e^- \rightarrow 2H_2O \tag{1.26}$$

while in alkaline media the ORR uses two water molecules as the source of protons:

$$O_2 + 2\,H_2O + 4e^- \rightarrow 4\,OH^- \tag{1.27}$$

while the indirect path in acidic media forms peroxide as an intermediate:

$$O_2 + 2H^+ + 2e^- \rightarrow H_2O_2 \tag{1.28}$$

$$H_2O_2 + 2H^+ + 2e^- \rightarrow 2H_2O \tag{1.29}$$

and in alkaline media:

$$O_2 + H_2O + 2\,e^- \rightarrow HO_2{}^- + OH^- \tag{1.30}$$

$$HO_2{}^- + H_2O + 2\,e^- \rightarrow 4\,OH^- \tag{1.31}$$

From the above reactions, it is evident that the ORR is *p*H sensitive. The direct path shows that in alkaline conditions, the local *p*H increases due to the production of OH^-, while in acidic conditions the increase in *p*H is due to the exhaust of H^+ in the vicinity of the electrode. When using extreme *p*H or buffered media, these effects are negligible, since the solutions would have a high buffer capacity. For unbuffered solutions with intermediate values of *p*H, this is not the case.

RDE studies at unbuffered media have shown two distinctive behaviours [33, 41]. Voltammograms obtained at *p*H higher than 6 show that the ORR proceeds trough the alkaline path, using protons from water molecules and locally increasing the *p*H of the solution. In lower *p*H (up to *p*H = 3), the voltammogram is split in two distinctive waves. Results with RDE have shown that the first wave, which appears at more positive potentials, is limited by the diffusion of H^+, as evidenced by the linear dependency of the limiting current with H^+ concentration. At lower potentials, H^+ are exhausted faster and the ORR can not be maintained through the acidic path, instead, the reaction uses H_2O as the source of protons, forcing the alkaline path and forming the second wave.

In general, the ORR in neutral and unbuffered media is complicated by the reaction being sensitive to *p*H. Care has to be taken when working in these conditions. At-

mospheric CO_2 can dissolve into water and react to form carbonic acid, effectively lowering the *p*H and possibly changing the reaction path to the acidic one. This can be minimised by using high purity O_2, maintaining a closed cell and purging the solution with Ar previous to the introduction of O_2.

1.6.2 Mass transport and kinetics

Mass transport has also shown to play a role on the reduction of O_2. Steady state voltammograms recorded in acidic and alkaline conditions show the typical sigmoidal wave expected for diffusion controlled reactions. From the limiting currents, it is possible to elucidate the number of electrons that participate in the reaction. This is easily done by normalising the limiting current with Equation 1.4 assuming $n = 1$ and by using the appropriate expression for k_m. The number of electrons has been reported to depend on *p*H; acidic conditions show $n = 4$ while results in alkaline solutions show $n = 2$ [66]. It is believed that the 2-electron transfer reaction obtained in basic conditions is due to the presence of OH^- in the surface of the electrode that prevents further reduction of peroxide towards water [67].

The number of electrons is also dependent on mass transport. Pletcher and Sotiropoulos reported fractional values of n when studying the ORR with high rates of mass transport [4]. This apparent number of electrons, with values varying between 2 and 4, was attributed to an incomplete reduction of oxygen, where the values of n_{app} obtained were in fact averages related to the amount of O_2 that was completely reduced to water. Chen and Kucernak later confirmed these results with the use of nanoelectrodes [5]. This decrease of n_{app} with increase in k_m was explained in terms of the fast removal of peroxide before it can be further reduced to water. In all cases, the ORR has been studied under well defined mass transport regimes, generally with RDE and RRDE. With the latter, it is possible to directly measure the production of peroxide by oxidising it with the ring, confirming what was observed by the groups of Pletcher and Chen.

Tafel plots are regularly used to study catalysts performance during the ORR. Results

with Pt-based electrodes generally show two Tafel slopes depending on the potential range studied [60]. At high overpotentials, the Pt surface is presumably oxide-free, producing a Tafel slope of -120 mV dec^{-1} while at low overpotentials, the ORR proceeds with a partially oxidised surface resulting in a Tafel slope of -60 mV dec^{-1}. Studies of the influence of Pt oxide on the ORR have confirmed that the Tafel slope is highly affected by the presence of oxides [36].

1.7 Adsorbed oxygen species after exposure to dissolved oxygen

Perry and Denuault reported the detection of an adsorbed oxygen species left after exposure of a Pt electrode to molecular oxygen [1, 2]. The conditions of their study are quite specific. They used a Pt microelectrode at the transient state which allowed them to discriminate non-Faraday currents at short times. They also used a neutral unbuffered media solution (0.1 M $KClO_4$); preliminary experiments performed by Perry showed that the species could not be detected with acidic media [3]. They reported the use of a pre-conditioning potential waveform to ensure that a reduced Pt surface was used every time. The potential waveform is shown in Figure 1.14. It consists of three main parts. First, the electrode is cycled between -0.1 and 1.2 V vs RHE at 0.5 V s^{-1}; the upper cleaning potential was selected to ensure that a small amount of oxide is formed, while the lower cleaning potential would completely reduce it. The last positive sweep ensured that the next step started with a reduced Pt surface. The second section of the pre-conditioning waveform consisted of applying a certain potential for 10 s; this potential was selected at a slightly more positive potential than the onset for oxygen reduction. Perry and Denuault reported that the rest potential had two objectives: first, it would allow for the recovery of the bulk O_2 concentration after being reduced during the cleaning section of the waveform; at the same time, it would allow the oxygenated species to adsorb. The third section consisted on the reduction of the adspecies by either a potential step [1] or a cathodic sweep [2].

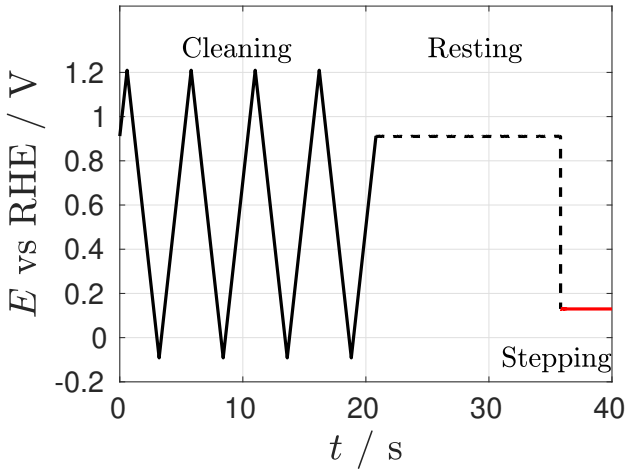

Figure 1.14: Potential waveform used by Perry and Denuault and throughout this work. Cleaning: sweeps at 500 mV s^{-1}, rest: potential held for 15 s, step: potential held for 1 s. Potential and time for the resting and stepping can vary.

Figure 1.15 shows Cottrell plots reported by Perry and Denuault. The plot also shows a theoretical diffusion controlled current from the Mahon-Oldham equation, Equation 1.9. Perry and Denuault normalised the current transient obtained at the ORR plateau with the Mahon-Oldham equation assuming $n = 1$. With a diffusion controlled reaction, this procedure reveals the apparent number of electrons at all times [20]:

$$n_{app} = \frac{i}{\pi FDCaf(\sigma)} \tag{1.32}$$

For the oxygen reduction reaction, the expected value of n_{app} at the steady state is 3.3 and should decrease in transient conditions as the mass transfer coefficient increases; this has been observed at the steady state with RDE, microelectrodes and nanoelectrodes [4, 5]. Instead, Perry and Denuault observed that the apparent number of electrons increased, suggesting that the process occurring was not diffusion controlled in nature. They plotted the experimental current transient and fitted the Mahon-Oldham equation at long times and noted a difference in current at short times. Integration of the difference allowed them to calculate a charge of adsorption of the oxygenated species, [4] $Q = 33$ μC cm^{-2}. They also observed a lower current magnitude recorded

[4]The reported value was $Q = 55$ μC cm^{-1} due to an error on the calculation of the electroactive area. See Chapter 2 for the correct calculation.

on similar conditions but in the absence of O_2, suggesting that the adsorbed species were related to the presence of molecular oxygen.

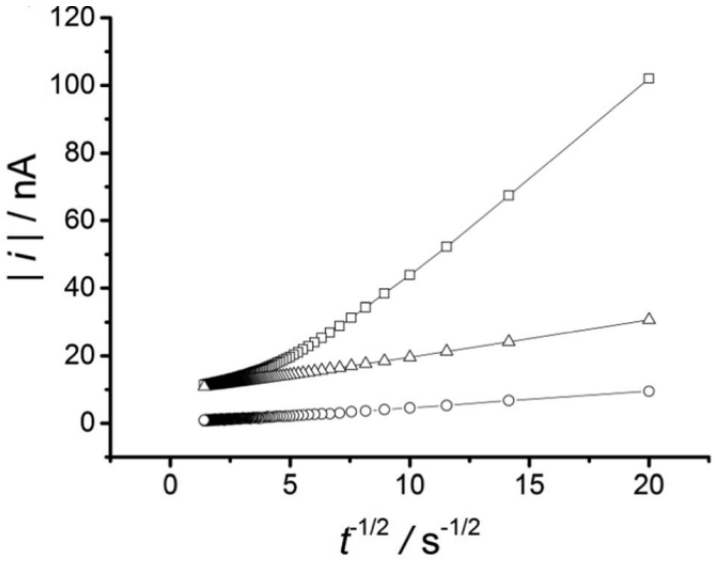

Figure 1.15: Current transients recorded in 0.1 M $KClO_4$ aerated (squares) and in Ar-saturated (circles) solutions using a Pt microdisc electrode (a = 12.5 μm). The triangles show the theoretical current calculated from the Mahon-Oldham equation. Figure used with permission from [1].

Perry and Denuault also constructed sampled current voltammograms and normalised them with the Mahon-Oldham equation as shown in Equation 1.32. They expected a constant value of n_{app} independently of sampling time; instead they observed that this was only true at long times, while at short times n_{app} increased. More importantly, the adsorbed species was observed to affect the whole potential range of the oxygen reduction reaction wave, suggesting that the species were oxygenated in nature. Stripping voltammetry and comparison with theoretical results confirmed the oxygenated nature of the species [2].

Perry and Denuault performed a series of experiments to test the behaviour of the adspecies [1]. They observed an increase in Q when increasing the rest time; for rest times longer than 10 s, Q reached a plateau. They also changed the rest potential and observed that Q was independent of E_r until around 1.1 V vs RHE; oxide formation occurred at more positive potentials. They also performed experiments in the presence of anions with different binding energies; the charge of adsorption decreased with the

trend ClO_4^- < Cl^- < Br^- < I^-. The current transient recorded in the presence of I^- agreed with the expected mass transport controlled current given by the Mahon-Oldham equation. These experiments led them to conclude that the species being probed were adsorbed on the surface, as the different anions are known to block Pt active sites in the same trend observed. The species were also shown to be irreversibly adsorbed; this was tested by applying the cleaning and rest sections of the waveform in the presence of O_2, and the step potential in absence of O_2. Even after removal of molecular oxygen the extra current was observed, proving that the species were irreversibly adsorbed to the electrode.

The existence of the adsorbed oxygenated species was first reported by Perry and Denuault. The reduction of oxygen in a neutral and unbuffered media in combination with the transient response of microelectrodes allowed them to observe the presence of the species. It is believed that their detection was due to the specific conditions used in their work that can not be reproduced with other techniques. Generally, the ORR is studied either in acidic or alkaline media [36, 60]; although some groups have work with the ORR in neutral and unbuffered solutions, their experiments are performed under the steady state with RDE and microelectrodes [4, 33]. Perry and Denuault showed that the adspecies were completely reduced in the millisecond scale and so working in transient conditions is required.

1.8 Objectives

Even with the thorough study performed by Perry and Denuault, the identity and behaviour of the adsorbed species is unknown. The present work takes over the project started by Perry [3] and shows results regarding the origin of the adsorbed species as well as their interaction with the oxygen reduction reaction and the formation and reduction of Pt oxides. The list of objectives are as follows:

- To separate the current contribution of the adsorbed species from the total current.

- To study the oxygen reduction reaction and the reduction of adsorbed species independently from each other.
- To understand the role of O_2 on the detection of the adsorbed oxygen species.
- To understand the relation of the adsorbed oxygen species with the oxygen reduction reaction.
- To understand the influence of pH on the adsorbed oxygen species behaviour.

Chapter 2

Experimental

This chapter presents the experimental details used throughout this work. It has been divided in different sections. The first sections concern to the list of materials, the electrochemical setup and the cleaning procedures. Then, the construction and characterisation of the working and reference electrodes is presented, as well as the basic potential waveform used; modifications of the waveform are shown when needed in the results chapters. The next section presents the methodology used to calculate the concentration and diffusion coefficient of oxygen. Lastly, experimental details about SECM are presented.

2.1 Materials

This section presents the list of materials used in this work. Table 2.1 shows the list of gasses used. Both, Ar and O_2 were obtained from BOC, while air was obtained from an external compressor; a Dreschell bottle was used to decrease the amount of impurities (see following section).

Table 2.2 shows the chemicals used throughout this work; they were used as received without further purification. $KClO_4$ of different purities were used; in Chapter 4, where better cleaning conditions were needed, the higher purity $KClO_4$ was used.

Gas	Purity	Company
O_2	99.5 %	BOC
Ar	99.999 %	BOC
Air	-	external compressor

Table 2.1: List of gasses used.

Chemical	Purity	Company
H_2SO_4	95-98 %	Sigma-Aldrich
$KClO_4$	99 %	Sigma-Aldrich
$KClO_4$	99.99 %	Sigma-Aldrich
H_2PtCl_6	99.9 %	Sigma-Aldrich
$Ru(NH_3)_6Cl_3$	98 %	Sigma-Aldrich
$K_4Fe(CN)_6$	99 %	AnalR
KCl	99 %	Fisher Chemical
K_2SO_4	99.5 %	Fisher Chemical
$KMnO_4$	99.5 %	AnalR
H_2O_2	100v > 30% w/v	Fisher Chemical
NaOH	97 %	Fisher Chemical
$HClO_4$	99.999 %	Sigma-Aldrich
H_2O	18 MΩ	Purite

Table 2.2: List of chemicals used.

2.2 Electrochemical setup

The setup used in this work is similar to the one used by Perry [3]. The potentiostat used was the PGSTAT101 from Autolab controlled by Nova 1.11. Voltammograms of adsorbed species (hydrogen, adsorbed oxygen species) were always recorded with the procedure Staircase Cyclic Voltammetry Current Integration. In this mode, the current during the voltage staircase is integrated with internal electronics; the charge obtained is then differentiated mathematically to obtain a current with less losses

of information than the normal staircase voltammetry. As an example, Figure 2.1 shows cyclic voltammograms of a Pt microelectrode ($a = 25$ μm) with and without the current integration mode. As it can be seen, information about hydrogen adsorption and desorption processes is lost when regular staircase voltammetry is used.

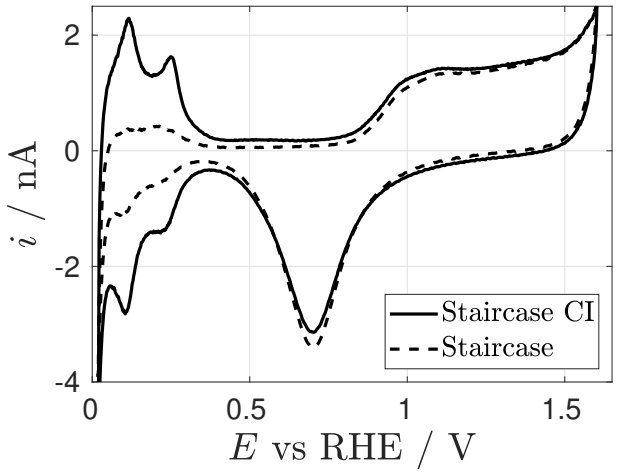

Figure 2.1: Cyclic voltammogram in 1 M H_2SO_4 with a Pt disc electrode ($a = 12.5$ μm) with the procedure cyclic voltammetry and cyclic voltammetry current integration. The scan rate used was 0.2 V s^{-1}.

Chronoamperometry experiments were obtained with a sampling time of 2.5 ms with the high speed mode; this mode does not filter the data resulting in the raw values of the current with the drawback of a signal affected by noise. The noise was minimised by using a Faraday cage and by grounding all metallic objects required (Faraday cage, stands, clamps). The current ranges available to the PGSTAT101 can record currents up to three times their value [1]. In this work, the appropriate current range was selected; when overloading occurred, the current range was change to the next value and the experiment was repeated.

The glass electrochemical cells were constructed by the Glass Section of the School of Chemistry and consisted on jacketed cells with five necks, The experiments were always performed under temperature control at 25 ^{o}C with the help of a water bath. Either Ar, O_2 or air were introduced in the cell as required by first passing them through a Dreschell bottle with deionised water; the Dreschell bottle acted as a humidifier for the

[1] A current range of 10 nA can record currents up to 30 nA without overloading.

gasses and, in the case of compressed air, as a particle trap to minimise contamination. The cell was kept closed at all times and a glass neck was connected to a water reservoir to act as a gas outlet and to prevent air going into the cell.

2.3 Cleaning procedures

Two different cleaning procedures were used. For experiments involving the use of aerated solutions (Chapter 3 and SECM experiments), all the glassware was soaked overnight in diluted Decon90, 5% in volume, followed by extensive rinsing with deionised water. The cells were kept under water prior use.

When using O_2 instead of air, cleaner conditions were needed. For this, all the glassware was first soaked several hours in a solution consisting of 0.7 g/L of $KMnO_4$ with 40 mM H_2SO_4; this solution oxidizes organic molecules left in the glassware. After rinsing with deionised water, the glassware was then soaked in a diluted piranha solution for several hours [2] (30 mM H_2O_2 and 40 mM H_2SO_4) to remove the traces of organics and the $KMnO_4$ left. After rinsing with deionised water, the glassware was boiled three times for at least 30 min each. Prior to use, the glassware was kept in deionised water to minimise contamination.

2.4 Electrodes

This section presents the different electrodes used in this work. The reference electrodes were homemade previously or obtained commercially, while the working electrodes were constructed and characterised and the results are presented here.

2.4.1 Reference electrodes

With microelectrodes, a counter electrode is normally not required due to the small currents that can be supplied by the reference electrode without changes in its poten-

[2] Although diluted, this solution is highly corrosive and needs to be handled with care.

tial; because of this, all the experiments were performed with a two-electrode system consisting on reference and working electrodes.

Different reference electrodes were used throughout this work depending on the electrolyte used. Experiments in H_2SO_4 were performed using a saturated mercury mercurous sulfate electrode (SMSE); its potential was measured against a reversible hydrogen electrode (RHE) giving $E = 0.673$ V.

For experiments concerning the use of Cl^- as supporting electrolyte, a saturated calomel electrode (SCE) was used as reference electrode. In Chapter 3, experiments concerning the ORR were performed by using a SCE; the potential was converted to a RHE according to:

$$E_{\mathrm{RHE}} = E_{\mathrm{SCE}} + 0.059p\mathrm{H} + 0.241 \tag{2.1}$$

Experiments in Chapter 4 were performed with a commercial RHE from Gaskatel, this was done to avoid Cl^- leakage from the SCE that could interfere with the adsorbed species. To test for chloride contamination, cyclic voltammograms and current transients at the oxygen reduction reaction plateau were recorded vs a SCE and a Pt mesh as a quasi reference electrode (Pt QRE). Since the potential of a QRE depends on the species in solution, the difference in potential between the SCE and the Pt QRE on both, air and Ar saturated solutions was recorded for 30 min while the cell was off. New solutions were used each time to prevent cross contamination. Figure 2.2 shows the change in potential for both cases, and their final values were used to convert the potentials to RHE.

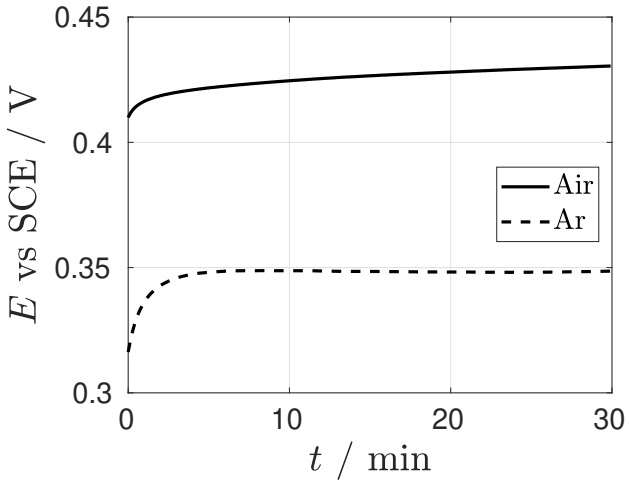

Figure 2.2: Potential of a Pt QRE in 0.1 M $KClO_4$ in the presence of air or Ar.

Cyclic voltammograms were recorded using both reference electrodes and new solutions each time. Figure 2.3 shows CVs in an aerated solution; the hydrogen adsorption and desorption peaks and the oxide reduction peak are more visible when the Pt QRE electrode was used. The differences suggest the presence of an adspecies that prevents the adsorption of hydrogen, presumably Cl^-.

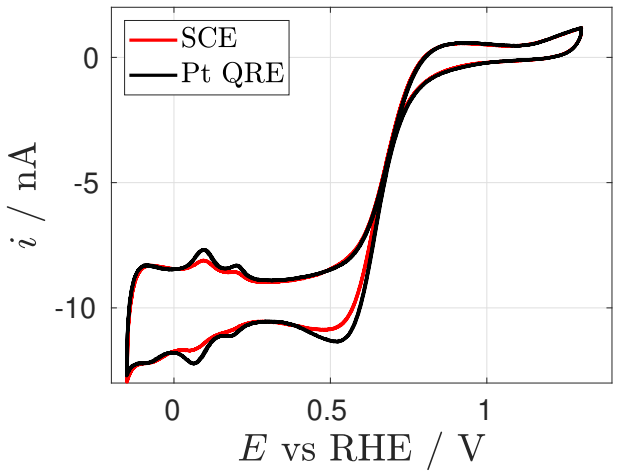

Figure 2.3: Cyclic voltammograms in an air saturated 0.1 M $KClO_4$ solution at 0.2 V s^{-1} using a Pt microdisc electrode (a = 12.5 μm). The temperature was maintained at 25 ^{o}C and a new solution was used for each CV.

Figure 2.4 shows CVs in Ar-saturated solution; here, big differences can be observed. The oxide formation region when using the SCE seems shifted to more positive po-

tentials, this regions corresponds to the formation of PtOH and is highly sensitive to Cl^- contamination [30, 56]. The lower amount of oxide formed is also evidenced in the oxide reduction peak, where the current recorded with the SCE is smaller. The hydrogen desorption peaks seem to also be affected by Cl^- leakage from the SCE, where the peaks are shifted to negative potentials and with similar magnitudes. Similar CVs have been reported for solutions in degassed KCl; here, it is possible that the small volume of the cells (< 20 ml) and the close arrangement between the reference and working electrodes prevents the Cl^- from diffusing away and instead, covers the Pt surface. Even with Cl^- adsorption, Perry and Denuault demonstrated that the adsorbed oxygen species could be detected [1]; in Chapters 4 and 5, a RHE was used to minimise contamination and to obtain a more reliable coverage of the adspecies.

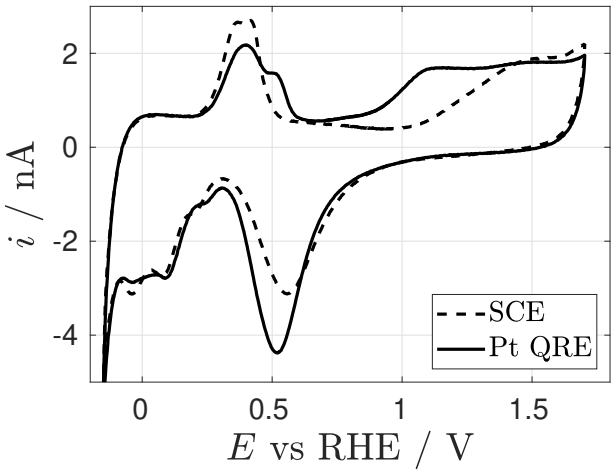

Figure 2.4: Cyclic voltammograms in an Ar saturated 0.1 M $KClO_4$ solution at 0.2 V s^{-1} with a Pt microdisc electrode ($a = 12.5$ μm). The temperature was maintained at 25 ^{o}C and a new solution was used for each CV.

Chloride contamination was also tested with the presence of the adsorbed oxygen species reported by Perry and Denuault [1, 2]. Current transients at the ORR plateau ($E = 0.2$ V vs RHE) in aerated conditions are shown in Figure 2.8. They were recorded after conditioning the electrode and resting for 15 s as reported previously [1, 2]. A significant decrease can be seen when the SCE is used. Even though the use of a Pt QRE has been reported in the literature [5], this should be avoided due to changes in potential as well as local changes in pH. Experiments in Chapters 4 and 5, that

required cleaner conditions, were then performed with a commercial RHE to avoid Cl^- contamination.

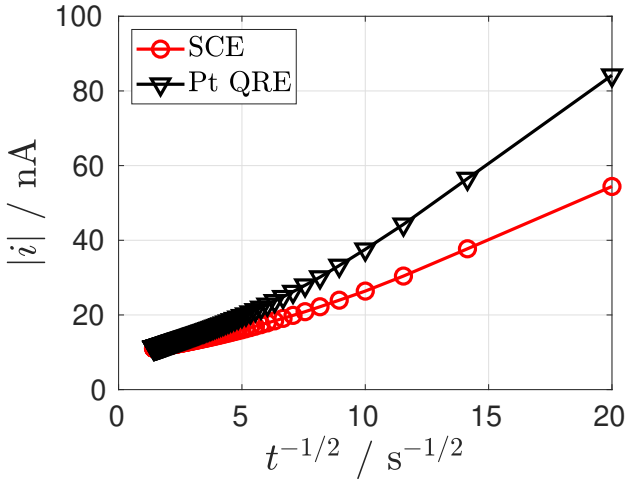

Figure 2.5: Current transients recorded at 0.2 V vs RHE in an air saturated 0.1 M $KClO_4$ solution at 25 ^{o}C with a Pt microdisc electrode (a = 12.5 μm).

2.4.2 Pt microdisc electrodes

Pt microdisc electrodes were constructed by sealing Pt microwires of different diameters (5, 10, 25 and 50 μm, Goodfellow) in glass tubes. The glass was then polished with sand paper of different grades (600 and 1200) until the Pt disc was revealed, followed by polishing using alumina suspension of different sizes (5, 1 and 0.3 μm, MetPrep) until no marks were seen in the glass under an optical microscope with the use of a 100x lens. The electrical contact was made with indium and an electrical wire. The electrodes were kept in water to prevent contamination.

Figure 2.6 shows optical images of the polished discs. Deviations from a circular geometries make the measurement of the radius difficult; instead, the software can measure geometrical areas by identifying zones with different contrasts, with this, the radius was obtained assuming a perfect circle with $a = \sqrt{A/\pi}$.

Figure 2.7 shows steady state voltammograms of Pt microdisc electrodes in $K_4Fe(CN)_6$. The sigmoidal wave shown is evidence of the hemispherical diffusion field created by the microelectrodes at low scan rates. Even though the radius of the electrode can be

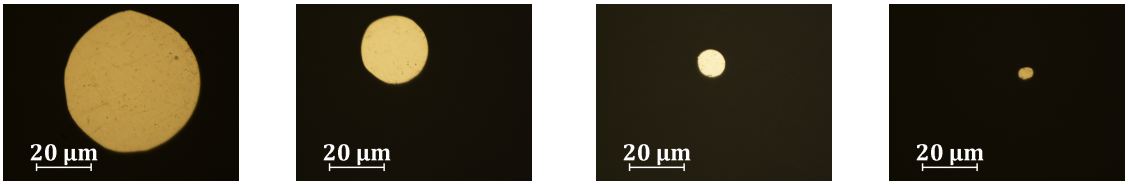

(a) $a = 25$ μm **(b)** $a = 12.5$ μm **(c)** $a = 5$ μm **(d)** $a = 2.5$ μm

Figure 2.6: Optical images of Pt microdisc electrodes. The nominal values are shown.

estimated with the limiting current ($i_{lim} = 4nFDCA$), in this work, the radius of the discs was obtained by fitting current transients as explained below.

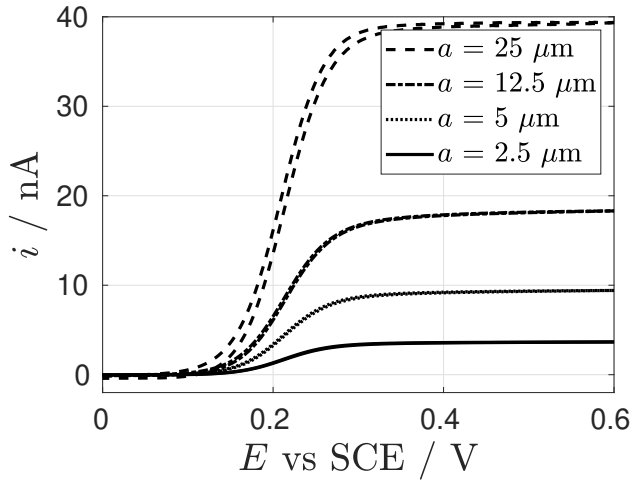

Figure 2.7: Cyclic voltammograms of Pt microdisc electrodes in a solution 5.61 mM $K_4Fe(CN)_6$ and 0.5 M KCl, the scan rate was 2 mV s^{-1}. The temperature was maintained at 25 ^{o}C.

The electrodes show deformations in their geometries that could have an impact on the diffusion controlled response in transient conditions. To test for this, chronoamperometry experiments were performed in $K_4Fe(CN)_6$. Figure 2.8 shows the current transients obtained at 0.5 V vs SCE (markers) as well as the fittings to the Mahon-Oldham equation (dashed lines). For the bigger electrodes, the fittings agree at all times, indicating that the electrodes follow the expected behaviour of a microdisc. The smaller electrode ($a = 2.5$ μm) does not show this, instead, its response is significantly different, as evidenced not only by the theoretical response but by the different slope compared to the rest of the electrodes. This could be due to a bad sealing. This is

important when applying the methodology proposed by Perry and Denuault to detect the presence of adsorbed oxygen species since they relied on the electrode following the Mahon-Oldham response at all times [1, 2]; results obtained with this electrode have to be taken with care.

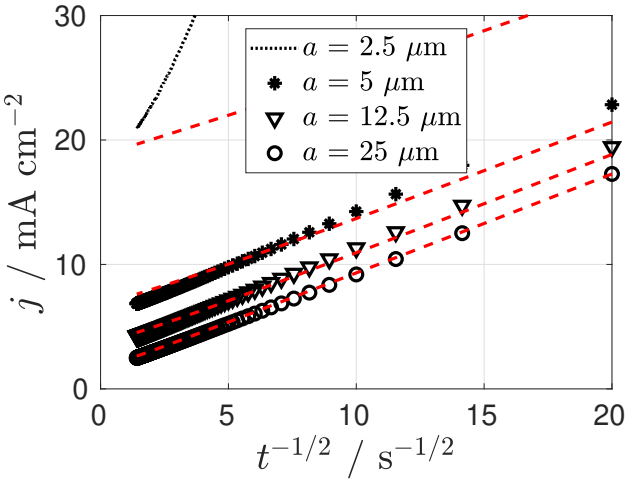

Figure 2.8: Chronoamperometry experiments (markers) in a solution 5.61 mM $K_4Fe(CN)_6$ and 0.5 M KCl recorded at 0.5 V vs SCE; the fittings to the Mahon-Oldham equation are indicated as dashed lines. The currents were normalised against the geometrical area of the electrodes and the temperature was maintained at 25 ^{o}C.

Table 2.3 shows the radii of the electrodes obtained by fitting the Mahon-Oldham equation to the chronoamperometry experiments shown in Figure 2.8. These values are used in Chapter 3 when testing for the presence of adsorbed species with the methodology proposed by Perry and Denuault.

Nominal radius	CA in $K_4(FeCN)_6$
25 μm	27.8 μm
12.5 μm	13 μm
5 μm	7 μm
2.5 μm	-

Table 2.3: Comparison of the radius of the microelectrodes obtained by fitting the Mahon-Oldham equation to current transients at 0.5 V vs SCE in 5.6 mM $K_4(FeCN)_6$ and 0.5 M KCl.

The electrodes were also characterised in H_2SO_4 to test for cleanliness and to obtain the electroactive area. Figure 2.9 shows a CV recorded with a Pt microelectrode, where the Pt surface processes can be observed. The red line shows the region used for the calculation of the electroactive area, as proposed by Biegler [34]. In this work, the area was obtained by integrating the hydrogen adsorption peaks from 0.4 to 0.05 V vs RHE after subtracting the double layer region:

$$A = \frac{\int i \mathrm{d}E}{0.77 \nu Q_H} \tag{2.2}$$

where ν is the scan rate and Q_H is the charge of adsorption of hydrogen on Pt, assumed to be 210 μC cm^{-2}. The factor 0.77 takes into account that less than a monolayer is adsorbed on Pt at those potentials [34]. [3]

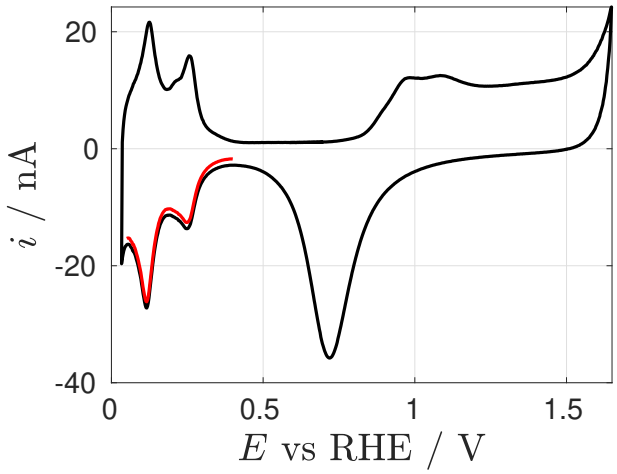

Figure 2.9: Cyclic voltammogram of a Pt microelectrode (a = 25 μm) in a 1 M H_2SO_4 solution. The CV was recorded at 0.2 V s^{-1}. The red line shows the hydrogen adsorption region used for the calculation of the electroactive area after subtracting the double layer region.

[3] In their work, Perry and Denuault calculated A by multiplying the factor 0.77 instead of dividing it. Correcting the value of the charge of adspecies that they obtained gave Q = 33 μC cm^{-2} instead of the reported 55 μC cm^{-2}.

2.4.3 Carbon fibre with Pt nanoparticles

This section presents the construction and characterisation of a carbon fibre microdisc electrode with Pt nanoparticles deposited on it. A carbon fibre ($a = 3$ μm) was introduced into a glass tube leaving less than 0.5 cm of the fibre exposed outside it. The tip of the glass tube was sealed with a flame to ensure the fibre was secure inside it, then, the sealed tip was introduced into a heating coil while vacuum was applied through the opened end; this ensured that the inner walls of the tube sealed the carbon fibre. The coil was then slowly moved through the length of the tube until approximately 1 cm of the carbon fibre was sealed. This method produced bubbles around the fibre, probably CO_2 due to the heating of the carbon fibre in an oxygen environment (see Figure 2.10a). A small amount of silver paint was introduced along with a wire to make the electrical contact. The electrode was then polished with different grades of silicon carbide paper and alumina powder in order to have a smooth finishing at the tip of the tube.

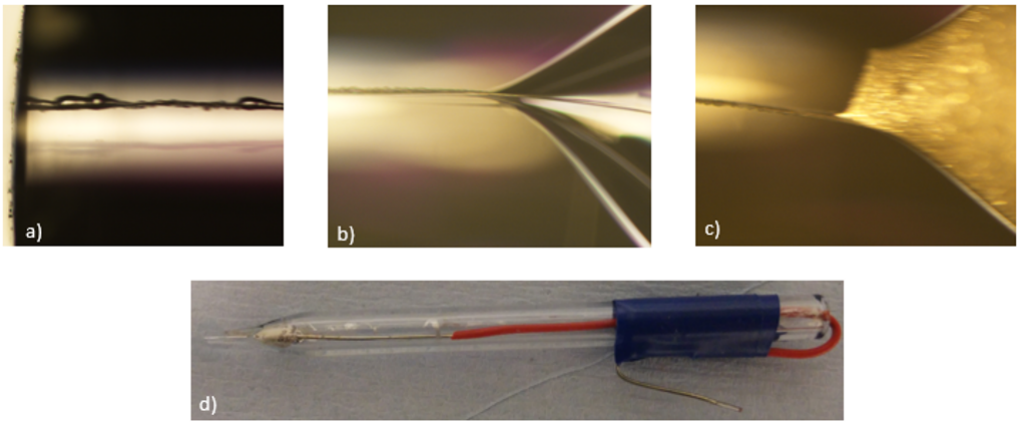

Figure 2.10: Optical images of a carbon fibre disc microelectrode. a) Tip of the sealed tube with the carbon fibre in the centre surrounded by bubbles, b) interface formed by the sealed and non-sealed part of the tube, c) electrical contact between the carbon fibre and the silver paint at the interface of the glass, d) image of the constructed carbon fibre microdisc electrode.

Pt was deposited onto the carbon fibre following the methodologies proposed by the groups of Gao and Yasin [68, 69]. The deposition was performed in a solution of 2 mM H_2PtCl_6 in 0.1 M HCl. Figure 2.11 shows a chronoamperogram in this solution at a

potential of -0.1 V vs SCE; this potential ensures that the deposition of Pt is diffusion controlled [69]. The experiment was stopped when 1 μC of charge was passed.

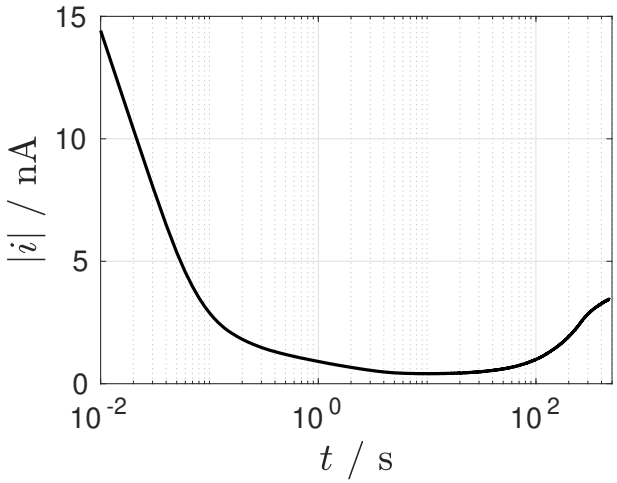

Figure 2.11: Pt deposition onto a carbon fibre microelectrode (a = 3 μm) in a solution 2 mM H_2PtCl_6 after stepping from 0.6 V to -0.1 V vs SCE. The experiment stopped when 1 μC of charge was passed.

Figure 2.12 shows a SEM image of the carbon fibre microdisc electrode after Pt deposition. Pt nanoparticles can be seen as bright spots over the surface of the electrode, the bigger nanoparticles have a diameter of 350 nm.

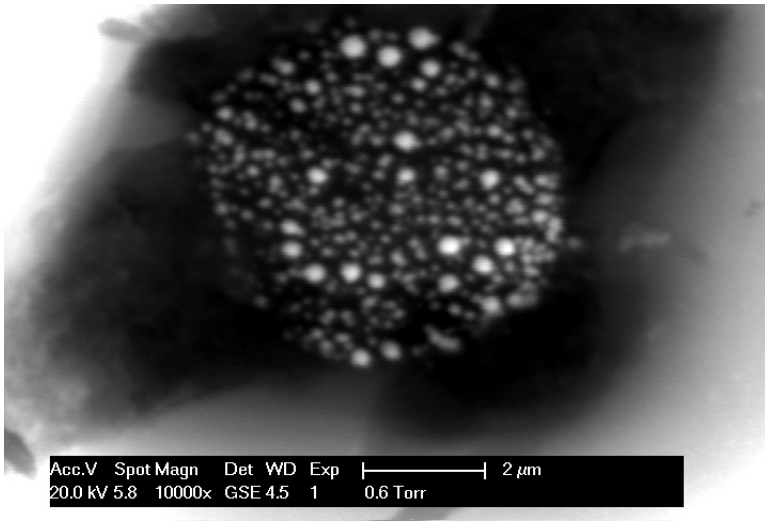

Figure 2.12: SEM image of a carbon fibre / Pt electrode with 1 μC of charge obtained by stepping from 0.6 to -0.1 V vs SCE in a solution 2 mM H_2PtCl_6 and 0.1 M HCl.

As reported by Yasin [69], the nanoparticles are well dispersed and only cover a fraction

of the fibre due to the difficulty of nucleating Pt, where the growth of the nanoparticles is preferred to the creation of new nuclei. Due to these Pt-free sites, the electrochemical response would be affected by both materials, that is, the active part of this electrode is formed by carbon and Pt. In this work, this electrode is referred to as C/Pt NPs electrode.

Figure 2.13 shows voltammograms in H_2SO_4 before and after the deposition of Pt. It can be seen that the carbon signal is not seen under these conditions, still, the presence of C should not be ignored.

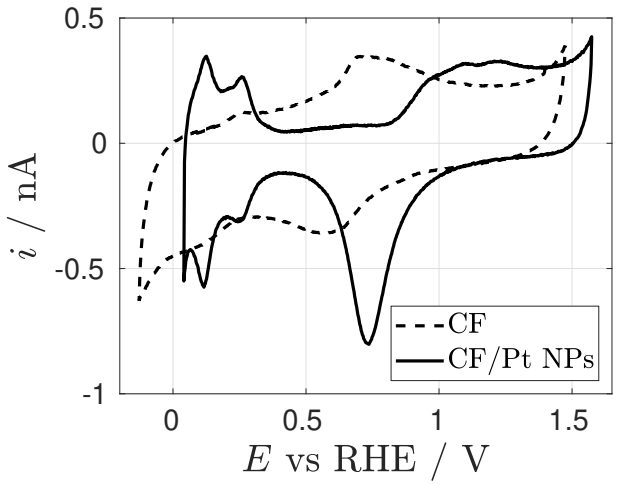

Figure 2.13: Cyclic voltammograms in a degassed solution 1 M H_2SO_4 of the carbon fibre electrodes (3 μm in radius) before and after the deposition of 1 μC of Pt. The scan rate used was 0.1 V/s.

2.4.4 Pt spherical electrode

This section presents the construction and characterisation of a Pt sphere electrode with sub-micron radius. The methodology used is based on the ones proposed by Actis and Sen [70, 71].

A pipette-puller machine Sutter P-2000 was used for pulling quartz capillaries (World Precision Instruments, ID = 0.7 mm, OD = 1 mm, l = 10 cm). The parameters to control were Heat (H = 650), Filament (F = 4), Velocity of the pulling (V = 60), Delay

before pulling (D = 150) and the Pull force applied (P = 175). As a general rule, the lower the heat, the bigger the diameter and length of the tip.

Carbon was deposited as following: the quartz pipette was introduced into a quartz capillary flooded with Ar, butane was passed through the pipette and a flame was approached to the tip (which was covered by the quartz capillary); this created a C film that filled the tip of the pipette. Electrical connection was made with silver paint. Handling these electrodes is difficult due to their fragility; to prevent electrical discharge from breaking the tips [72], a grounded band wrist was used at all times

Due to the low currents expected with this electrode, all the experiments were performed with a potentiostat PGSTAT30 with the ECD module; this module adds current ranges of 1 and 0.1 nA. Figure 2.14 shows the cyclic voltammogram of the electrode in H_2SO_4, where currents in the order of pA can be observed. Figure 2.14 also shows a cyclic voltammogram in $Ru(NH_3)_6Cl_3$ at 20 mV s^{-1}, where the typical sigmoidal shape for reactions with species in solution is observed. Assuming a disc-shaped electrode and that the RG is infinite, the diameter was calculated to be 340 nm with $i_{lim} = 4nFDCa$. It is possible that the assumption of infinite insulation is not fulfilled; due to the pulling, the diameter of the glass may be comparable to that of the electrode, if that is the case, the diameter may be overestimated due to back diffusion.

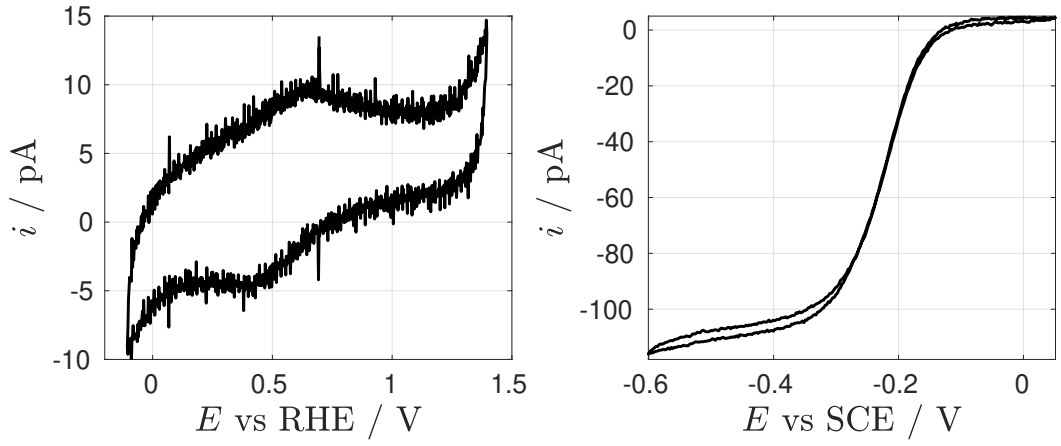

Figure 2.14: Cyclic voltammogram of a Quartz/C nanodisc electrode. Left: 1 M H_2SO_4 at 0.2 V/s and right: 5 mM $Ru(NH_3)_6Cl_3$ and 0.5 M KCl at 0.02 V s^{-1}.

Pt deposition was performed on the carbon nanoelectrode by cycling the potential in

a solution 2 mM H_2PtCl_6 and 0.1 M HCl at 20 mV/s for three consecutive cycles. The total deposition charge was 58 nC. Figure 2.15 shows the voltammogram; the first cycle shows that a high overpotential is needed to start the deposition; with consecutive cycles the current increases due to the grow of Pt on previously deposited Pt layers.

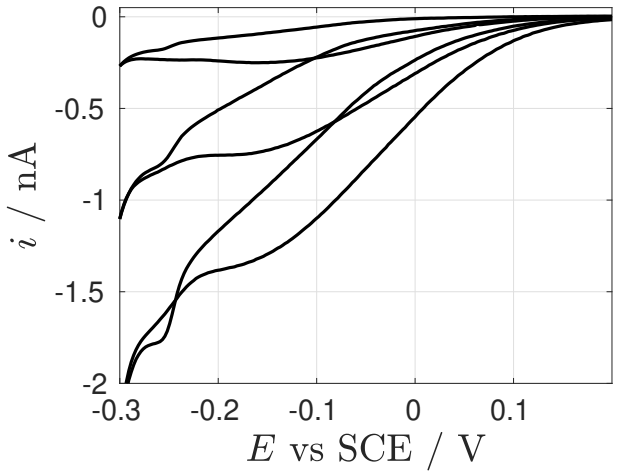

Figure 2.15: Electrodeposition of Pt by cyclic voltammetry on a Quartz/C nanoelectrode in a solution 2 mM H_2PtCl_6 and 0.1 M HCl at 0.02 V s^{-1}.

The electrode was also characterised in $Ru(NH_3)_6Cl_3$, Figure 2.16 shows a voltammogram recorded at 1 V s^{-1}; the fact that the sigmoidal shape is maintained even though the scan rate used is high refers to the high rate of mass transport achieved with this electrode. Assuming a perfect sphere, the calculated radius was 0.49 μm (Equation 1.1).

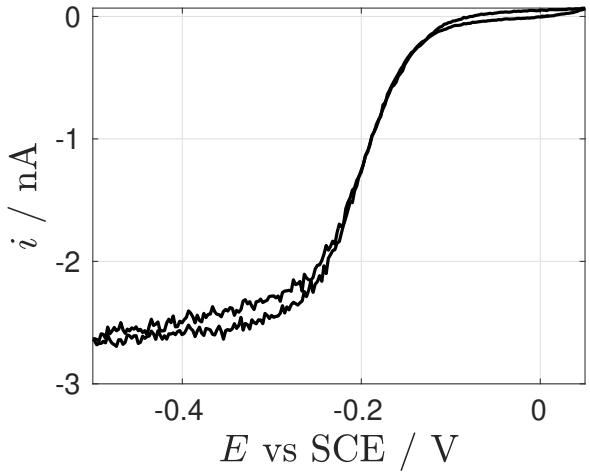

Figure 2.16: Cyclic voltammogram of a Quartz/C/Pt spherical electrode in a solution 5 mM $Ru(NH_3)_6Cl_3$ with 0.5 M KCl at 1 V s^{-1}.

Figure 2.17 shows a SEM image of this electrode, where it can be seen that the deposited Pt covers the tip of the electrode, that is, no carbon is exposed. The measured radius of the electrode from the SEM image was $r = 0.45$ μm; the difference with the radius obtained from $Ru(NH_3)_6Cl_3$ is probably due to the limiting current assuming a perfect sphere. In this work, the radius obtained from the SEM measurements was used.

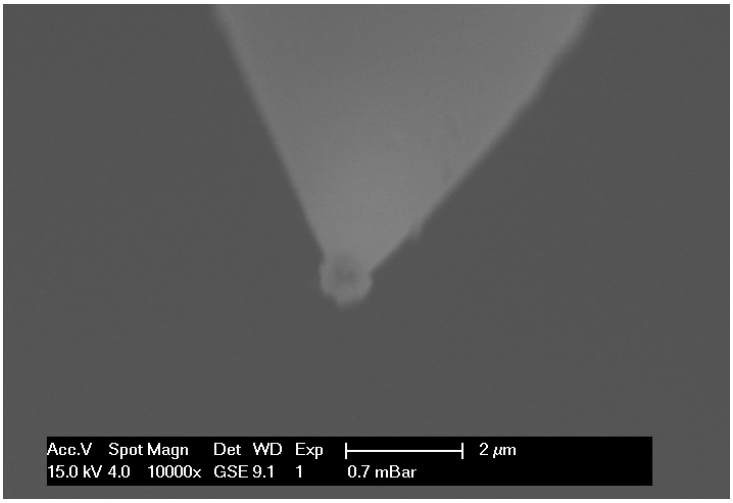

Figure 2.17: SEM image of a Quartz/C/Pt sphere electrode with $r = 0.45$ μm.

2.5 Potential waveform

Perry and Denuault reported that in order to obtain reliable and reproducible results regarding the detection of the adsorbed oxygen species, the electrode has to be treated electrochemically to ensure that every experiment is started with similar electrode history [1, 2]. They proposed the use of the potential waveform shown in Figure 2.18, and it consists in three main parts: electrochemical cleaning, resting and stepping.

During the cleaning, the electrode is swept at 500 mV s^{-1} between hydrogen evolution and oxide formation. The upper cleaning potential E_{up} was selected in the lower potential region of oxide formation to oxidise impurities that may be present in the electrode, while the lower cleaning potential E_{low} was selected in the hydrogen evolution region to ensure that all the formed oxide was completely reduced. The last anodic sweep was stopped at the rest potential; this potential was selected in the region observed by Perry and Denuault to allow the oxygenated species to adsorb, between 0.8 V and 1.2 V vs RHE. The rest potential also ensured that the oxygen concentration at the surface of the electrode was re-established after being affected during the cleaning. Lastly, the step potential was selected anywhere along the ORR wave; the current transient obtained during the step potential was analysed to study the adsorbed oxygen species in transient conditions.

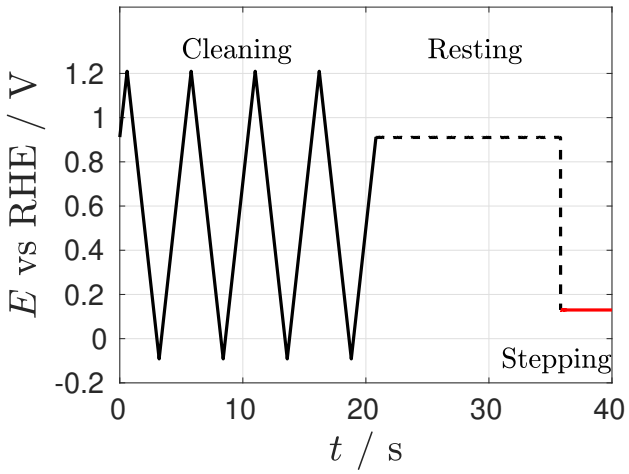

Figure 2.18: Potential waveform used by Perry and Denuault [1, 2, 20] and in this work to study the adsorbed oxygen species.

In this work, variations of the potential waveform from Figure 2.18 were used; when needed, the potential waveform is shown with the differences specified.

2.6 Oxygen parameters

The concentration and diffusion coefficient of oxygen are important parameters when studying the oxygen reduction reaction. In this section, the measurement and calculation of these parameters is presented.

2.6.1 Concentration

The concentration of oxygen in an aqueous solution has a dependence on temperature, atmospheric pressure and the species in solution; here, the concentration was calculated with Henry's law [73]:

$$C = k_H P(\mathrm{O_2}) \tag{2.3}$$

where C is the concentration of oxygen, k_H is the Henry's law constant and $P(\mathrm{O_2})$ is the partial pressure of oxygen. k_H and $P(\mathrm{O_2})$ are given by:

$$k_H = k_{298K}\ \exp[-(\Delta H_{soln}/R)(1/T - 1/298)] \tag{2.4}$$

$$P(\mathrm{O_2}) = P_{atm} - P_{H2O} \tag{2.5}$$

where k_{298K} is 1.2 mM atm^{-1}, ΔH_{soln} is the dissolution enthalpy of oxygen, $-\Delta H_{soln}/R$ = 1500 K [73], T is the temperature in K, P_{atm} is the atmospheric pressure (when using gas saturated solutions) and P_{H2O} is the partial pressure of water vapour (0.0313 atm). At 298 K (25 ^{o}C), Equation 2.3 can be simplified to:

$$C = k_{298K}(P_{atm} - P_{H2O}) \tag{2.6}$$

When using air, a different equation was used to calculate the concentration of oxygen [1, 74]:

$$C_{air} = \frac{C_{760}(P_{atm} - P_{H2O})}{760 - P_{H2O}} \tag{2.7}$$

where C_{air} is the concentration of oxygen when using air, C_{760} is the saturation concentration of oxygen at 760 mm Hg (24.86 μmol cm^{-3}) and P_{atm} and P_{H2O} are expressed in mm Hg. In this work, the concentration of oxygen was estimated by using Equations 2.6 and 2.7 when using O_2 and air respectively.

2.6.2 Pressure sensor

The atmospheric pressure was obtained from a home-made pressure and temperature sensor. Table 2.4 shows the list of electronic components. The microcontroller was programmed with Equation 2.6 to display the appropriate concentration of oxygen after measuring the pressure; see Figure 2.19 for an image of the constructed sensor.

Component	Model
Microcontroller	ELEGOO Nano v3
LCD display	ELEGOO 1602
Air pressure sensor	kwmobile BMP180
Mini USB cable	Startech

Table 2.4: List of electronic components for the pressure sensor.

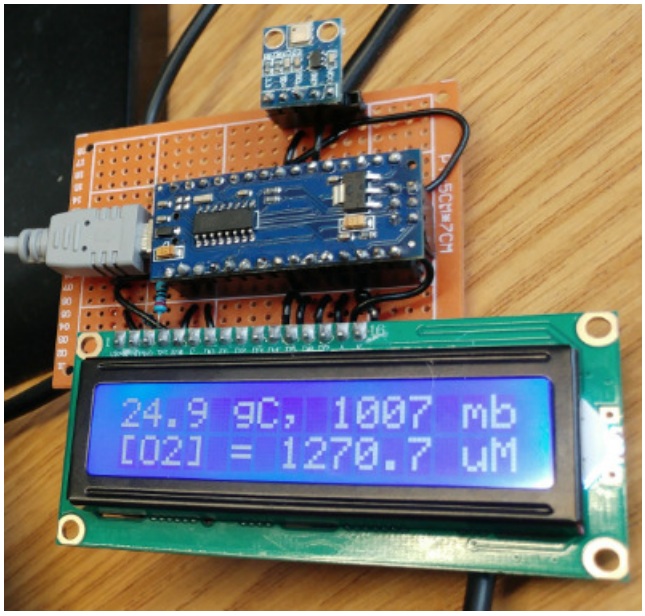

Figure 2.19: Constructed pressure sensor.

2.6.3 Diffusion coefficient

The diffusion coefficient of oxygen was measured by following the methodology proposed by Denuault *et al* [9]. They used microelectrodes to record current transients at a potential that ensured a diffusion controlled rate and normalised it by the experimental limiting current; after the normalisation, the current transient is proportional to $t^{-1/2}$. Using the expression proposed by Shoup and Szabo, they established that at long times ($Dt/a > 1$), the current can be simplified to:

$$\frac{i}{i_{ss}} = 1 + \frac{2a}{\pi^{3/2}\sqrt{Dt}} \tag{2.8}$$

Equation 2.8 can be used to measure D from the slope with an error within 1 %. In this work, the current transients were recorded using the potential waveform shown in Figure 2.18. Figure 2.20 shows a current transient recorded in a $HClO_4$ O_2-saturated solution; a good agreement between the experimental current and the fit to Equation 2.8 can be seen. A list of diffusion coefficients calculated with this methodology are shown in Table 2.5.

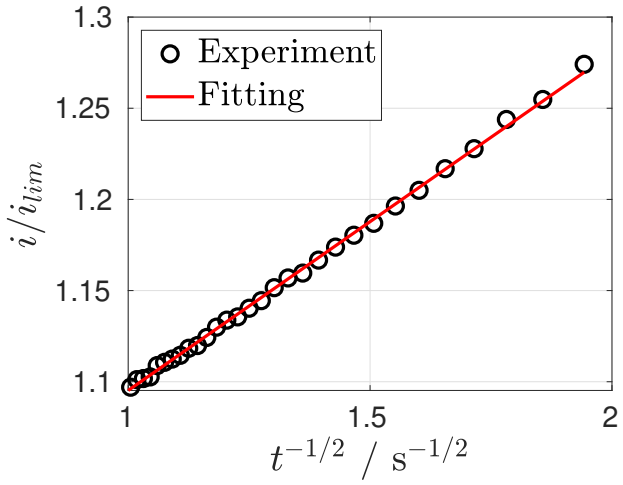

Figure 2.20: Current transient recorded with a Pt microdisc electrode (a = 25 μm) in a 0.1 M $HClO_4$ O_2 saturated solution. E_{step} = 0.4 V vs RHE. The waveform shown in Figure 2.18 was used. The red line shows the fit to Equation 2.8.

Solution	D/ cm^2 s^{-1}
0.1 M $HClO_4$	2.5x10^{-5}
0.1 M $KClO_4$	2.3x10^{-5}
0.1 M NaOH	2.6x10^{-5}

Table 2.5: Diffusion coefficients of O_2 obtained by fitting Equation 2.8 to current transients. The temperature was maintained at 25 ^{o}C.

2.7 Scanning electrochemical microscopy

Some experiments with a scanning electrochemical microscope were performed. This section presents the instrumentation as well as the alignment of the tip and the substrate. Specific conditions and waveforms are presented in Chapter 4.

2.7.1 Electrochemical cell and instruments

A home-made glass electrochemical cell was used. To allow movement of the tip, the cell was kept open at all times. When ORR experiments were needed, air was introduced by first passing it through a Dreschell bottle. A glass rod (a = 7 mm, l = 7 cm) was polished with sand paper (600 to 1200) and alumina (5 μm to 0.3 μm) and used as a substrate for negative feedback. The working electrode consisted on a Pt disc (a = 25 μm) with RG = 50. A RHE from Gaskatel was used in all SECM experiments.

A 3-axis micropositioner from PI-Instruments was used; the axis have a precision of 0.1 μm with a maximum travel range of 25 mm. The software of the instrument allows for the control of the micropositioner and can generate linear movement at a specified velocity. As the microsopitioner is not interfaced with a potentiostat, a PGSTAT101 from Autolab was used and programmed separately to perform the electrochemical measurements. Figure 2.21 shows an image of the SECM setup.

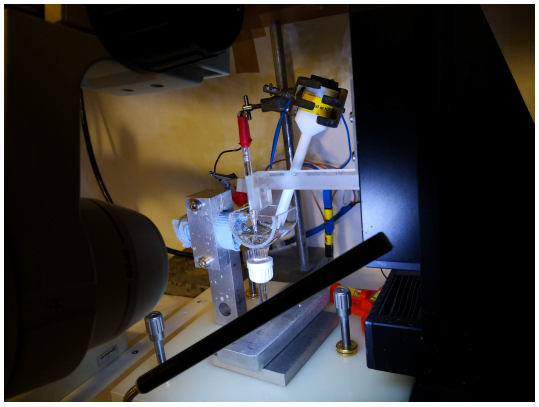

Figure 2.21: Image of the SECM setup used.

2.7.2 Alignment

A levelling stage with three high precision screws (100 TPI Adjustment Screw) was constructed and used to align the substrate with the microelectrode. An optical microscope (Olympus, SZ-STB1) was used to obtain live video in order to position the tip with more precision. After an initial alignment done by eye, line scans were obtained to improve it, see Figure 2.22 for the potential waveform and details about the movement, this waveform was also used to record approach curves.

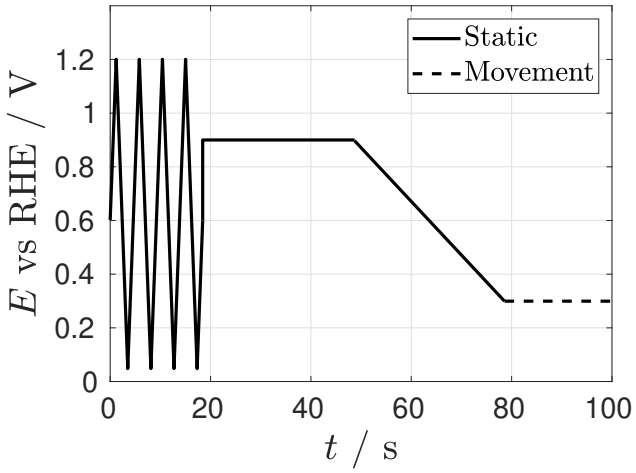

Figure 2.22: Potential waveform used to align the microelectrode to the substrate. Cleaning, resting and sweeping were performed in a static position while the electrode was moved in any of the three axis during the step at 0.3 V.

During the alignment, O_2 from air was used as a redox mediator. First, the electrode was positioned away from the substrate (bulk position). Cleaning, rest and sweep were performed in the bulk, the sweep at 20 mV s^{-1} was performed to obtain the steady state response. After the linear sweep, the potential was held at the ORR plateau and the electrode was approached to the substrate at a speed of 2 μm s^{-1}. The movement was stopped when the current decreased to about 50% of the bulk current. Line scans were then obtained in either X or Y axis using the same potential waveform and speed. During the line scans, changes in the current give information about the alignment between the substrate and the tip. For a perfectly flat and aligned system, the current would remain constant during the movement; any changes in the current

(either positive or negative) would indicate a tilt on the substrate, requiring manual adjustment using the high precision screws. 2.23 shows linear scans in X and Y with a tilted substrate.

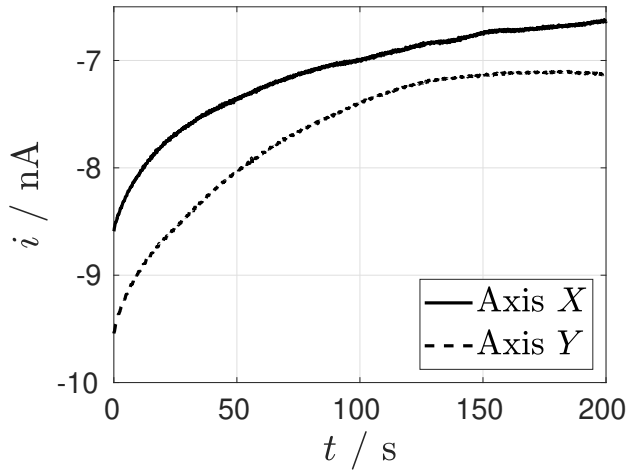

Figure 2.23: Line scans in X and Y recorded with the potential waveform from Figure 2.22.

Once the current was found to remain constant, approach curves were recorded at 2 μm s^{-1}. Figure 2.24 shows an approach curve recorded with an aligned system where the fit to Equation 1.19 is also shown. In this work, a well aligned system was considered when the current was 30 % that of the current at the bulk.

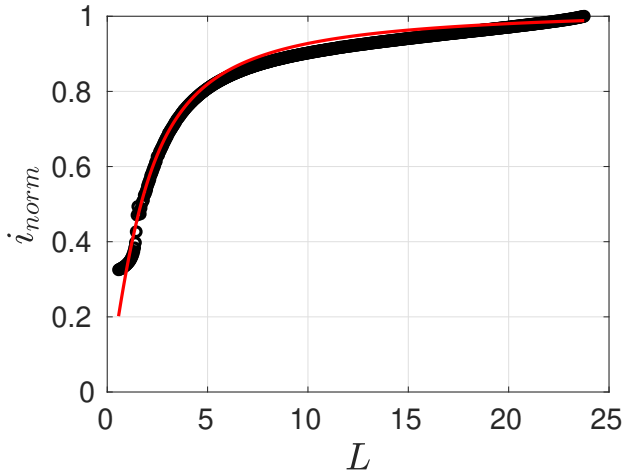

Figure 2.24: Approach curve recorded with the waveform shown in Figure 2.22. The red solid line shows the fitting to Equation 1.19.

Chapter 3

Reduction of oxygenated species at high rates of mass transport

This Chapter presents results regarding the oxygen reduction reaction and the reduction of adsorbed oxygen species when high rates of mass transport are used. The value of k_m is varied at the steady state by using different sizes of Pt microelectrodes and at the transient state by recording the current as a function of time. Section 3.1 shows results at the steady state, where the adspecies can not be detected and the results solely describe the response of the ORR at different values of k_m; kinetics effects and changes in n_{app} are discussed in terms of mass transport. Section 3.2 uses the transient methodology proposed by Perry and Denuault to detect the presence of adsorbed species [1, 2]; values of n_{app} and Q are presented as a function of the size of the electrodes and the sampling time. This section also presents results with Pt nanoparticle electrodes, where their high rates of mass transport is exploited to discriminate the reduction of dissolved oxygen species and minimise its contribution to the overall current. Finally, Section 3.3 proposes a different methodology based on potential sweeps to detect the presence of adsorbed species without relying on a theoretical mass transport controlled current. Overall, this Chapter improves the results obtained by Perry [3] by exploiting the mass transport regime to study the presence of the adsorbed oxygen species.

3.1 Oxygen reduction reaction with microelectrodes

The reduction of oxygen on Pt electrodes is a complicated reaction that can have several pathways [64]. In the direct pathway, O_2 is directly reduced to H_2O with the transfer of $4e^-$. Indirect routes produce intermediates, the most accepted one being H_2O_2 in a $2e^-$ transfer reduction; this in turn can be further reduced to H_2O with $2e^-$, giving an overall $4e^-$ reduction. Some groups have shown that in fact, the measured number of electrons can have any intermediate value between 2 and 4 depending on the mass transfer coefficient used [4, 5, 75]. The value of k_m controls the amount of H_2O_2 that can be reduced towards H_2O, this is because a high mass transport rate allows the H_2O_2 to leave the vicinity of the electrode before it can be reduced again. This section revisits these results by using different sizes of Pt microdisc electrodes to reduce oxygen at the steady state. The results show a good agreement with previous studies performed with rotating disc electrodes, microelectrodes and nanoelectrodes [4, 5, 75].

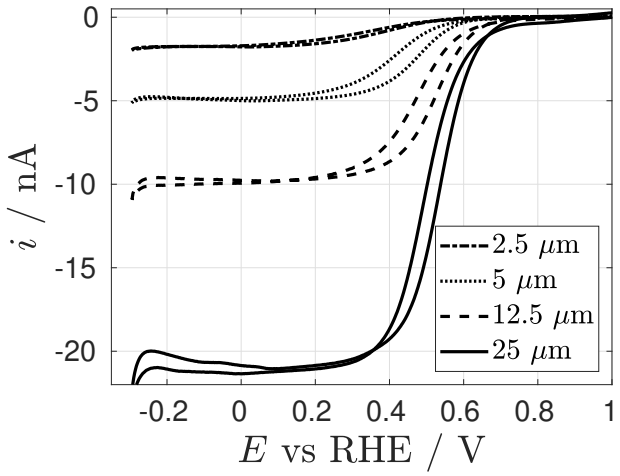

Figure 3.1: Cyclic voltammograms obtained at 0.2 V s^{-1} in an aerated solution of 0.1 M $KClO_4$ with different microelectrode radii.

Cyclic voltammograms in aerated $KClO_4$ were obtained with microelectrodes of different sizes. Figure 3.1 shows these results; the limiting currents obtained decrease according to the radius of the electrode, as expected for a diffusion controlled process ($i_{lim} = 4nFDCa$). The hysteresis seen between the forward and backward currents

has been studied by several groups and is explained in terms of the state of the surface during the oxygen reduction reaction [36, 37, 48]. In the forward sweep the electrode is partially oxidised making the ORR more difficult to proceed; as the overpotential is increased, the oxide is eventually completely reduced, ensuring that during the backward sweep the electrode is free of oxide making it more active towards the reduction of oxygen. This difference in the state of the surface gives rise to the hysteresis seen in Figure 3.1: at the same potential the current is higher during the forward sweep (oxide-free) than during the anodic one. The voltammograms also show a decrease in current in the hydrogen region, this has been explained in terms of the competition for free Pt active sites between the adsorption of hydrogen and the reduction of molecular oxygen and is highly dependent on mass transport due to the production of H_2O_2 [76, 77, 78]. The features observed (hysteresis, hydrogen adsorption) can be used as an indicator of the cleanliness of the system, impurities in the solution can block the active sites preventing these processes to occur. Systems with high rates of mass transport are specially sensitive to cleanliness since even trace levels of impurities can block the surface during the timescale of the experiments [59].

Figure 3.2 shows the oxide-free voltammograms normalised by their respective limiting currents. Kinetic limitations can be seen and are attributed to the high value of the mass transfer coefficient that can be achieved with microelectrodes. For comparison, a microdisc with $a = 12.5$ μm would give $k_m = 0.01$ cm s^{-1}, while to achieve the same value with RDE, a rotation of 2500 RPM is needed[1]. This implies that, unless high speeds are used with rotating disc electrodes, it will not be possible to observe kinetic limitations due to mass transport. Interestingly, the onset potential for the hydrogen evolution reaction does not seem to be affected by the size of the microelectrode, indicating that this reaction is considerably faster than the oxygen reduction reaction, requiring higher rates of mass transport for it to show kinetic limitations.

[1] k_m calculated with $D = 1\text{x}10^{-5}$ cm^2 s^{-1} and $N = 0.01$ cm^{-2} s^{-1}.

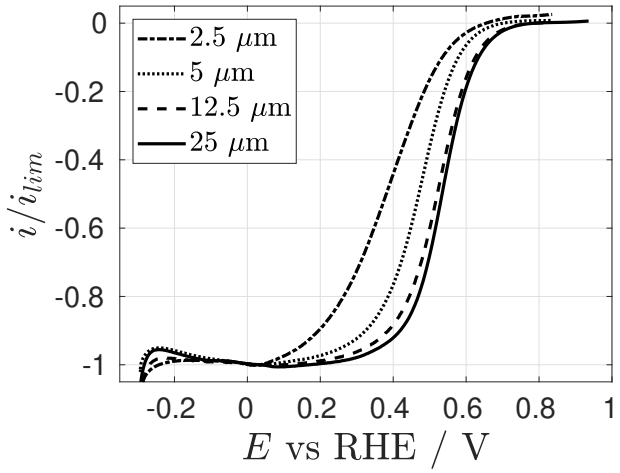

Figure 3.2: Backward sweeps from Figure 3.1 normalised by the limiting current taken at $E = 0$ V vs RHE.

Figure 3.3 shows the oxide-free voltammograms normalised by the theoretical limiting current assuming $n = 1$; this normalisation procedure reveals an apparent number of electrons in the plateau of the voltammograms. For a simple one electron reaction, this would make the voltammograms collapse into each other, with the plateau being equal to 1, and revealing possible kinetic limitations, similar to the normalisation by the experimental limiting current, Figure 3.2. Instead, the ORR voltammograms show a dependence on the microelectrode radius, with lower values of n_{app} as the electrode size decreases. For the specific case of the oxygen reduction reaction, this has been explained in terms of mass transport and the intermediate steps of the reaction [4, 5, 75]. Studies performed with rotating disc electrodes at low rotation rates showed that the number of electrons that participate in the reaction is 4, indicating a complete reduction of O_2 towards H_2O by either the direct path or the indirect path (O_2 reduced to H_2O_2 and then to H_2O). When increasing the rate of mass transfer, the H_2O_2 produced during the indirect path can leave the vicinity of the Pt surface before being reduced again, decreasing the apparent number of electrons towards 2.

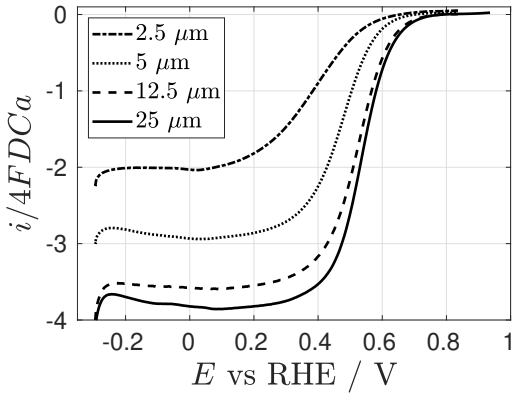

Figure 3.3: Backward sweeps from Figure 3.1 normalised by $4FDCa$.

Here, the effect of mass transport on the oxygen reduction reaction was tested by using different sizes of Pt microelectrodes. The bigger electrodes showed a higher ability to fully reduce O_2 towards water due to the lower mass transport regime that prevents H_2O_2 to leave the surroundings of the electrodes before it can be reduced to H_2O. The irreversibility degree of the reaction, as well as the limiting currents obtained showed the expected behaviour as a function of the size of the electrodes. The effect of mass transport on n_{app} has also been observed by some groups with the use of micro and nanoelectrodes [4, 5, 75]. In all cases, this has been done at the steady state, although it is expected that a similar trend should should occur on transient conditions, since on a chronoamperometric experiment, the mass transfer coefficient decreases as time is increased, and so n_{app} should be a function of time.

3.2 Detection of adsorbed oxygen species

Recently, Perry and Denuault detected the presence of oxygen containing species pre-adsorbed on Pt when the electrode was exposed to molecular oxygen [1, 2]. They showed that the adspecies could only be detected in the millisecond scale and that its coverage was highly dependent on the presence of spectator species (ClO_4^-, Cl^-, I^-, Br^-) and on the bulk concentration of oxygen. To detect the adspecies they compared an experimental current transient with a theoretical response that assumed diffusion control under transient conditions. They observed a disagreement at the millisecond

scale that could only be explained as the reduction of an oxygen surface process. In this section, the methodology proposed by Perry and Denuault is used to detect the presence of the adspecies with different microelectrode sizes. The analysis of current transients obtained at the ORR plateau is presented, followed by the construction and analysis of sampled current voltammograms to elucidate the apparent number of electrons and the presence of the adsorbed species in transient conditions.

3.2.1 Current transients at the ORR plateau

Perry and Denuault reported the presence of adsorbed species by comparing their experimental response recorded at a potential on the ORR plateau with the theoretical response given by the Mahon-Oldham equation, Equation 1.9 [1, 2]. The main assumption of this equation is that the reaction is limited by diffusion. One can see from Figure 3.3 that this is true at potentials between 0 and 0.2 V; potentials more negative than 0 V show a decrease in current due to the competition with the hydrogen adsorption [76, 77, 78]. The waves also show kinetic limitations, with the smallest electrode showing a plateau at similar potentials as the adsorption of hydrogen. For the following analysis, as a compromise, a potential of 0.17 V was selected for all the electrodes.

The potential waveform used is similar to the one used by Perry and Denuault [1, 2], shown in Figure 3.4 and it consists on three main parts. First, the potential was cycled at 500 mV s^{-1} to pre-condition the electrode and to ensure that the surface had a similar history between experiments. The second region corresponds to a resting state, where the electrode was held at 0.91 V and where Perry and Denuault showed that the oxygenated species were allowed to adsorb. The rest potential also ensures that the concentration of oxygen around the electrode is re-established after the cleaning part of the waveform. The stepping region corresponds to the stripping of the adspecies and where the current is taken for analysis. A potential on the ORR plateau was selected in order to compare it with the Mahon-Oldham equation that assumes diffusion controlled. This potential waveform was used in all the transient experiments used in this section.

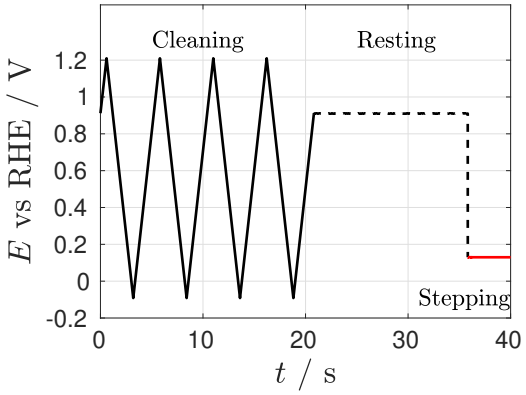

Figure 3.4: Potential waveform applied to record current transients. Cleaning: four cycles at 500 mV s^{-1}. Resting: 0.91 V for 15 s. Stepping: 1 s at 0.17 V vs RHE, the time of the stepping section was increased for visualisation purposes.

Figure 3.5 shows the Cottrell plots for a current transient obtained with a Pt disc electrode ($a = 25$ μm) and the theoretical current transient obtained by fitting the Mahon-Oldham equation, Equation 1.9, for $t > 400$ ms. As reported by Perry and Denuault [1, 2], at short times, an experimental extra current is visible that is evidence of the adspecies being reduced; as time progresses, both, the experimental and theoretical current agree, suggesting that the adspecies have been completely reduced and that the current is limited by the diffusion of molecular oxygen towards the electrode.

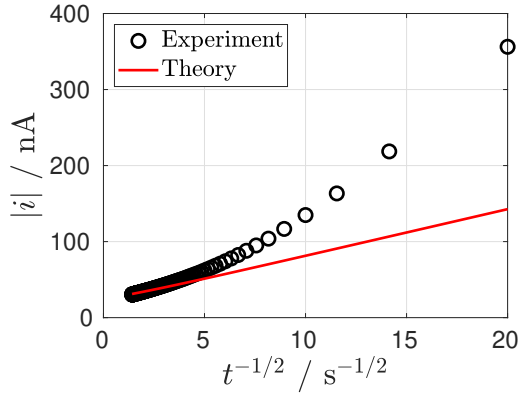

Figure 3.5: Cottrell plots for the reduction of oxygen using a Pt disc electrode ($a = 25$ μm) at 0.17 V vs RHE after the preconditioning waveform was applied. The solid line shows the current transient fitted using the Mahon-Oldham equation. An air saturated 0.1 M $KClO_4$ solution at 25 ^{o}C was used. The plots shows the average of 5 repetitions.

From the fitting at long times ($t > 400$ ms), it is possible to elucidate the apparent number of electrons, since the current is not being affected by the presence of the adspecies any more. Figure 3.6 shows the values of n_{app} obtained for different sizes of Pt microdisc electrodes by fitting the Mahon-Oldham equation from $t > 400$ ms. The trend of decreasing n_{app} as the radius of the electrode is decreased is consistent with previous works [4, 5, 75] and Figure 3.3 and is due to the high mass transport rates that can be achieved with small microdisc electrodes which prevent the ORR to continue with the full 4-electron pathway.

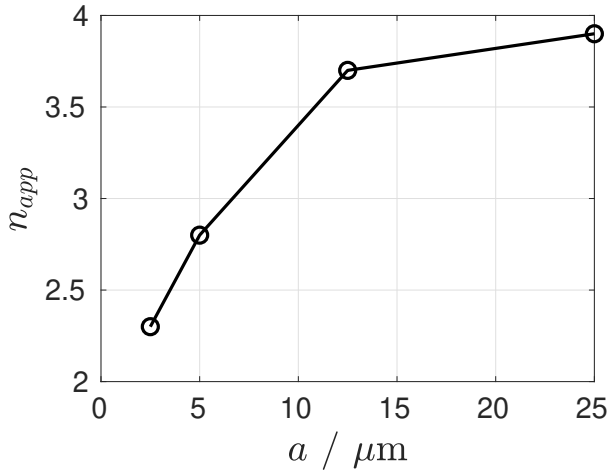

Figure 3.6: Dependency of n_{app} on the radius of the electrode. The values were obtained by fitting the Mahon-Oldham equation for $t > 400$ ms. See Figure 3.6 for experimental details. The x axis shows the nominal values of the radii.

The difference in current seen at short times can be integrated and normalised against the electroactive area to obtain a charge density of adsorption, Q. According to Perry and Denuault [1, 2], with a 12.5 μm Pt electrode, an extra charge of about 33 μC cm^{-2} can be obtained, and it corresponds to about 0.1 monolayers of adsorbed oxygen[2]. This was done here with the different sizes of Pt microelectrodes, and the results are shown in Figure 3.7.

[2]This was calculated assuming $n = 2$.

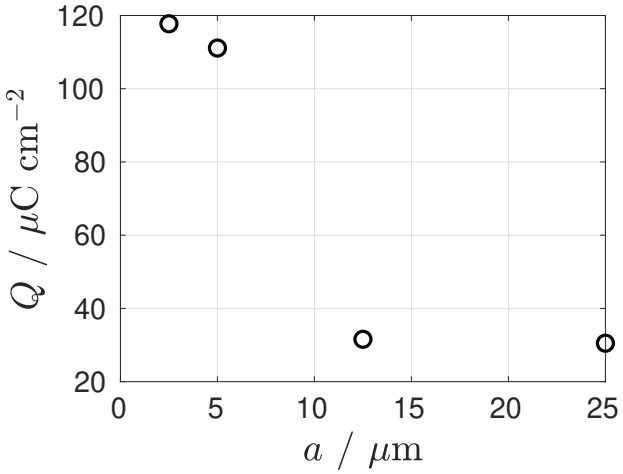

Figure 3.7: Charge density of adsorption for different sizes of Pt microdisc electrodes. The values were obtained by integrating the difference between the experimental and theoretical current transients and dividing it by the electroactive area. The highest standard deviation was obtained for the 5 μm electrode with $\sigma = 2.5$ μC cm^{-2}. See Figure 3.5 for experimental details.

With the smaller electrodes, the extra charge is almost three times higher than the reported value; the reason for this difference is attributed to the difficulty to obtain a true microdisc behaviour under transient conditions since the construction of these small electrodes is not trivial: the bad handling and sealing of the wires can potentially deform them, generating an ellipse shape instead of a circular one. Since with microelectrodes the edge effect dominates at long times, the steady state condition is still achieved with these deformed electrodes, meanwhile, the transient behaviour will not be consistent with the Mahon-Oldham equation due to deviations in the diffusion field at intermediate times.

This section presented the analysis of current transients at the oxygen reduction reaction plateau with different sizes of Pt microelectrodes. It was shown that, in agreement with Perry and Denuault [1, 2], a charge density for adsorption was obtained with a range of different sizes of Pt microelectrodes. At long times, fitting to the Mahon-Oldham equation revealed the expected dependency of n_{app} on the mass transfer coefficient at the steady state, in agreement with other reports [4, 5, 75] and with Figure 3.3.

3.2.2 Sampled current voltammetry

Perry and Denuault also showed that the extra current can be seen when applying different potential steps along the oxygen reduction reaction wave [1, 2]. They observed this by constructing sampled current voltammograms and normalising them against the Mahon-Oldham equation, taking $n = 1$; this procedure revealed values of n_{app} higher than 4 at short times, which indicated the presence of an extra process. As mentioned previously, under the steady state, the apparent number of electrons has an inverse dependency on the mass transfer coefficient [4, 5, 75], and a similar behaviour would be expected under transient conditions. The values for n_{app} observed by Perry and Denuault were clearly not following this trend, ruling out the possibility of this being due to the higher rates of mass transport achieved in transient conditions, instead, the presence of an extra process at short times (the reduction of oxygen adsorbed species) was proposed. It is important to note that the Mahon-Oldham equation assumes diffusion control, that is, it reveals the apparent number of electrons only at the ORR plateau. To obtain n_{app} in the kinetic and mixed controlled regions, a different equation is required. Perry and Denuault obtained a generalised equation for microelectrode sampled current voltammograms of species in solution [20], but its use in the ORR is not possible due to the reaction involving intermediates and surface processes that complicate the response. Qualitatively, they observed that, after normalisation assuming $n = 1$, the SCVs showed an increase in current at all potentials, similar to what occurs at the ORR plateau; they suggested that this was an indication of the presence of adsorbed species and that the fact that the potentials correlate well with the potentials for the ORR also suggests that the adsorbed species were oxygenated in nature. In this section, the same analysis of the sampled current voltammograms was performed for different microelectrode sizes to test for the presence of the adsorbed species under different rates of mass transport and electroactive areas. Since with smaller microelectrodes the steady state is reached faster, qualitatively it is expected that deviations from it at long times would indicate the presence of the adspecies. Quantitatively, the analysis is more complicated. The reduced area of the electrodes would contribute to lower coverages of the adspecies, and if the rate of the

reaction is fast, it may not be possible to detect them. Then, a compromise between the size of the electrode, the electroactive area and the potential is needed. Sampled current voltammograms along the ORR wave were recorded following the methodology proposed by Perry and Denuault [1, 20].

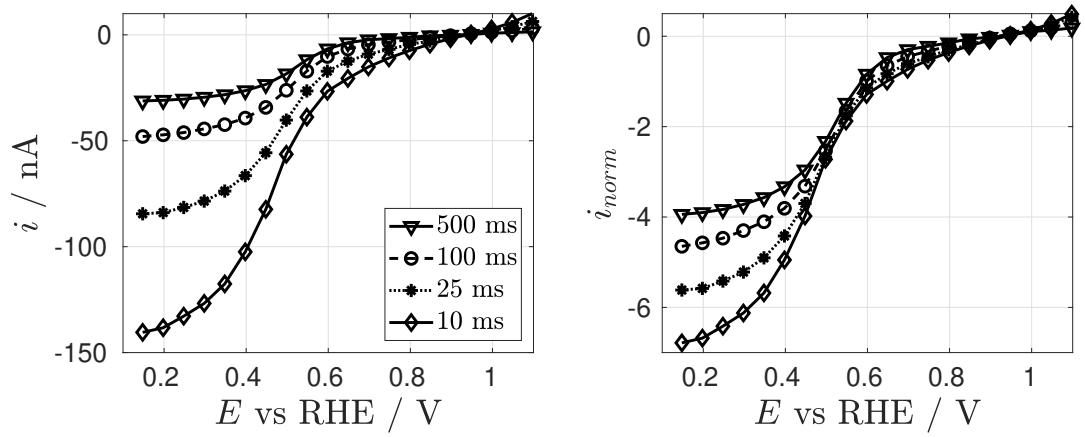

Figure 3.8: Left: Sampled current voltammograms and right: normalised SCVs for the ORR using a 50 μm diameter Pt disc electrode using the waveform shown in Figure 3.4; the Mahon-Oldham equation was used for the normalisation assuming $n = 1$. An air saturated 0.1 M $KClO_4$ solution at 25 ^{o}C was used. The legends refer to the sampling times for each voltammogram.

Figure 3.8 shows sampled current voltammograms and their normalised versions obtained with a Pt electrode of 25 μm in radius. As already reported by Perry and Denuault (with $a = 12.5$ μm), under the conditions studied here (aerated 0.1 M $KClO_4$, at the millisecond scale, with Pt microdiscs), at short times ($t < 150$ ms) an extra current is seen on the whole of the oxygen reduction reaction wave and is related to the reduction of pre-adsorbed oxygen species. The presence of this extra current is evidenced by the fact that the normalised sampled current voltammograms show that the value of n_{app} increases with increasing sampling time, surpassing the 4 e^- reduction expected by the ORR. The low overpotential region on Figure 3.8 shows the increase in current with decreasing sampling time that is attributed to the adsorbed species. For a species in solution, this region would show kinetic limitations for shorter times due to the higher rates of mass transport[3]. Perry and Denuault did not observe this with

[3]This would make the voltammograms more drawn out.

their electrodes ($a = 12.5$ μm), probably due to a higher current response of the adspecies than that of the molecular oxygen. To test this, a range of microelectrode sizes were used, with the assumption that a smaller electrode would have a lower number of active sites for the adspecies, contributing less to the overall current.

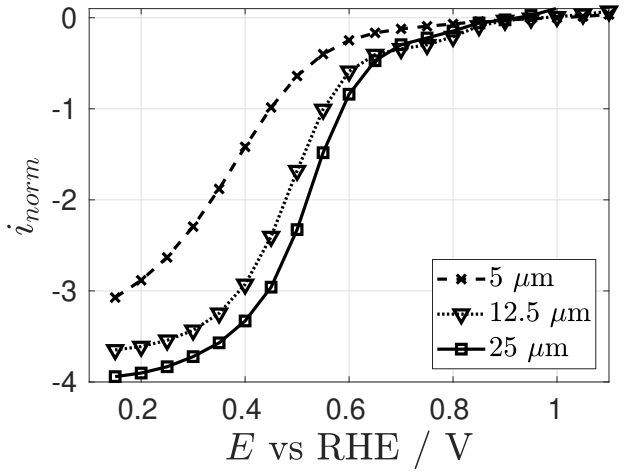

Figure 3.9: Normalised sampled current voltammograms using different sizes of Pt microdisc electrodes at 500 ms. The normalisation was performed by dividing the current transients with the Mahon-Oldham equation assuming $n = 1$. See Figure 3.8 for experimental details.

Figure 3.9 shows sampled current voltammograms for three sizes of microdisc electrodes sampled at 500 ms. It is believed that at this timescale, the adsorbed species are completely reduced and true steady state is achieved. This is confirmed by the fact that the plateaus of the normalised sampled current voltammograms show values similar to the values of n_{app} from Figure 3.3. Similar to the results with linear sweeps (Figure 3.2), the SCVs show a negative shift in potential due to kinetic limitations, as expected for electrodes of these sizes under steady state conditions.

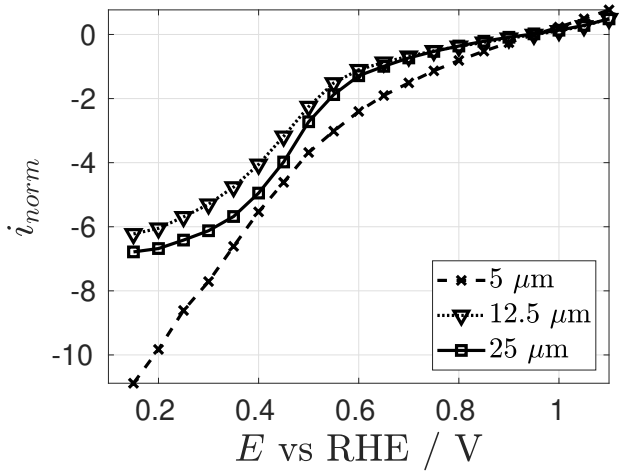

Figure 3.10: Normalised sampled current voltammograms using different sizes of Pt microdisc electrodes at 10 ms. The normalisation was performed by dividing the current transients with the Mahon-Oldham equation assuming $n = 1$. See Figure 3.8 for experimental details.

To observe the presence of the adspecies with these electrodes, shorter sampling times are needed. Figure 3.10 shows the normalised sampled current voltammograms for different sizes of Pt microdisc electrodes sampled at 10 ms. In all cases a high value of n_{app} was obtained, indicating the presence of the adspecies at that time scale. For the bigger electrodes ($a = 12.5$ and 25 μm), the wave is shifted to negative potentials, similar to the true steady state (500 ms), meanwhile, the smaller electrode ($a = 5$ μm) does not follow this trend. The absence of the plateau can be explained by the high rate of mass transport; at this time scale, the reaction is kinetically limited, needing high overpotentials to reach the diffusion controlled state. The higher values of the current at all potentials suggest that the contribution of the adsorbed species to the overall current is higher than that of the ORR, probably due to the low currents of the kinetic limited ORR response with this electrode. This also suggests that by increasing the mass transport regime, it is possible to separate the response of the dissolved and adsorbed species. Experimentally, this may be challenging; higher rates of mass transport require the construction of smaller microelectrodes which can be difficult. Additionally, these electrodes would have a smaller number of active sites available for the adspecies, decreasing their contribution to the current. To circumvent

the latter, a small microelectrode with a high electroactive area can be constructed by depositing Pt nanoparticles. This electrode would provide the active sites for the adspecies while also ensuring that the steady state is reached in a short time. Examples of this electrode are used on the following section to test the presence of the adsorbed species with sampled current voltammetry.

3.2.3 Pt nanoparticles

In this section, two types of nanostructured electrodes were used to test for the presence of the adsorbed oxygen species on transient conditions. The construction and characterisation were presented in Chapter 2. The electrodes used have an appreciable difference on the Pt electroactive area available for the ORR. Their response at the steady state is presented and compared to a bare Pt microdisc, followed by their results on transient conditions with sampled current volammetry.

First a carbon nanoelectrode was constructed from a pulled quartz capillary (a = 140 nm) and a Pt sub-micron sphere was electrochemically deposited on it, with r = 450 nm. Linear sweep voltammograms at different scan rates in aerated 0.1 M $KClO_4$ were recorded and a sigmoidal shape was obtained at scan rates as high as 1 V s^{-1}, this being evidence of the high rate of mass transport achieved. Figure 3.11 shows LSVs at 258 mV s^{-1}, where the sigmoidal shape is visible. Assuming a perfect sphere, at the steady state this electrode has a k_m of 0.51 cm s^{-1}, equivalent to a rotation rate of 2.1x10^6 RPM for a rotating disc electrode[4]. Another indication of the high mass transport coefficient obtained can be observed by comparing the responses of a Pt bare microdisc electrode (a = 5 μm) with that of the spherical electrode, where the latter is more kinetically limited, as evidenced by the more drawn out wave. A carbon fibre microdisc electrode was also constructed (a = 3 μm), and Pt nanoparticles were electrochemically deposited (see Chapter 2 for the construction, Pt deposition and characterisation of the electrode). SEM characterisation revealed the presence of Pt nanoparticles with diameters up to 350 nm. Compared to the spherical electrode, the C/Pt electrode has a high electroactive area given by the nanoparticles, while having

[4] k_m calculated with D = 2.29x10^-5 cm^2 s^{-1} and N = 0.01 cm^2 s^{-1} [1].

a small enough radius ($a = 3$ μm) to ensure that the steady state current is achieved quickly. Figure 3.11 shows a linear sweep voltammogram with this electrode at 2 mV s^{-1} in aerated 0.1 M $KClO_4$, higher scan rates showed high capacitive currents due to the increased electroactive area given by the nanoparticles.

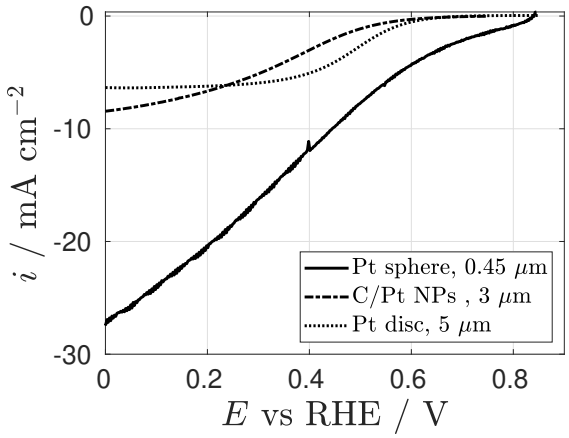

Figure 3.11: a) Linear sweep voltammograms for a Pt sphere electrode ($r = 0.45$ μm, 258 mV s^{-1}), a carbon fibre disc with Pt nanoparticles ($a = 3$ μm, 2 mV s^{-1}) and a Pt disc electrode ($a = 5$ μm, 20 mV s^{-1}) in aerated 0.1 M $KClO_4$. The voltammograms were normalised against the geometrical area.

The normalisation to estimate n_{app} was performed using its respective diffusion controlled equation according to its geometry. Figure 3.12 shows the normalised LSV for the spherical electrode, this revealed a value of $n_{app} = 2$, indicating that all the H_2O_2 produced is leaving the surroundings of the electrode at a high rate before it can be reduced to H_2O. This confirms what was observed by others [4, 5, 75] and in this work (Figure 3.3), regarding the strong dependence of n_{app} on the mass transfer coefficient. Figure 3.12 also shows the normalised LSV of the CF/Pt electrode, revealing the apparent number of electrons at the plateau. Compared to the Pt sphere and the 5 μm Pt disc, this electrode shows a higher value of n_{app}, which is evidence of an almost complete reduction of O_2 towards H_2O (n_{app} approx. 4). A bare Pt electrode of this size would have a smaller value of n_{app} due to the high rate of mass transport. It is believed that the source of this larger value of n_{app} is the effectiveness of the nanoparticles at reducing H_2O_2 due to their close arrangement which prevents it to diffuse before being further reduced to H_2O.

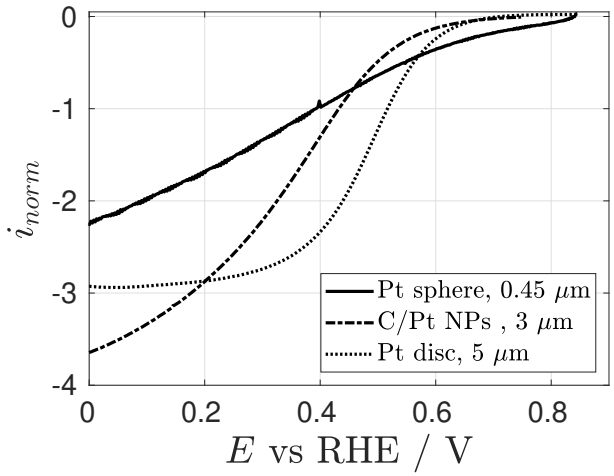

Figure 3.12: a) Linear sweep voltammograms for a Pt sphere electrode (r = 0.45 μm, 258 mV s^{-1}), a carbon fibre disc with Pt nanoparticles (a = 3 μm, 2 mV s^{-1}) and a Pt disc electrode (a = 5 μm, 20 mV s^{-1}) in aerated 0.1 M $KClO_4$. The LSVs for the discs were normalised against the Mahon-Oldham equation while the spherical electrode was normalised against the Cottrell equation for a sphere.

These electrodes were also used in transient conditions to test for the presence of the adsorbed oxygen species. These electrodes were selected due to their extreme conditions: the spherical electrode provides a high rate of mass transport to quickly reach the steady state while having a restricted electroactive area due to the size; the C/Pt electrode also provides a high rate of mass transport while having a high electroactive area due to the Pt nanoparticles. This could simplify the discrimination between the diffusion controlled and the adsorbed species.

First, the Pt submicron sphere electrode was used. From the equation for k_m, Equation 1.5, the steady state response can be reached in only 12 ms (105 % of the true steady state). For a potential sweep experiment, this value would correspond to 2.14 V s^{-1}. This confirms what was observed in Figure 3.11, where a scan rate as hight as 258 mV s^{-1} showed a steady state response. Deviations from the steady state at those timescales would imply the presence of the adsorbed species. Figure 3.13 shows the experimental and theoretical current transient for the reduction of oxygen obtained with this electrode. The theoretical current seems constant at all times, this is due to the high rates of mass transport given by the spherical geometry that ensures that

the steady state is reached in 12 ms. Recalling the equation for k_m, Equation 1.5, the shortest sampling time used in this work (2.5 ms) increases k_m for only around 12 %; to increase it to at least 20 % would require 700 μs and around 110 μs to increase it 50 %. This has an important implication in the value of n_{app} for the reduction of oxygen. As shown in Figure 3.12, at the steady state n_{app} is close to 2, and since the electrode requires the microsecond scale to have an appreciable influence on k_m, on the timescale used here (millisecond) the value of n_{app} can be assumed to be constant. Then, the methodology proposed by Perry and Denuault where they compared an equation to their experiment, can be considered valid when using electrodes with high rates of mass transport, since the value of n_{app} would not change over time.

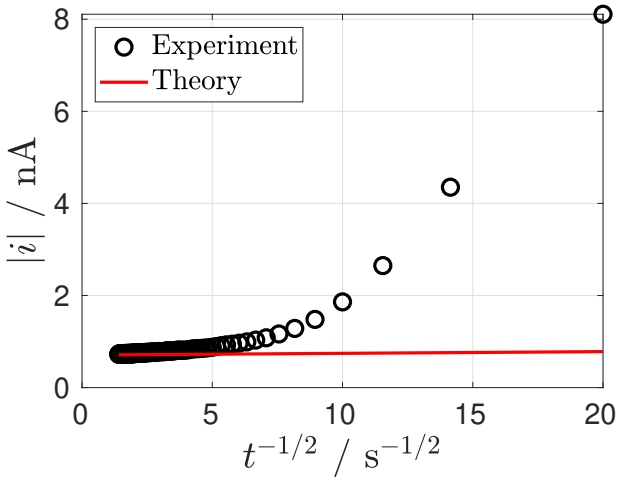

Figure 3.13: Current transient recorded at 0 V vs RHE using a Pt sphere electrode (r = 0.45 μm) in an aerated solution 0.1 M $KClO_4$. The theoretical current transient was obtained from Equation 1.1.

The experimental current from Figure 3.13 shows deviations from the theory at short times that can be related to the reduction of the adsorbed oxygen species. The charge of adsorption of the adspecies was calculated by integrating the difference between the experimental and the theoretical currents. The charge obtained was Q = 131.2 μC cm^{-2}, which is higher than what was reported by Perry and Denuault (33 μC cm^{-2}, [1, 2])[5]. In their case, the assumption of n_{app} being constant could underestimate

[5]The electroactive area of the Pt sphere electrode was estimated from an aerated CV in H_2SO_4, the contribution of the ORR was removed by subtracting the limiting current.

the charge of adsorption, since at short times n_{app} would be smaller, increasing the value of Q. From Equation 1.5, it can be seen that the value of k_m is dictated by the competition between the transient response (proportional to $t^{-1/2}$) and the steady state response (proportional to r^{-1}). With bigger electrodes, the transient term becomes more important at short times, increasing the value of k_m. Then, the current at short times would decrease due to n_{app} being smaller; this effectively would make the charge higher than the one reported by Perry and Denuault. Another possibility for the higher Q obtained could be related to the surface structure of the electrode. Some research groups have reported that Pt nanoparticles tend to adsorb oxygenated species too strongly, mostly in the deffects of the nanoparticles [36, 79, 80]. It is possible that the deposition created a high number of defects that would allow this behaviour. It should also be noted that the charges of adsorption obtained with small Pt disc electrodes (see Figure 3.7) are similar to the charge for the Pt sphere. It may be possible that these electrodes have a high affinity for the adsorbed species due to the presence of defects.

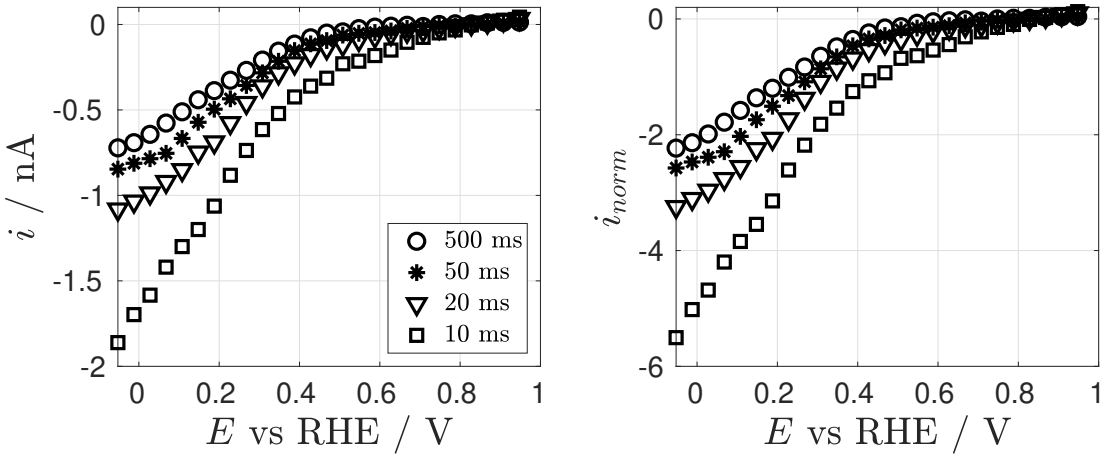

Figure 3.14: Left: sampled current voltammograms for the oxygen reduction reaction and right: normalised SCVs using a sub-micron spherical Pt electrode ($r = 0.45$ μm); the Cottrell equation for a sphere was used for the normalisation.

Sampled current voltammograms were obtained with this electrode and are shown in Figure 3.14. Similar to the results with potential sweeps at the steady state, the SCV sampled at 500 ms is kinetically limited due to the high k_m achieved. The apparent

number of electrons is close to 2, as expected for an electrode of this size. Small variations in the number of electrons due to the presence of the adsorbed species were only appreciable for SCV sampled at times shorter than 200 ms, where n_{app} changed from 2.2 when sampling at 500 ms to 2.3 when sampling at 200 ms. At more positive potentials the normalised SCVs show that the wave is affected by the presence of the adsorbed oxygen species, in agreement with what was reported by Perry and Denuault.

The subtraction of the theoretical controlled current to obtain n_{app} and Q only works when applying a potential step at the ORR plateau. The response at potentials where the current is influenced by electron transfer requires the use of a different equation. Perry and Denuault proposed an equation for quasi-reversible sampled current voltammograms of species in solution with microdisc electrodes [20]. This equation is complex in nature and the extraction of the apparent number of electrons is not a straight forward procedure. Instead, exploiting the mass transport regime to discriminate the diffusion controlled species may be a suitable way of obtaining the charge of adsorption as a function of potential. As was shown previously, the spherical electrode can reach the steady state in about 12 ms, then, it can be assumed that i_{lim} does not vary in the time scale of the experiment. For the following analysis, the limiting currents obtained at all potentials were taken as a baseline and subtracted from their respective current transients. After integration of the subtracted current, a plot of Q against E was constructed, Figure 3.15 shows the results. The plot shows that the charge is higher at the potentials for the ORR plateau; this is expected since it is at this region were the current is more sensitive to the presence of the adsorbed species (see normalised SCVs). These results need to be taken with care; at the plateau, the adsorbed species are completely removed in about 100 ms. Potentials at the plateau would provide a stronger driving force for the reduction of the adspecies than more positive potentials, where longer times may be needed to completely reduce them. A better solution to this problem would be simulating the steady state response of the spherical electrode assuming that n_{app} remains constant. This would require the knowledge of kinetic parameters (α and k_s) of the ORR, nevertheless, as the ORR is a catalytic process, it requires free Pt sites to proceed, that may in fact be occupied by the adsorbed

species, and so the subtraction procedure may still not be completely valid. In both methodologies, (Figure 3.15 and simulations) the charge of adsorption as a function of potential would be an approximation.

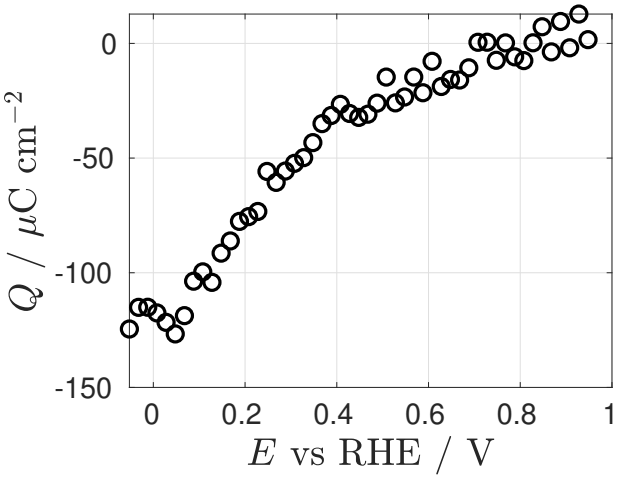

Figure 3.15: Charge of adsorption as a function of potential for a spherical Pt electrode (r = 0.45 μm) in areated 0.1 M $KClO_4$.

Transient experiments were also performed with the C/Pt microelectrode (a = 3 μm). This electrode is small enough to quickly reach the steady state while also having a high availability of free active sites for the adsorbed oxygen species due to the nanoparticles. At the steady state, the calculated k_m was 0.1 cm s^{-1}; in transient conditions, it can reach the steady state in about 200 ms (105 %), this is longer than the time required by the spherical electrode (12 ms) but shorter than the microdisc electrode used by Perry and Denuault (a = 12.5 μm, t = 3.5 s). To have a k_m 50 % higher than that at the steady state, this electrode can achieve it in 2 ms, which is in the timescale of the experiments performed here (t > 2.5 ms); a bigger microelectrode (a = 12.5 μm) would achieve the same k_m in around 30 ms. The assumption of n_{app} being constant at all times is not valid here; instead, the high electroactive area is exploited to obtain the value of Q.

A current transient at the ORR plateau was recorded with this electrode and compared to the Mahon-Oldham response, see Figure 3.16. It can be seen that the theoretical current is almost unchanged compared to the experiment. Considering that the mass transfer coefficient of this electrode changes 50 % in the timescale of the experiment

and that the extra current is two orders of magnitude higher at short times, it can be assumed that the contribution of the ORR to the current is minimal compared to the reduction of the adsorbed species. Variations of n_{app} due to k_m may be negligible.

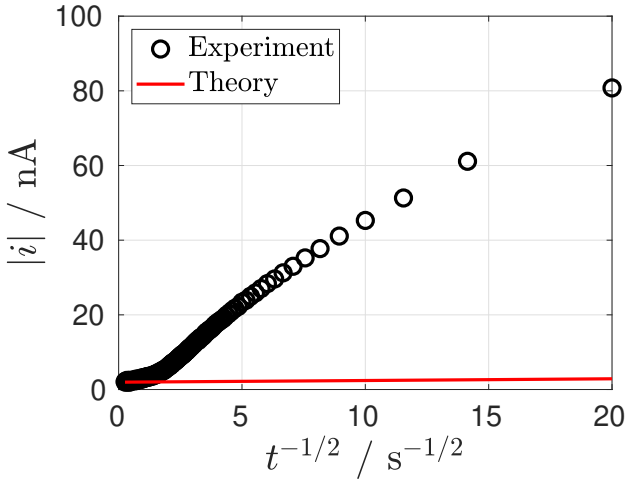

Figure 3.16: Current transient recorded at the ORR plateau using a C/Pt NPs electrode (a = 3 μm) in an aerated solution 0.1 M $KClO_4$. The theoretical current transient was obtained from Equation 1.9.

This electrode provides a high number of active sites with a mass transport coefficient high enough to reach a steady state at short times, ensuring that most of the current comes from the reduction of surface processes. The charge of adsorption obtained was Q = 306.2 μC cm^{-2}, considerably higher than the expected value of 33 μC cm^{-2} and that of the spherical electrode (Q = 131.2 μC). Even though the extra current could be attributed to the reduction of the adsorbed oxygen species, it is possible that capacitive currents are present at short times due to the high electroactive area of the electrode (RF = 19.5). Recalling the equation for a capacitor in transient conditions Equation 1.20, a plot of ln(i) against t should be linear with slope -1/RC and intercept ln(E/R), where R is the solution resistance and C is the capacitance. This plot is shown in Figure 3.17, where it is clear that the current transient does not follow the response of a capacitor. The time required to charge the double layer (defined as $\tau = 3RC$) was calculated to be τ = 21.2 μs [6], three orders of magnitude smaller than the time scale of the experiment (t = 2.5 ms); as a comparison, for a freshly polished Pt microdisc with

[6] τ was calculated with with RF = 19.5, C = 20 μF cm^{-2} and κ = 0.013 Ω^{-1} cm^{-1} [8].

$a = 12.5$ μm and $RF = 3$, the charging time is $\tau = 13.6$ μs. These results suggest that the extra current is due to the presence of the adsorbed species, in agreement with the results obtained with different sizes of Pt electrodes.

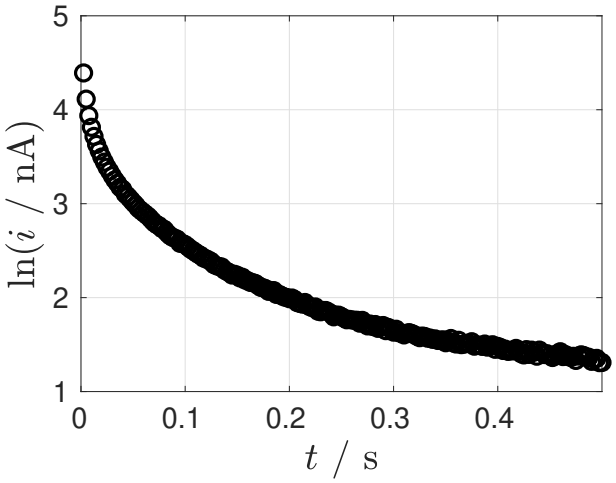

Figure 3.17: ln(i) vs t for a current transient recorded at the ORR plateau using a C/Pt NPs electrode ($a = 3$ μm) in an aerated solution 0.1 M $KClO_4$.

As it was mentioned during the analysis of the spherical electrode, it is also possible that the oxygenated species are preferentially adsorbed on specific sites. It has been reported that nanoparticles have a high density of defects and that they adsorb oxygen species too strongly [79, 80]; this could explain the higher value of Q obtained with this electrode. Another possible explanation could be the presence of different adsorbed species corresponding to carbon functionalities. SEM images of this electrode revealed that its surface is not completely covered by Pt nanoparticles, probably due to the difficulty of nucleating Pt centers in the carbon fibre [69]. Even though the latter may be possible with the C/Pt electrode, it is not expected to be the same with the spherical electrode since Pt seems to completely cover the tip of the quartz pipette (see Figure 2.17); this suggests that the high charge obtained in both cases seems to be related to the number of defects on the nanoparticles.

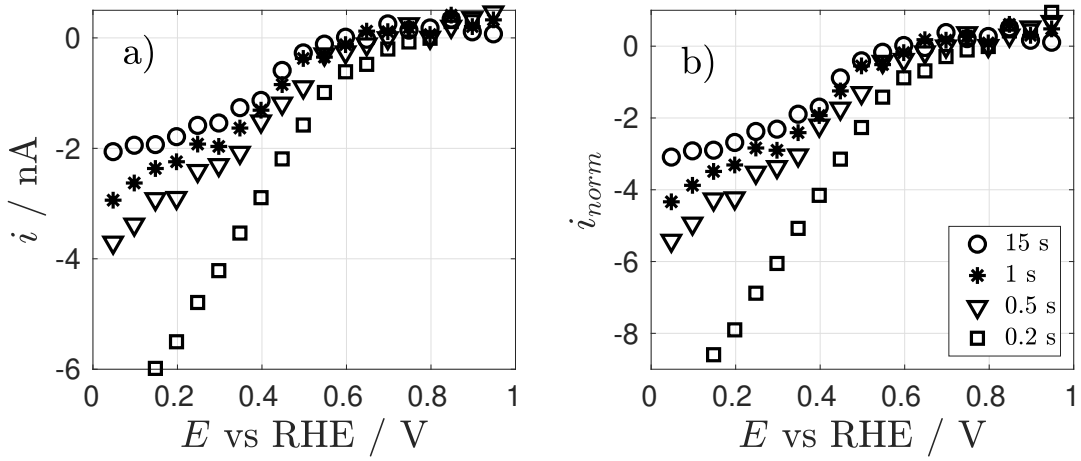

Figure 3.18: Left: sampled current voltammograms and right: normalised SCV using a C/Pt nanoparticles electrode; the Mahon-Oldham equation was used for the normalisation assuming $n = 1$.

Figure 3.18 shows sampled current voltammograms of this electrode. The ORR plateau is only visible at long times ($t > 1$ s) due to the presence of the adsorbed species at shorter times. Since this electrode should achieve the steady state in around 200 ms, the fact that a plateau is observed only after 1 s implies that an extra process is occurring, namely, the reduction of the adsorbed species. In fact, the ORR plateau was only constant when sampling at $t > 10$ s. Figure 3.18 shows a SCV sampled at 15 s, which corresponds to an equivalent 1.7 mV s^{-1}; this is considerably slower than electrodes of bigger diameters. Normalised sampled current voltammograms are shown in Figure 3.18b. The SCV sampled at 15 s shows a value of n_{app} to be approximately 3. The reported value of n_{app} is 2.6 for a Pt microdisc with $a = 5$ μm [75]; this value is smaller than the one obtained for the carbon fibre with Pt nanoparticles, even though the latter has a smaller diameter ($a = 3$ μm). It is believed that the source of this larger value is the effectiveness of the nanoparticles at reducing H_2O_2 due to their close arrangement, which prevents the H_2O_2 to diffuse before being reduced to H_2O. At shorter times, n_{app} increases due to the presence of adsorbed species. With this electrode, the adspecies can be detected even at the second scale due to the greater number of active sites available for them to adsorb and this trend is visible along the whole of the ORR wave.

This section presented results using Pt electrodess with high rates of mass transport and different electroactive areas. It was shown that adsorbed species are present in both cases, with the difference being the time scale where they can be detected (ms for the sphere and up to s for the C/Pt). The high rate of mass transport of the spherical electrode was exploited to discriminate the diffusion controlled species from the experimental current by assuming that in the time scale of the experiment its k_m remained constant, and so n_{app} did not change; with this, i_{lim} was assumed to be constant at all times, subtracted from the experimental current and integrated to obtain Q. Compared to the methodology proposed by Perry and Denuault [1, 2], here, Q is not affected by mass transport. In their case, n_{app} was also assumed to be constant even though the k_m of their electrode changes considerably in the millisecond scale due to its size ($a = 12.5$ μm); it is believed that this underestimates the total charge of adsorption. The use of electrodes with high rates of mass transport makes the assumption of n_{app} valid and allows for a better estimation of the charge density of adsorption.

3.3 Stripping voltammetry

In this section, a methodology to study the reduction of the adsorbed oxygen species is proposed. Perry and Denuault [1, 2] reported the use of chronoamperometry and cyclic voltammetry experiments to study the reduction of oxygen adspecies. The chronoamperometry experiment to obtain the charge of adsorption relies on a mathematical procedure that requires knowing the values of the apparent number of electrons, the concentration and diffusion coefficient of oxygen, and the electroactive area and radius of the electrode beforehand. Also, the procedure to obtain the charge of adsorption by means of the Mahon-Oldham equation assumes that n_{app} is constant at all times and that the process is diffusion controlled. The latter only applies when a potential at the ORR plateau is used but not for the rest of the ORR wave. This is used as an approximation but it was already proven by Pletcher and Sotiropoulos [4] that n_{app} depends on the mass transfer coefficient, which in the case of a microdisc electrode,

k_m depends on both, its diameter and the timescale of the experiment. Since most studies regarding the oxygen reduction reaction are being performed at the steady state [28, 81], the dependency of k_m on t is ignored and hence, the dependence of n_{app} on t has also been ignored. Perry and Denuault also presented a cyclic voltammetry methodology that relies on holding the potential in aerated conditions to allow oxygen to adsorb and degassing while still at rest; a sweep is then performed to reduce these adspecies [2]. A background voltammogram recorded on a degassed solution is then subtracted to reveal a stripping peak. This stripping peak can then be integrated and divided by the electroactive area to obtain the extra charge for the adsorption of oxygen. Perry and Denuault [2] pointed out that this is a time consuming methodology due to the degassing step (up to 30 min depending on the volume of the solution). In this chapter, a methodology to obtain the extra charge due to adsorption in fully aerated conditions is presented, the goal is to reduce the time of the experiment and to eliminate the need of knowing the parameters required by the chronoamperometric method beforehand. This is achieved by modifying the potential waveform and taking advantage of the fact that at short timescales the contribution from the oxygen adsorbed species towards the current is higher than the contribution coming from the diffusion controlled species.

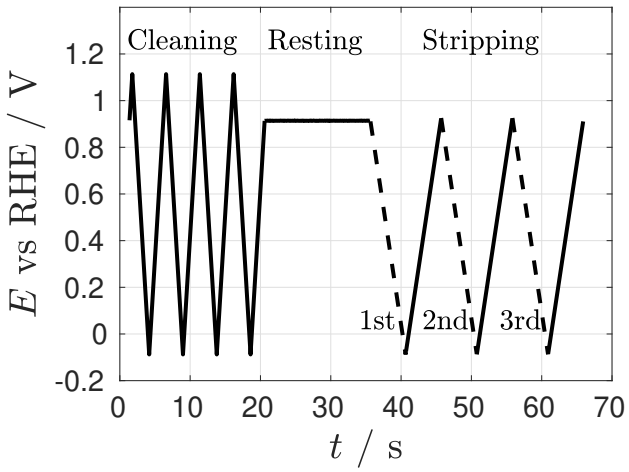

Figure 3.19: Potential waveform applied to obtain a stripping voltammogram. Cleaning: four cycles at 500 mV s^{-1}. Resting: 0.91 V for 15 s. Stripping: three cycles, the scan rate is variable. The dashed lines indicate the stripping sweeps used for the analysis.

Figure 3.19 shows the waveform proposed. It is a modification of the waveform shown in Figure 3.4, where instead of a potential step, several sweeps are recorded after applying the rest potential. As before, the first part of the potential waveform consists on cycling at 500 mV/s to pre-treat the electrode in order to have an oxide-free surface, then, the adsorption of oxygen species is allowed by holding the potential for a set time (15 s). After this, several cycles starting at the rest potential are recorded, taking care not to go more positive than this potential on the next cycles to prevent the formation of oxide. The hypothesis is that due to the rest potential, the first sweep has the information of both, the adsorbed species and the dissolved oxygen species, that is, the current should be the sum of both contributions. Consequently, if the adspecies are completely removed on the first sweep, the following sweeps will only have the information of the dissolved oxygen species and the resulting currents should be similar. By subtracting the first two cathodic sweeps, a peak-shaped voltammogram corresponding to the removal of the oxygen adspecies should be seen. Because of this, it is important to sweep to very negative potentials to ensure that all the oxygen adspecies are removed and also, to not go more positive than the rest potential in order to prevent the formation of oxide. An appropriate scan rate needs to be found to ensure that the adsorbed species can be detected.

Figure 3.20 shows an example of the stripping section of the waveform shown in Figure 3.19, the CV was recorded with a Pt microelectrode (a = 25 μm) at 5 V s^{-1}. The voltammogram is affected by capacitance due to the high scan rate used, although the ORR wave is still visible. The higher current of the first sweep is attributed to the adsorbed species being reduced at the same time as the ORR; subsequent sweeps only contain the current contribution of the ORR.

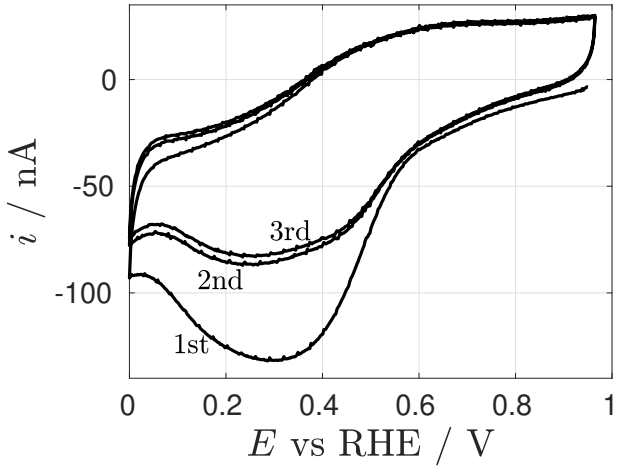

Figure 3.20: Cyclic voltammograms obtained by using the waveform shown in Figure 3.19 using a Pt microelectrode ($a = 25$ μm) in an aerated solution of 0.1 M $KClO_4$ at 25 ^{o}C. The scan rate used was 5 V/s.

It has been reported that in the presence of a species in solution that can adsorb weakly, the peak current of the voltammogram would be higher than that for the case of no adsorption at all due to the reduction of both processes occurring at nearly the same potential [82]. This suggests that the adsorbed species studied here are oxygenated in nature, since their reduction occur at similar potentials; this agrees with what was previously discussed by Perry and Denuault [1, 2]. The methodology proposed here consists on discriminating the ORR current by exploiting subsequent sweeps. After subtracting the second (or third) sweep from the first one, a stripping peak seems to appear (see Figure 3.21), where by integrating this difference and dividing it by the electroactive area of the electrode gave $Q = 26.37$ μC cm^{-2} [7]; this is a promising result since it is close to the reported value of 33 μC cm^{-2} [1, 2]. Compared to the methodology proposed by Perry and Denuault, this method does not require the prior determination of a, C, n or D, greatly simplifying the analysis; the charge of adsorption can be measured directly from experimental data since it does not rely on a specific model for the diffusion controlled species. The stripping method also reported by Perry and Denuault [2], relies on degassing the solution after the oxygen species adsorb on the electrode and then sweeping to reduce them; they reported that this is a time consuming

[7] Average of five repetitions; the standard deviation was less than 1 % that of Q.

way of obtaining the charge of adsorption ($t > 30$ min due to the degassing). Since the experiments proposed here are performed under fully aerated conditions, the total time is greatly reduced ($t < 1$ min depending on the scan rate).

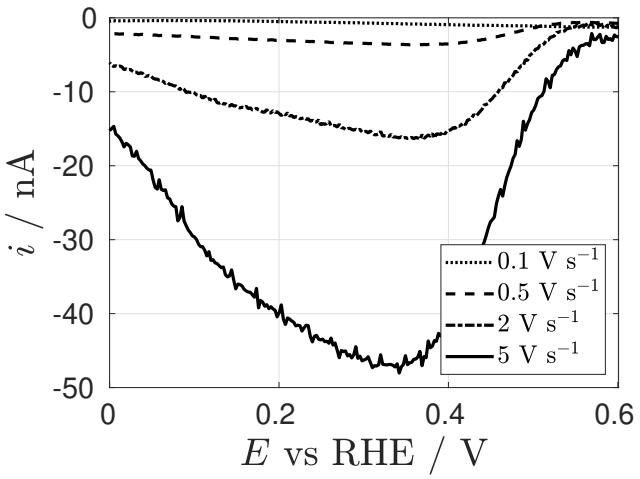

Figure 3.21: Subtracted cyclic voltammograms (first minus third sweep) obtained by using the waveform shown in Figure 3.19 using a 50 μm in diameter Pt disc electrode in an aerated solution of 0.1 M $KClO_4$ at 25 ^{o}C. Each voltammogram is the average of 5 repetitions.

The analysis performed on current transients with Pt microdisc electrodes revealed that the adsorbed species are completely reduced at around 200 ms, this is equivalent to a scan rate of about 130 mV s^{-1}, that is, high scan rates are required to observe the presence of the adsorbed species. In this section, the charge density of adsorption is presented as a function of the scan rate. Figure 3.21 shows subtracted voltammograms for the 50 μm Pt disc electrode at different scan rates. The subtraction reveals a stripping peak where the peak potential seems to shift to the left as the scan rate is increased. This could be due to the kinetics of the adsorption process that dominates the reaction. Since the adsorbed species are detected at short times by CA experiments ($<$ 200 ms), it can be assumed that at high scan rates the reduction of the adsorbed species dominates the current.

Figure 3.22 shows the peak current of the subtracted voltammograms for the 50 μm Pt disc electrode against the scan rate. It can be seen that a linear relation was obtained, thereby confirming an adsorption process. The values for low scan rates have to be taken with care, since the adspecies may not be detected ($<$ 130 mV s^{-1}). To have a

better idea of the scan rate that needs to be used to detect the adspecies, the subtracted voltammograms were integrated to obtain a charge of adsorption, the results are shown in Figure 3.23 for different microdisc electrodes. The potential limits were chosen by eye, where the first and second sweep agreed, presumably because no adsorbed species can be detected at potentials higher than 0.6 V and hydrogen adsorption is present at potentials lower than 0 V.

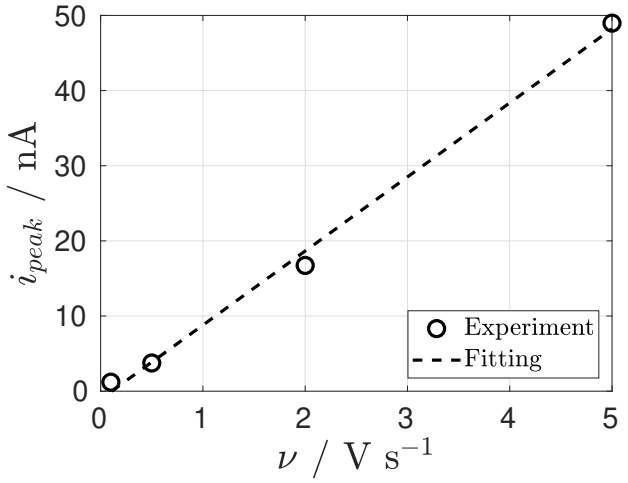

Figure 3.22: Dependency of the peak currents on the scan rate of the subtracted voltammograms obtained from Figure 3.21. A 50 μm diameter Pt disc electrode was used in an aerated solution of 0.1 M $KClO_4$ at 25 ^{o}C. $R^2 = 0.9959$. The reproducibility is within 12 %.

Figure 3.23 shows that for scan rates higher than 2 V/s, the peak currents seem to reach a plateau at around 20 μC cm^{-2}. These results are promising because they suggest that the methodology may work on different geometries and electrodes since it does not rely on a specific model to obtain the extra charge of adsorption. Also, the subtraction procedure removes any contribution from capacitive currents that may be present at high scan rates, opening up the possibility to study adsorbed species with larger electrodes and higher electroactive areas (macroelectrodes, catalyst inks, nanostructured electrodes, etc.).

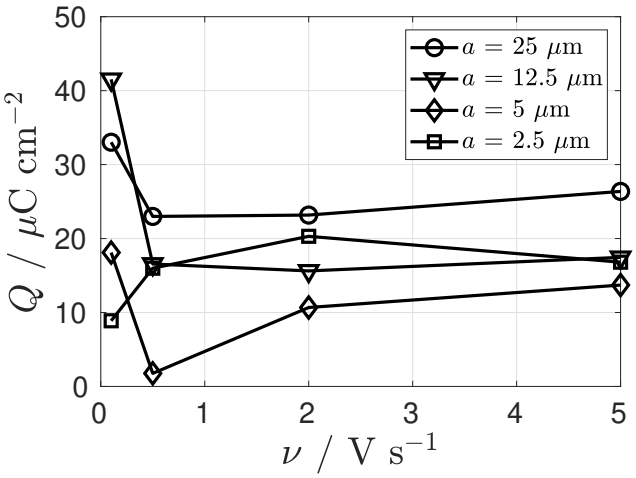

Figure 3.23: Charge density of adsorption as a function of the scan rate and the electrode size. The experimental error was within 10 %. See Figure 3.22 for the experimental conditions.

3.4 Conclusions

In this Chapter, the oxygen reduction reaction was studied with Pt electrodes that provided a high rate of mass transport. Experiments with cyclic voltammetry showed the dependency of the apparent number of electrons on the mass transport coefficient, confirming what was observed by other groups [4, 5, 75]. The presence of adsorbed oxygen species after exposure to molecular oxygen was tested using the methodology proposed by Perry and Denuault that relies on subtracting a theoretical diffusion controlled current transient to the experimental response [1, 2]. The results showed that the adspecies can be detected even in the smallest electrodes, where the number of active sites is reduced due to their electroactive area. Sampled current voltammograms with different microelectrode sizes were shown to be affected by the presence of the adspecies, confirming what Perry and Denuault observed using a Pt microelectrode with intermediate size (a = 12.5 μm). The voltammograms at short sampling times showed a high value of n_{app}, consistent with the reduction of the adsorbed species; the sigmoidal shape of those voltammograms implied that the ORR had an important contribution to the current, even though it was expected that the reduction of the adspecies dominated the response. The methodology proposed by Perry and De-

nuault to obtain a charge of adsorption assumed a constant value of n_{app} during the time scale of the experiment, this assumption is not valid at short times, where k_m is high. Here, mass transport was exploited to discriminate the contribution of the ORR on the current transient. Two electrodes with different electroactive areas and small sizes were constructed. The high rates of mass transport given by the radius allowed for the assumption of n_{app} to be constant. The charge obtained with both electrodes was higher than that obtained by Perry and Denuault and is attributed to the higher number of active sites and the negligible influence of the ORR on the current due to the high rate of mass transport and the constant value of n_{app}.

A different methodology to detect the presence of the adsorbed species was proposed. It relies on sweeping the potential at a high scan rate and subtract the currents. Compared to the chronoamperometric and voltammetric methodologies used by Perry and Denuault, this method does not require the previous knowledge of constants (n_{app}, D, C, a) and does not require degassing the solution, greatly decreasing the experimental time and the analysis. This methodology opens up the possibility of studying the presence of adsorbed species on different types of electrodes where a theoretical current is not available, as well as electrodes with high electroactive areas, where capacitive currents may affect their response.

Overall, in this Chapter, mass transport was successfully exploited to discriminate the current contribution from the reduction of molecular oxygen and to separate the reduction of the adsorbed oxygen species.

Chapter 4

Interaction between adsorbed oxygen species, O_2 and pH

In Chapter 3, the adsorbed oxygen species were studied with different sizes of Pt microelectrodes. The high rate of mass transport given by the spherical microelectrode validated the assumption of having a constant n_{app} in transient conditions. Perry and Denuault observed that in the absence of O_2, the adsorbed oxygen species could not be detected; this led them to conclude that the source of the adspecies was the dissolved oxygen [1, 2]. Since Pt surface processes are pH dependent, it was believed that the adsorbed oxygen species could be influenced by pH. Perry performed preliminary studies at different pH following their methodology; the results suggested that acidic solutions suppressed the presence of the adspecies, while in alkaline conditions they could be detected [3]. In this Chapter, Pt surface processes with solutions of different pH are studied and the results are related to the adsorbed oxygen species. Due to the complications of maintaining a clean environment, the experiments shown here were only performed once; the discussion and conclusions of this chapter are discussed in a qualitative way. Different coverages of oxides are formed and their reduction in the absence and presence of O_2 is discussed. Similarities in the behaviour of Pt oxides in acidic and alkaline conditions with the response of the adsorbed oxygen species in $KClO_4$ are presented. Hinder diffusion is also exploited to study oxide formation in the presence of O_2. The results lead to the conclusion that the source of the adsorbed oxy-

gen species is the local changes of pH that can not be compensated by mass transport and by the low buffer capacity of the solution.

4.1 The oxygen adspecies behave as an oxide

In this section, Pt oxide formation and reduction and the oxygen reduction reaction are studied as a function of oxide coverage and pH. Similarities between the response of Pt oxides in acidic and alkaline solutions to those in neutral unbuffered media are discussed. The potential waveform used is similar to the one presented in Figure 2.18, where the stripping step was changed to sweeps, see Figure 4.1. Briefly, the electrode was cycled at 0.5 V s^{-1} to clean it electrochemically, followed by a rest potential (30 s) that is varied to form different oxide coverages; the stripping sweeps were then performed at 0.5 V s^{-1} when using Ar-saturated solutions and at 0.02 V s^{-1} when using O_2 saturated solutions. The voltammograms are normalised against the electroactive area measured from the hydrogen adsorption region of voltammograms obtained in Ar-saturated H_2SO_4.

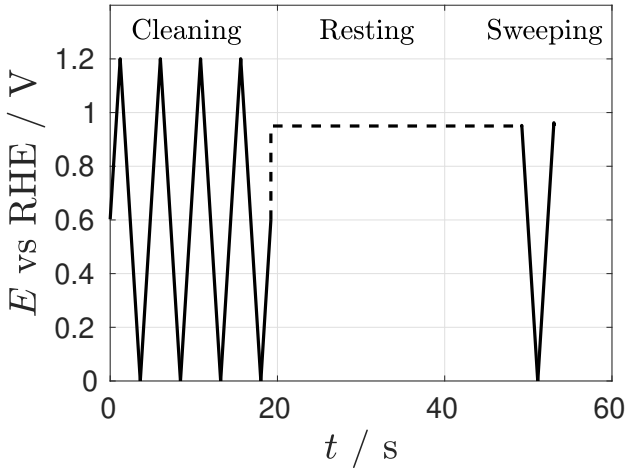

Figure 4.1: Potential waveform used in this section to study Pt surface processes. Cleaning at 0.5 V s^{-1}, resting at different E_r and sweeping at either 0.5 or 0.02 V s^{-1}.

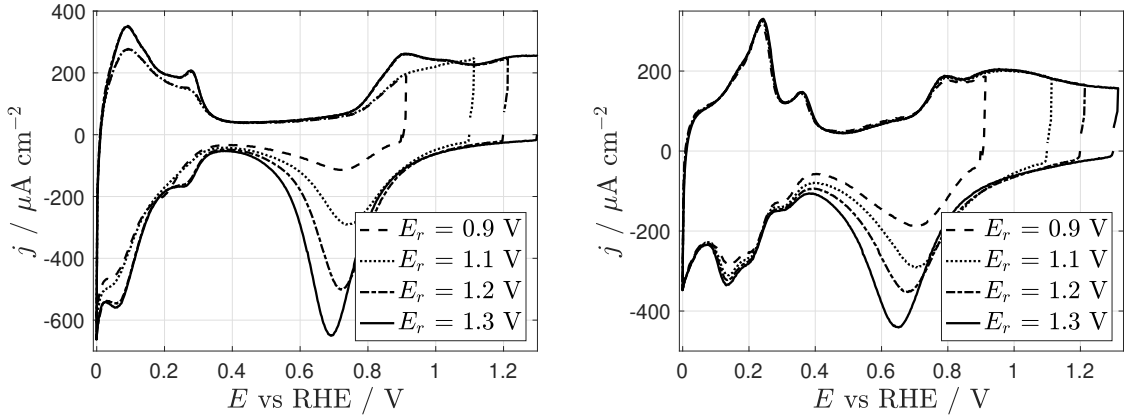

(a) 0.1 M $HClO_4$ **(b)** 0.1 M NaOH

Figure 4.2: Cyclic voltammograms at 0.5 V s^{-1} in Ar-saturated solutions with a Pt microdisc electrode (a = 25 μm). The potential waveform shown in Figure 4.1 was used with different values of E_r. All CVs started at E_r.

4.1.1 Pt oxide in the absence of O_2

This section presents results of Pt oxidation and reduction in the absence of O_2 and with different electrolytes ($HClO_4$, NaOH, $KClO_4$). Different coverages of oxide were obtained by using the waveform shown in Figure 4.1 with different rest potentials. The peak potentials were converted to SHE to reveal their pH dependency and plotted against their respective rest potentials vs RHE. The results are discussed in terms of local changes on pH during the Pt oxidation and reduction processes.

Figure 4.2a shows cyclic voltammograms of a Pt electrode in 0.1 M $HClO_4$ and 0.1 M NaOH, obtained with the waveform shown in Figure 4.1. The oxide reduction region in both electrolytes shows a dependence on E_r, where the peak increases as E_r increases. The integral of the peak current can be related to the oxide coverage formed and will be presented below [37, 39].

In neutral and unbuffered media (0.1 M $KClO_4$, Figure 4.3) the voltammogram is remarkably different. The shifts and separation between peaks seen in the surface processes have been explained in terms of local changes of pH [33, 41, 83, 84, 85]. During Pt oxidation and hydrogen desorption, protons are produced according to:

$$\mathrm{Pt} + \mathrm{H_2O} - 2\mathrm{e}^- \rightarrow \mathrm{PtO} + 2\mathrm{H}^+ \tag{4.1}$$

$$\mathrm{PtH}_{ads} - \mathrm{e}^- \rightarrow \mathrm{Pt} + \mathrm{H}^+ \tag{4.2}$$

while during Pt oxide reduction and hydrogen adsorption, OH^- is generated:

$$\mathrm{PtO} + \mathrm{H_2O} + 2\mathrm{e}^- \rightarrow \mathrm{Pt} + 2\mathrm{OH}^- \tag{4.3}$$

$$\mathrm{Pt} + \mathrm{H_2O} + \mathrm{e}^- \rightarrow \mathrm{PtH}_{ads} + \mathrm{OH}^- \tag{4.4}$$

The reactions given by Equations 4.1 to 4.4 imply that under media with low buffer capacity, the *p*H at the surface of the electrode would be different than that at the bulk during the course of the reactions. Then, the apparent irreversibility seen in Figure 4.3 is due to the anodic processes (Pt oxidation and hydrogen desorption) acidifying the solution, while the cathodic processes (Pt oxide reduction and hydrogen adsorption) make the solution more alkaline; this difference in environment shifts the processes to the potentials dictated by their local *p*H.

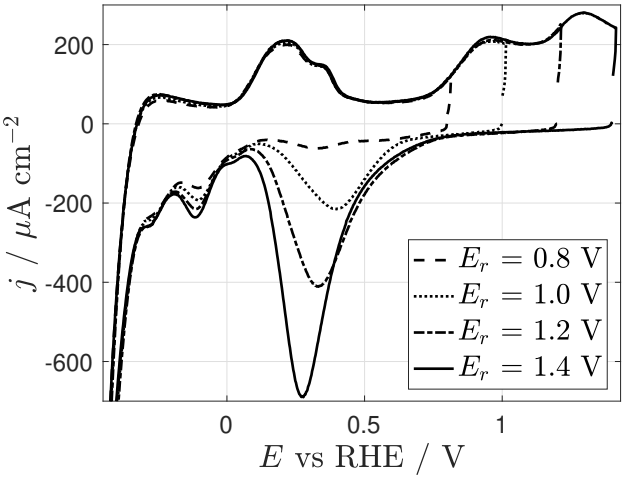

Figure 4.3: Cyclic voltammograms in Ar-saturated 0.1 M $KClO_4$ solution with $\nu = 0.5$ V s^{-1} and a Pt microdisc electrode ($a = 12.5$ μm). The potential waveform shown in Figure 4.1 was used with different values of E_r. All CVs started at E_r.

An important factor to consider is the rate of mass transfer. With a high mass transfer coefficient, the product of the reaction would leave the surface of the electrode rapidly,

minimising the local changes of *p*H given by previous reactions. This has been studied previously with rotating disc electrodes and microelectrodes [33, 84]. It was observed that the potentials for the deposition reactions (oxide formation and hydrogen adsorption) correlated well with their expected *p*H (acidic and alkaline respectively); in contrast, hydrogen desorption was shown to be strongly affected by the mass transport regime. With a stationary electrode, the hydrogen desorption peaks appeared in the potentials expected for alkaline conditions, this is due to the increase in OH^- close to the Pt surface due to oxide reduction and hydrogen adsorption; in contrast, when the mass transport is increased, the hydrogen desorption peaks appear shifted towards potentials expected for acidic conditions; this shift is attributed to the fast removal of the OH^-, leaving only the protons being produced by the desorption process. This discussion leads to the conclusion that in neutral and unbuffered media, changes in local *p*H due to previous processes have to be considered in the following reactions, specially if the timescale of the experiment is not long enough to allow for the recovery of the bulk concentration of H^+ or OH^-.

Oxide coverages were obtained by integrating the reduction peaks and plotted against the rest potential, Figure 4.4. The charges for acidic and alkaline conditions show a linear dependency with rest potential, where at higher E_r the charge tends to 420 μC cm^{-2}, the expected charge for oxide reduction at high potentials [34, 47, 86]. Perry and Denuault observed that the adsorbed oxygen species could not be detected in Ar-saturated $KClO_4$ using a low value of E_r [1], although higher rest potentials were not studied. Figure 4.4 shows that in the absence of O_2, the charge obtained in $KClO_4$ follows the linear response of $HClO_4$ and NaOH that is attributed to oxide growth.

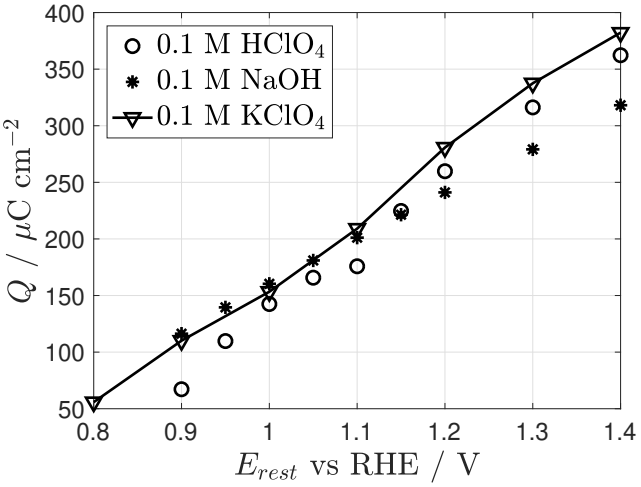

Figure 4.4: Pt oxide reduction charge calculated by integrating the peak currents from Figures 4.2 and 4.3. The potential waveform shown in Figure 4.1 was used with different values of E_{rest}.

To see the effect of local changes of pH in oxide reduction, the peak potentials were converted to the SHE scale and plotted against E_r (vs RHE), Figure 4.5. In acidic and alkaline solutions the peaks are positioned at potentials according to their pH (approximately 0.7 V and 0 V respectively[1]); this is not the case for the results in $KClO_4$, where the peak potentials are closer to the alkaline conditions. For a neutral buffered solution, the peak potentials would be located at intermediate values (ref. [87] shows Pt voltammograms in neutral buffered media.). Due to the low buffer capacity of this solution, the OH^- produced during the reduction of the oxide increases the pH locally, see Equation 4.3. This implies that even when resting at a low potential (E_{rest} = 0.8 V vs RHE), enough OH^- is being produced to make the local pH alkaline, that is, the mass transfer rate given by the microelectrode is not high enough to remove the hydroxide ions being produced during the reduction.

[1] $E_{SHE} = E_{RHE} - 0.059p\text{H}$

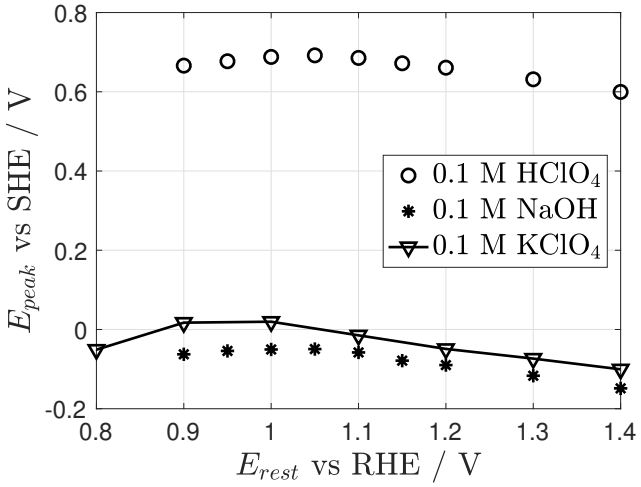

Figure 4.5: Peak potentials (vs SHE) for the reduction of Pt oxides as a function of rest potential (vs RHE). The potential waveform shown in Figure 4.1 was used with different values of E_{rest}.

The results in this section showed that in the absence of O_2, the reduction of Pt oxide in $KClO_4$ is affected by local changes of *p*H. During the reduction, OH^- ions are released, making the surroundings of the electrode more alkaline. Even though the microelectrode provides a high rate of mass transport, the results show that it is not high enough to remove the OH^- being produced. Here, it was shown that even when forming low coverages of oxide, the reduction is affected by local changes of *p*H.

The low oxide formation region (0.8 to 1.2 V vs RHE) was used by Perry and Denuault to show that an oxygenated species was spontaneously adsorbed when a Pt electrode is exposed to dissolved oxygen [1, 2, 3]. In this section, it was shown that in the absence of oxygen, the reduction of Pt oxides formed at low E_{rest} is affected by local changes of *p*H due to the low buffer capability of the solution; this suggests that the adsorbed species may also be affected by it.

4.1.2 Influence of Pt oxide on the ORR

In this section, the impact of Pt oxides on the oxygen reduction reaction is tested in acidic and alkaline solutions and the results are compared to the response in $KClO_4$. Observations are made about local changes of *p*H and its possible relation to the pres-

ence of the adsorbed oxygen species.

Figure 4.6a shows representative anodic sweep waves for the three electrolytes recorded at 0.02 V s^{-1}. Plotting them against SHE reveals their dependence on pH, where the acid and alkaline waves are positioned according to their pH. The voltammogram in $KClO_4$ shows a shift towards alkaline potentials attributed to the local production of OH^-. Here, the production of OH^- comes from the oxygen reduction reaction following the alkaline path [41, 33]:

$$O_2 + 2H_2O + 4e^- \rightarrow 4OH^- \tag{4.5}$$

Similar to the case under Ar-saturated $KClO_4$, the rate of mass transport given by the microelectrode can not compensate for the production of OH^-, thereby increasing the pH in the vicinity of the electrode.

Figures 4.6b to 4.6d show voltammograms in O_2-saturated solutions recorded with the potential waveform shown in Figure 4.1; different rest potentials were used to oxidise the surface in the presence of molecular oxygen. The oxide-free waves show representative anodic sweeps, and only one is shown for each solution as they are not affected by E_r. In contrast, the cathodic sweeps show a dependence on E_r, where the overpotential needed to drive the oxygen reduction reaction is increased as E_r is increased. This difference between the anodic and cathodic waves forms the hysteresis seen in steady state ORR voltammograms that has been studied by several groups and is explained in terms of the state of the surface during the oxygen reduction reaction [48, 37, 36]. In the cathodic sweep the electrode is partially oxidised making the ORR more difficult to proceed, while during the anodic sweep the electrode is presumably free of oxide giving a higher current density than its cathodic counterpart. The position of the cathodic wave is then strongly dependent on oxide coverage.

To better observe the dependence of the position of the wave on E_r, E_k was measured as the potential where 0.1 mA cm^{-2} was obtained. Figure 4.7 shows the plot of E_k against E_r. In agreement with other groups [48, 37, 36], in acid and alkaline conditions E_k becomes more negative as the oxide coverage is increased, and the potential depends on the pH of the solution. In contrast, in $KClO_4$, E_k is shifted negatively towards alkaline

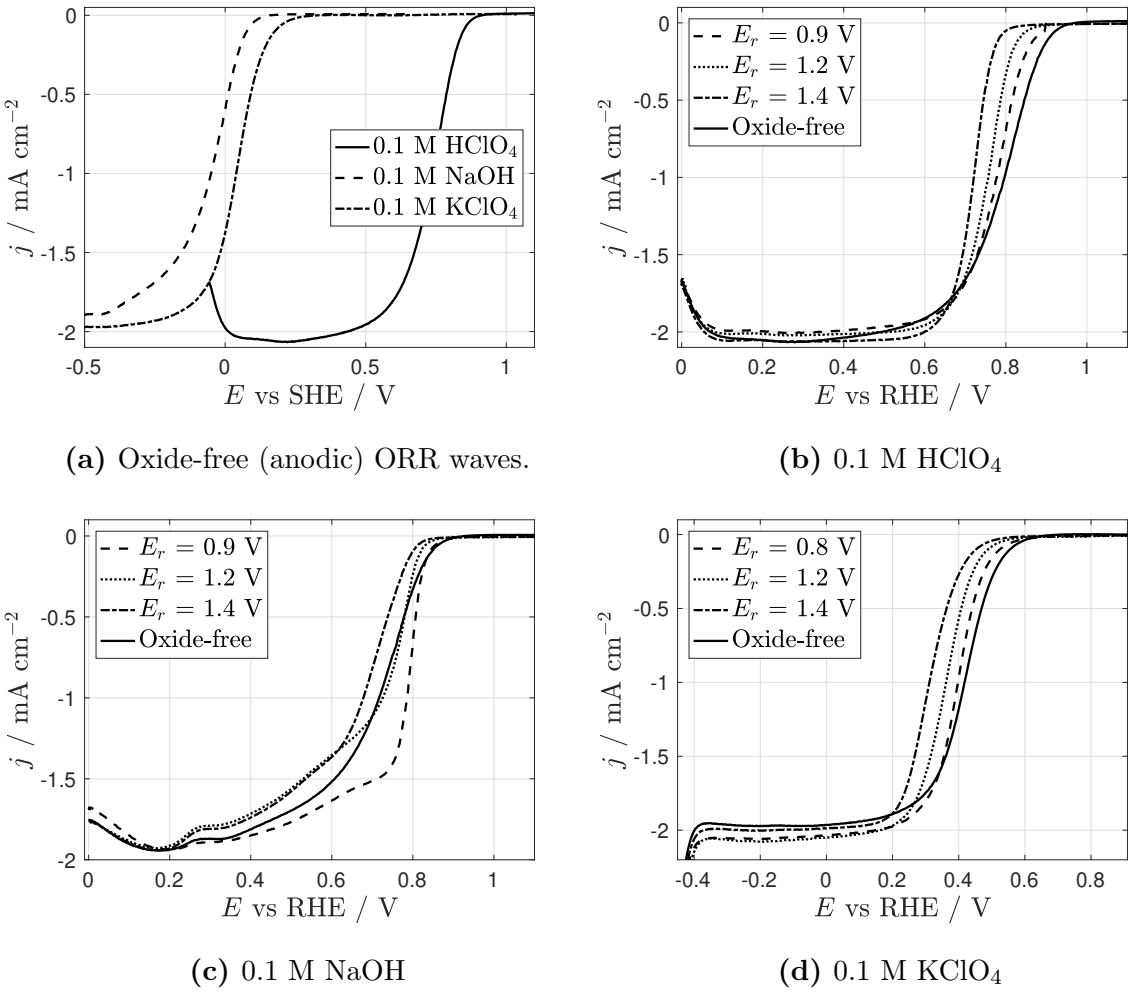

(a) Oxide-free (anodic) ORR waves.

(b) 0.1 M $HClO_4$

(c) 0.1 M NaOH

(d) 0.1 M $KClO_4$

Figure 4.6: a) Representative oxide-free (anodic) ORR waves. b) to d) cyclic voltammograms in O_2-saturated solutions, the potential waveform shown in Figure 4.1 was used with different values of E_{rest}. All CVs were recorded at 0.02V s^{-1} with a Pt microdisc electrode ($a = 12.5$ μm).

potentials, similar to the shift of E_{peak} in Ar-saturated solutions. Since the experimental conditions used here are similar to the ones used by Perry and Denuault, it is believed that the adsorbed oxygen species would show an effect at the low potential regions (E_r from 0.8 to 1.2 V vs RHE); instead, results in $KClO_4$ show a similar trend as in acidic and alkaline solutions: as E_{rest} is increased, a higher overpotential is needed to drive the oxygen reduction reaction. This results, together with the results in the absence of O_2 show that the low oxide formation region is strongly affected by local changes of pH and that the presence of the adsorbed species affects the oxygen reduction reaction in a similar manner as when Pt oxides are formed at higher potentials; this suggest that the adspecies are oxides formed during the rest, probably PtOH due to the low rest potentials used [88]. The adspecies being PtOH would explain the observation made by Perry and Denuault regarding the decrease in charge when anions with increasing ionic strength were used, since PtOH is strongly affected by the presence of spectator species [55, 89].

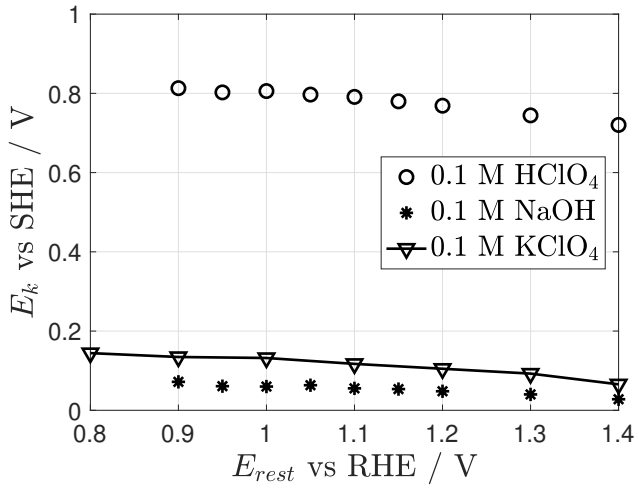

Figure 4.7: Onset potentials for the oxygen reduction reaction obtained at -0.1 mA cm^{-2} from sweeps recorded at 0.02 V s^{-1}, see Figure 4.6.

4.2 The adsorbed oxygen species are related to local changes of *p*H

Perry and Denuault suggested that the adspecies were formed spontaneously due to the presence of molecular oxygen, instead, results from previous sections seem to suggest that their presence is related to local changes of *p*H given by the low buffer capacity of the solution. In this section, some observations related to the influence of *p*H on Pt oxide formation are made.

Figure 4.8 shows cyclic voltammograms in the presence and absence of O_2 in $HClO_4$ and NaOH solutions. In both electrolytes, the ORR response shows the hysteresis due to the presence of the oxide in the forward sweep. The oxide formation region seems unaffected by the presence of molecular oxygen up to the point where the oxygen reduction reaction starts, around 0.9 V vs RHE. This is in agreement with previous work done with flow cells and quartz crystal microbalance [52, 53], and this validates the background subtraction procedure used by researchers when studying the ORR under well defined mass transport regimes [36, 37, 48].

In general, the Pt surface processes do not show any influence from the presence of molecular oxygen. The hydrogen region appears at the same potentials in Ar or O_2 saturated solutions. As mentioned before, Pt surface processes change the *p*H locally, although in the case of extreme *p*H as in Figure 4.8, the buffer capacity of the solutions is high, preventing any shift in potential.

In neutral and unbuffered solutions, the results are remarkably different. Figure 4.9 shows voltammograms in $KClO_4$ in Ar and O_2 saturated solutions that seem to be affected by the presence of O_2. In O_2, the oxide formation region seems to be divided in two regions at around 1.2 V vs RHE; this correlates well with the oxide reduction charge reported by Perry and Denuault, where they observed that the presence of the oxygen adspecies appeared when resting at potentials below 1.2 V, increasing the rest potential resulted in the linear increase in charge ascribed to oxide growth [1]. The latter observation led them to conclude that the oxygenated species were related to the presence of molecular oxygen, here, this is ascribed to local changes of *p*H.

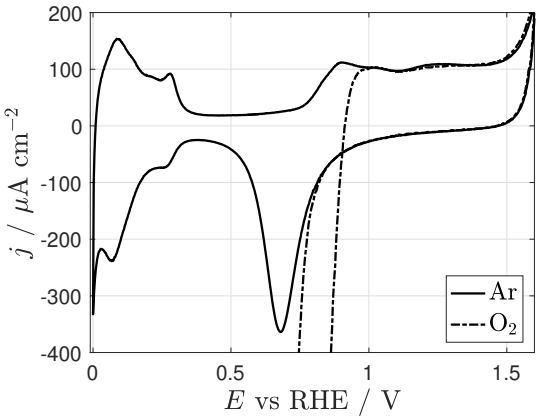

(a) 0.1 M $HClO_4$.

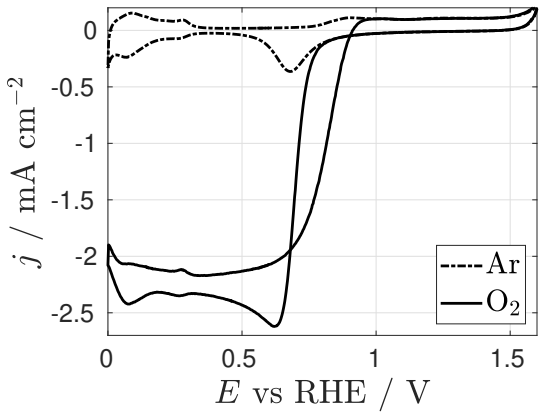

(b) 0.1 M $HClO_4$.

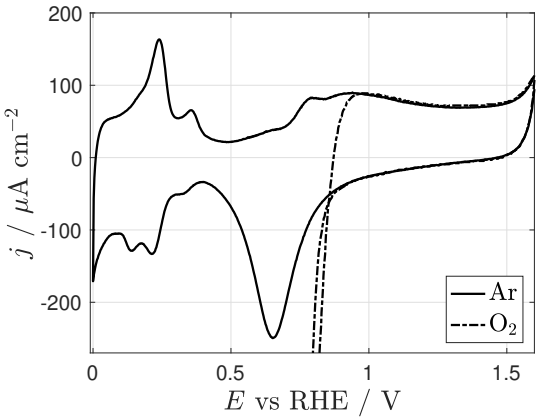

(c) 0.1 M NaOH.

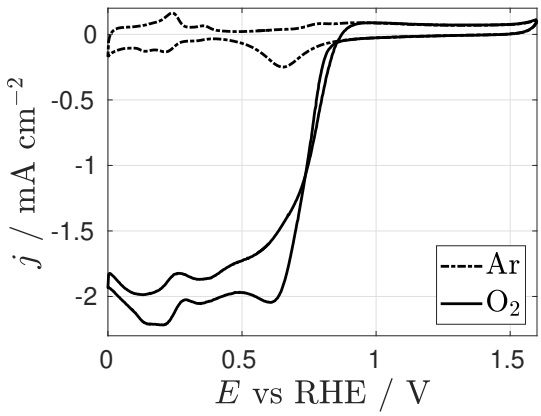

(d) 0.1 M NaOH.

Figure 4.8: Typical cyclic voltammograms in the presence and absence of O_2 recorded with a Pt microdisc electrode ($a = 25$ μm) at 0.2 V s^{-1}.

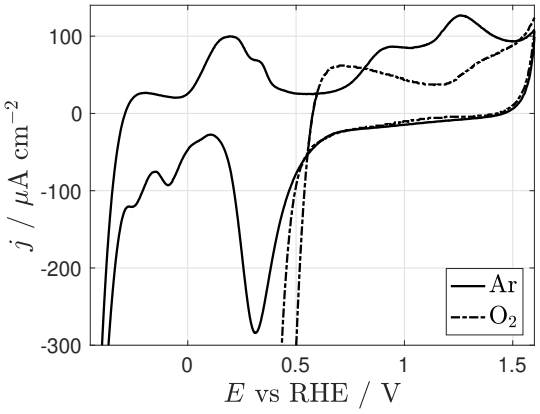

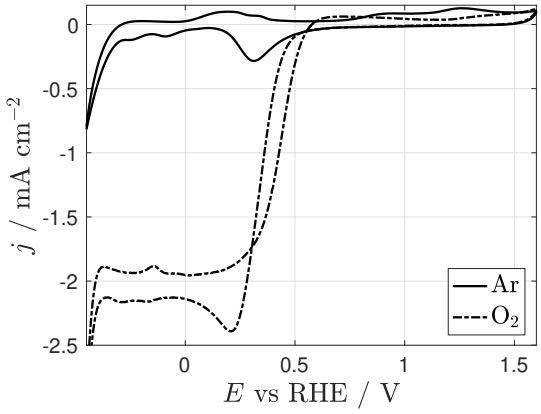

Figure 4.9: Typical cyclic voltammograms in 0.1 M $KClO_4$ recorded with a Pt microdisc electrode ($a = 25$ μm) at 0.2 V s^{-1}.

The voltammograms in the presence of O_2 also show an effect on the hydrogen region; in Ar, the hydrogen adsorption and desorption peaks are shifted away from each other due to local changes of *p*H [84, 83]. In O_2, the peaks appear more reversible, as it is the case when extreme values of *p*H are used (Figure 4.8). Recalling Figure 4.6a, one can see that the ORR in $KClO_4$ appears at potentials close to alkaline conditions due to the high production of OH^-, then, the hydrogen region also appears at alkaline potentials. The fact that the hydrogen desorption peaks are not shifted to acidic potentials, as it is the case for Ar-saturated $KClO_4$, shows that the amount of OH^- produced due to the ORR is high and can not be compensated by mass transport.

Figure 4.10 shows the comparison of the oxide formation region in NaOH and $KClO_4$. The low oxide formation region (0.2 to 0.8 V vs SHE) in O_2 saturated $KClO_4$ has a better similarity with O_2-saturated NaOH than with Ar-saturated $KClO_4$; this can be explained in terms of local changes of *p*H as follows. Starting with the forward current towards negative potentials, the ORR produces a high amount of OH^- that affects the hydrogen region, making it appear more reversible than in Ar-saturated conditions (see Figure 4.9). During the backward sweep, towards positive potentials, the ORR continues producing OH^- although at a slower rate, this then makes the oxide formation region to start at potentials where oxidation starts in alkaline conditions. At around 0.8 V vs SHE, presumably the solution is now acidic either due to the OH^- being completely removed since the ORR is not driven at those potentials, or due to the H^+ being produced during the oxidation that exhaust any OH^- left. It is believed that this change in local *p*H going from alkaline to acidic conditions is the source of the apparent separation of the oxide formation regions at around 0.8 V vs SHE (1.2 V vs RHE), as well as the source of the adsorbed oxygen species reported by Perry and Denuault.

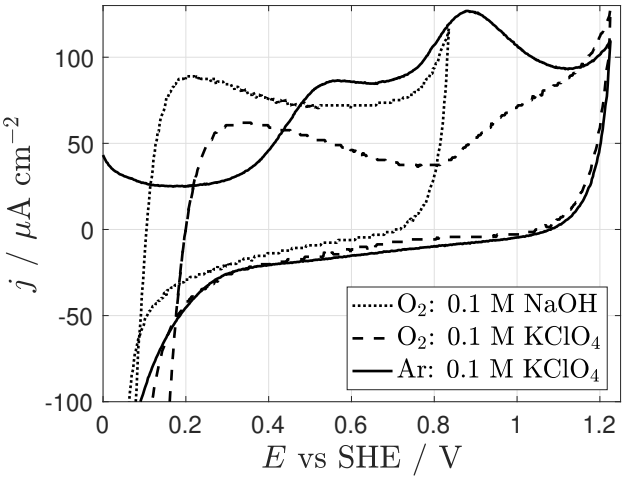

Figure 4.10: Oxide formation region in NaOH and $KClO_4$ solutions recorded with a Pt microdisc electrode ($a = 25$ μm) at 0.2 V s^{-1}.

4.3 SECM to study Pt electrochemistry

The effect of molecular oxygen on Pt oxide formation has been previously studied by the groups of Liu and Kongkanand by using flow cells and quartz crystal microbalance [52, 53]; they formed oxide in the presence of O_2 and stripped it in degassed conditions. The flow cell allowed them to quickly change the solution before the stripping occurred. The complete removal of O_2 implies that the surface conditions during oxide formation and oxide reduction are different. A better approach would be studying both processes in the presence of O_2,[2] nevertheless, the potentials for the ORR and the reduction of Pt oxides are similar, making it difficult to separate both contributions.

In this section, hindered diffusion is exploited to study oxide formation and reduction in the presence of O_2.

4.3.1 O_2 does not influence Pt oxide formation

A Pt microelectrode ($a = 25$ μm, RG = 50) was approached to an insulating substrate to decrease the flux of O_2. The potential waveform used is similar to the one shown in

[2]Perry and Denuault [1, 2] tried this by subtracting a theoretical current transient, although their methodology has certain assumptions that can influence the results, see Chapter 3.

Figure 4.1 and is reproduced here to illustrate the moving procedure, see Figure 4.11. Briefly, the electrochemical cleaning and the first 15 s of the rest were performed away from the substrate at a distance of at least 300 μm; this position is referenced through this section as the bulk. Then, while still at rest, the electrode is moved towards the substrate at a distance of less than 50 μm at 60 μm s^{-1}; this position is referenced in this section as the hindered position. Then, the electrode is kept at rest for 10 s to recover the bulk concentration that was perturbed due to convection. Lastly, the oxide is stripped by sweeping at 0.5 V s^{-1}.

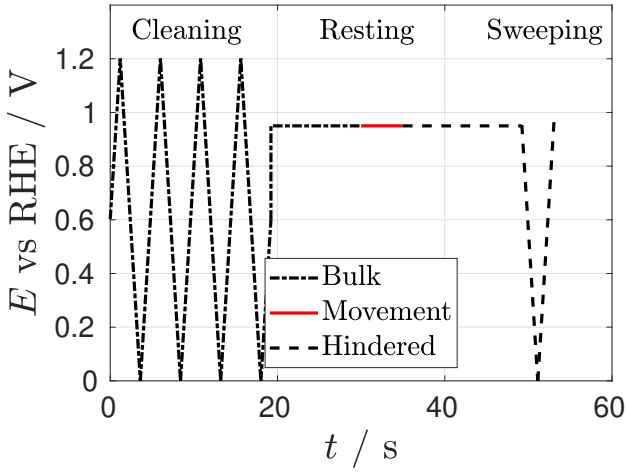

Figure 4.11: Potential waveform used in this section to study Pt surface processes. The cleaning and 15 s of the rest were performed in the bulk position, then, the electrode was approached to the substrate at a speed of 60 μm s^{-1} followed by 10 s of rest and stripping in the hindered position.

In this section, all the experiments were performed in air-saturated solutions due to the open configuration of the SECM cell, see Chapter 2. By following this methodology, hindered diffusion allowed for the study of oxide formation and reduction in the presence of O_2. The combination of parameters used here minimises the ORR contribution to the overall current: hindered diffusion greatly decreases the flux of O_2 [22], the concentration of O_2 is lower when using air-saturated solutions and high scan rates enhance surface processes [8, 82].

First, typical cyclic voltammograms were recorded at the bulk and hindered positions, see Figure 4.12. The hindered CV shows that the flux of O_2 towards the electrode is

minimal, as evidenced by the position of the double layer region. The potentials of the surface processes seem unaffected by the difference in O_2 flux; the oxide region obtained in the bulk follows the hindered response, suggesting that the flux of O_2 does not have an impact on the process.

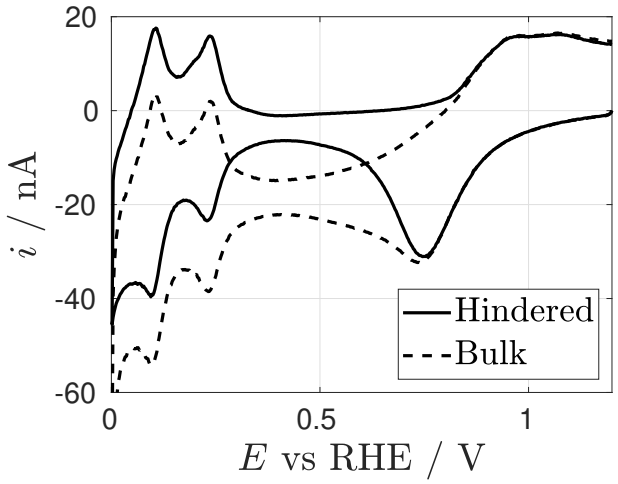

Figure 4.12: Cyclic voltammograms with a Pt microelectrode ($a = 25$ μm) in 0.1 M H_2SO_4 at a scan rate of 0.5 V s^{-1}. The solution was saturated with air.

To further investigate this, different oxide coverages were obtained by applying different rest potentials. Figure 4.13a shows hindered voltammograms; as a comparison, the voltammograms in Ar-saturated H_2SO_4 are shown in Figure 4.13b. The similarities of the hindered voltammograms with those of the Ar-saturated responses indicate that the flux of O_2 was successfully minimised.

Figure 4.14a shows the charges obtained after integrating the oxide reduction peaks. The linear dependency with E_r ascribed to oxide growth can be seen on both cases. The higher charges obtained in the hindered case are a result of the ORR proceeding with a low flux of O_2. The oxide reduction peak potentials were also measured and plotted against E_r, see Figure 4.14b. The difference in peak potentials is only noticeable at low E_r, when the contribution of the ORR to the overall response is comparable to that of the reduction of the oxide. Figure 4.14 shows that Q is more sensitive to small contributions from the ORR than E_{pk} and is expected that decreasing the tip-substrate distance would decrease the influence of O_2 even further.

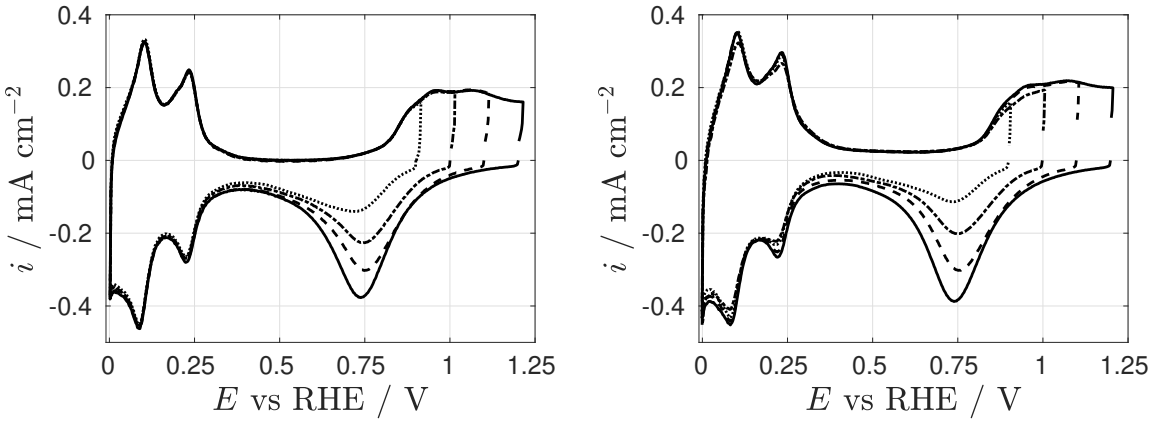

(a) Air-saturated solution, hindered. **(b)** Ar-saturated solution, bulk.

Figure 4.13: Typical cyclic voltammograms in 1 M H_2SO_4 recorded with a Pt microdisc electrode ($a = 25$ μm) at 0.5 V s^{-1} using the waveform shown in Figure 4.11 with different values of E_r.

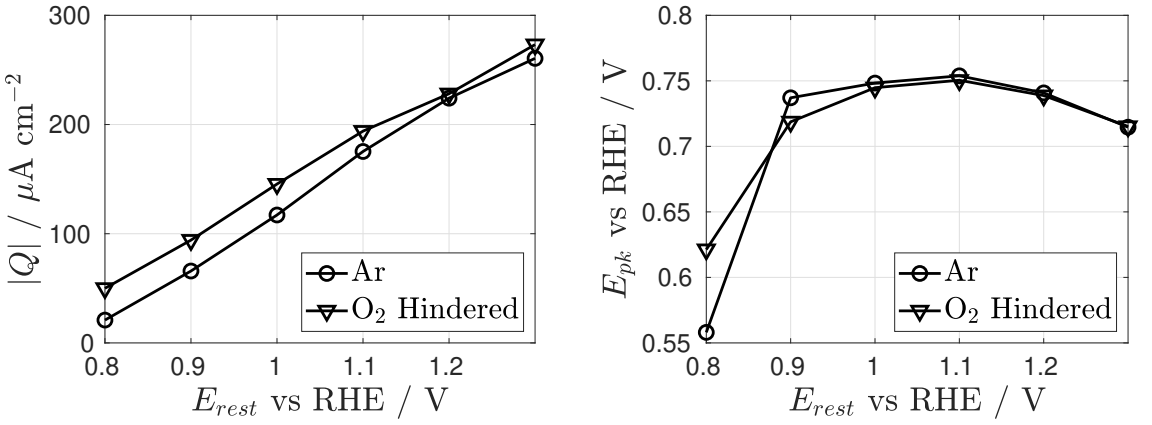

(a) Oxide reduction charges. **(b)** Oxide reduction peak potential.

Figure 4.14: Oxide reduction and peak potentials as a function of E_r. The values were obtained from Figure 4.13.

Overall, Figure 4.14 shows that oxide reduction is not affected by the presence of molecular O_2. This was observed after exploiting hindered diffusion to decrease the flux of O_2 and to study its effect on oxide reduction. Pt oxide was formed away from the substrate and reduced at the hindered position. Compared to previous methodologies that relied on changing the solution between the oxide formation and reduction steps [52, 53], here O_2 was present at all times, ensuring that both steps were performed with the same surface conditions.

The methodology presented here can be extended to cases where the electrochemical response contains the contribution of dissolved and adsorbed species that occur at similar potentials. These cases have been commonly studied by recording cyclic voltammograms at high scan rates to generate a thin diffusion layer and to enhance the current of the adsorbed species [8, 82]. Even though it is possible to use this methodology, voltammograms at high scan rates can be affected by double layer capacitance; instead, exploiting hindered diffusion to minimise the response of the dissolved species may be a better alternative.

4.3.2 Local changes of *p*H affect Pt oxide formation

The previous section showed that the presence of O_2 does not affect the oxide formation region in acidic media; this confirms what was observed by other groups [52, 53] and what it can be seen from voltammograms recorded in the presence and absence of O_2, see Figure 4.8. In neutral and unbuffered media, the voltammograms show remarkable differences depending on the availability of O_2, this led Perry and Denuault to conclude that the adsorbed oxygen species observed were related to the presence of molecular oxygen in solution [1, 2]. To test this, hindered diffusion is exploited in this section to effectively reduce the flux of oxygen and study its influence on the oxide formation region.

Figure 4.15 shows cyclic voltammograms recorded at different tip-substrate distances using an air-saturated $KClO_4$ solution and at 500 mV s^{-1}. The hindered CV shows a decreased current for the ORR due to the lower flux of O_2 achieved. The hydrogen

region and oxide reduction region potentials seem unaffected by the lower O_2 flux, while the oxide formation region shows remarkable differences. In the hindered position, the first oxide formation peak increased in size, while the second peak decreased; this resembles what is observed in alkaline conditions, where in the presence of O_2, oxide formation is shown as a continuous wave, see Figure 4.8.

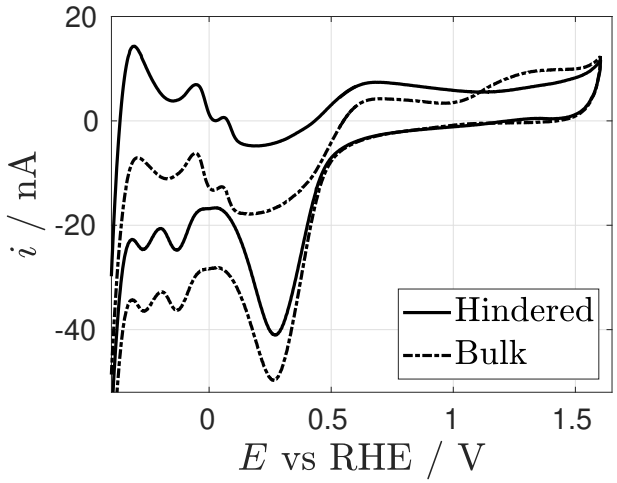

Figure 4.15: Cyclic voltammograms obtained in the hindered and bulk position. An air-saturated 0.1 M $KClO_4$ solution was used with $\nu = 0.5$ V s^{-1} and a Pt microdisc electrode ($a = 25$ μm).

Figure 4.16 shows voltammograms at the same positions recorded at 20 mV s^{-1}. The limiting currents for the ORR show that the O_2 flux was decreased considerably although not completely. The oxide formation region recorded in the bulk shows the behaviour seen regularly under this conditions, where the oxide seems separated in two sections, the first one ascribed to the formation of oxide in alkaline conditions while the second is the formation of oxide in acidic conditions. The hinder voltammogram shows that the first peak increased in current and is now more continuous until a potential around 1.3 V, where a sudden increase in current is observed; in the cathodic sweep, the wave does not return immediately to zero current, as it occurs in the CV recorded in the bulk and in other pH. In fact, the wave has a sigmoidal shape, suggesting the presence of a diffusion controlled current. It is possible that this wave reflects the oxidation of OH^-, as it is known to occur in Pt electrodes at high potentials [90]; here, this would confirm the highly alkaline conditions of the environment. The high RG used

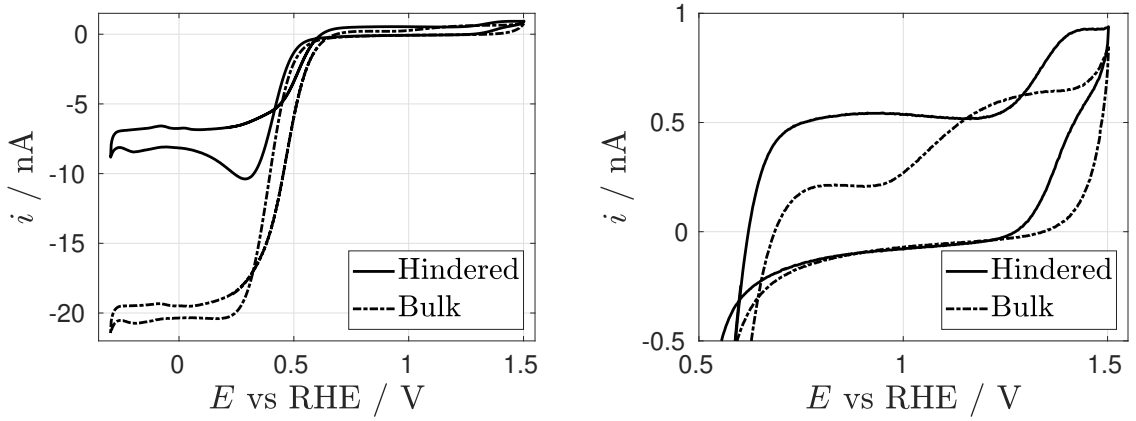

Figure 4.16: Bulk and hindered Pt CVs ($a = 25$ μm) in aerated 0.1 M $KClO_4$. A scan rate of 0.02V s^{-1} was used.

and the short tip-substrate distance simulate a thin layer cell; due to the unbuffered nature of the media, the *p*H of the solution between the tip and the substrate can be easily altered. The experiments performed in 1 M H_2SO_4, see previous section, did not show this behaviour due to the higher buffer capacity of the solution.

If the extra wave seen in the hindered position is related to the diffusion controlled oxidation of OH^-, then it should be possible to control its magnitude by varying the local *p*H. An increase in production of OH^- due to the ORR should increase the limiting current observed, while the production of H^+ should decrease it. Also, due to confinement in the hindered position, the process should be sensitive to tip-substrate distance due to the effect of mass transport. To test this, the potential waveform shown in Figure 4.17 was used. First, the potential was swept at 20 mV s^{-1} from 0.9 V to 0 V, these potentials were selected to minimise oxide formation and prevent hydrogen adsorption respectively, then the potential was held at 0 V for a certain amount of time. Due to he reduction of oxygen, the sweep and the potential step would generate OH^- and controlling the time of the step t_s would control the amount of OH^- produced. The third section consists on sweeping towards positive potentials at 20 mV s^{-1} and at around 1.3 V the wave for OH^- oxidation should appear; the potential is then swept back to 0 V to finish the cycle. Figure 4.17 shows the potentials where OH^- is being produced as solid lines, while the potentials at which it is expected to be detected are shown in dashed lines. Due to the presence of O_2, OH^- is produced continuously,

provided the reduction of molecular oxygen is occurring. It is important to note that, here, a pre-conditioning waveform was not used to prevent an increased change of local pH.

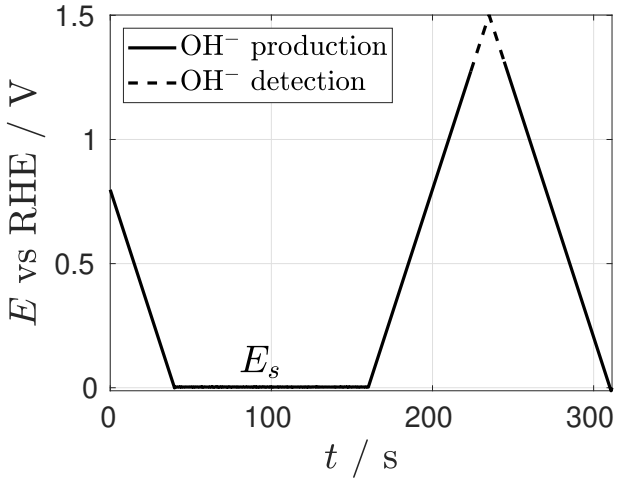

Figure 4.17: Potential waveform used to detect OH^-. The sweeps were performed at 0.02V s^{-1}.

Figure 4.18 shows voltammograms of the oxide formation region obtained with the waveform shown in Figure 4.17. The step time was varied to control the amount of OH^- produced. As it can be seen, the limiting current of the extra wave seen at high potentials increases as t_s increases. From 120 s to 300 s the limiting current does not change significantly, suggesting that the concentration of OH^- reached a maximum.

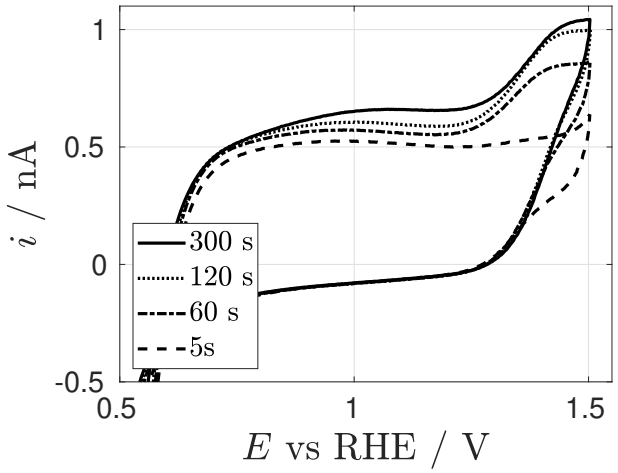

Figure 4.18: Voltammograms of the oxide formation region obtained with the waveform shown in Figure 4.17. The time of the step was varied. A Pt microdisc electrode (a = 25 μm) in a 0.1 M air-saturated solution was used.

It would be tempting to calculate the concentration from the limiting current, however, complications arise due to hindered diffusion. To use the equation for hindered diffusion, it is necessary to know the limiting current for OH^- oxidation at the bulk; this is not possible since the wave only appears under confinement of OH^-; instead, the charge during the production of OH^- was obtained by integration, this includes the negative sweep to reduce oxygen, the holding of the potential at 0 V and the positive sweep from 0 V to 0.6 V, where the ORR is still driven. After integration, the number of moles produced were calculated from the Faraday's law:

$$mol = \frac{q}{nF} \tag{4.6}$$

and by assuming that the reduction of 1 mol of O_2 produces 4 mol of OH^-, as it is the case for the alkaline path, Equation 1.27. In order to calculate the concentration of OH^-, the volume of the thin layer cell needs to be known; here it was assumed to have a cylindrical geometry, with the radius given by the RG (r = RG*a) and the height given by the tip-substrate distance (assumed $h = a$), with this, the estimated volume was 120 nL. The pH was then estimated with:

$$p\mathrm{H} = 14 - \log_{10}(1/[\mathrm{OH}^-]) \tag{4.7}$$

Figure 4.19 shows a plot of the limiting currents for OH^- oxidation obtained from

Figure 4.18 against the calculated pH; the solid line shows the linear regression for the first three data points. The lower limiting current for the higher pH could be due to OH^- leakage, this could be improved with higher values of RG and by ensuring that the tip and substrate are as parallel as possible from each other.

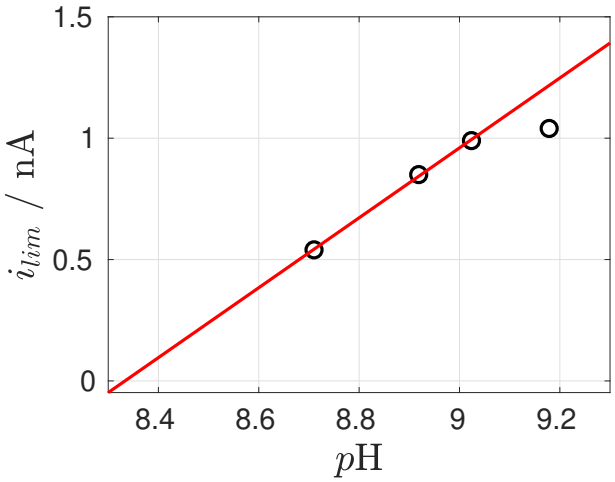

Figure 4.19: Limiting current of the oxidation of OH^- against pH. Currents obtained from Figure 4.18.

Figure 4.19 can also be thought of as a calibration curve for an amperommetric pH sensor; varying the amount of OH^- produced, would change the value of the limiting current, as reported previously [90]. Although in here, the pH was calculated by making certain assumptions, it is shown that the Pt electrode is sensitive to small local changes in pH under hindered and unbuffered conditions.

To continue testing for the pH sensitivity of the oxide formation region, the upper potential of the OH^- detection section was increased to reach the oxygen evolution reaction, known to produce H^+ in neutral conditions and H_2O in alkaline conditions; in both cases, OH^- are consumed by either neutralisation or by producing H_2O respectively. Figure 4.20 shows the results, as expected the oxide formation region is affected by the upper potential. In all cases, the anodic sweep shows that the limiting current ascribed to OH^- oxidation is unaffected, on the contrary, after O_2 evolution, the current of the cathodic sweep decreases with increasing E_{up}, confirming that the current is sensitive to local changes of pH.

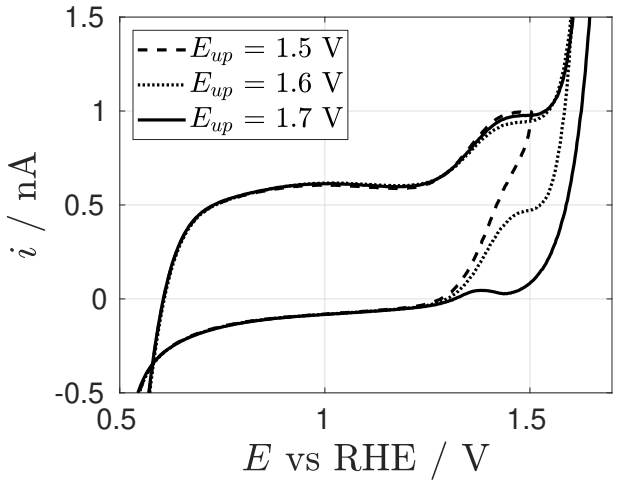

Figure 4.20: Oxide formation region obtained with the waveform shown in Figure 4.17. The upper potential of the OH^- detection section was varied. A Pt microdisc electrode (a = 25 μm) in a 0.1 M air-saturated solution was used.

As mentioned previously, since the oxide formation region is sensitive to pH, it should also be sensitive to tip-substrate distance, as a higher L would allow OH^- to diffuse away, lowering the concentration. Figure 4.21 shows an approach curve recorded at 2 μm s^{-1} as well as anodic LSVs recorded at 20 mV s^{-1}. As expected, the limiting current for ORR is sensitive to tip-substrate distance. Figure 4.21 shows that to have an appreciable effect on i_{lim}, $L < 5$ are required.

Figure 4.22 shows the oxide formation region obtained with the waveform shown in Figure 4.17 and with t_s = 30 s; this time was selected to ensure that small quantities of OH^- were produced. The voltammograms show that the first oxide formation peak increases when decreasing L, due to the higher alkaline conditions that can be achieved in smaller volumes of unbuffered solutions. This is confirmed by the decrease of the second peak, ascribed to oxide formation in acidic conditions; this decrease is due to the OH^- consuming any H^+ produced during the oxidation itself. The H^+ consumption is also evidenced by the union of both oxide formation regions at lower distances until the OH^- oxidation wave appears.

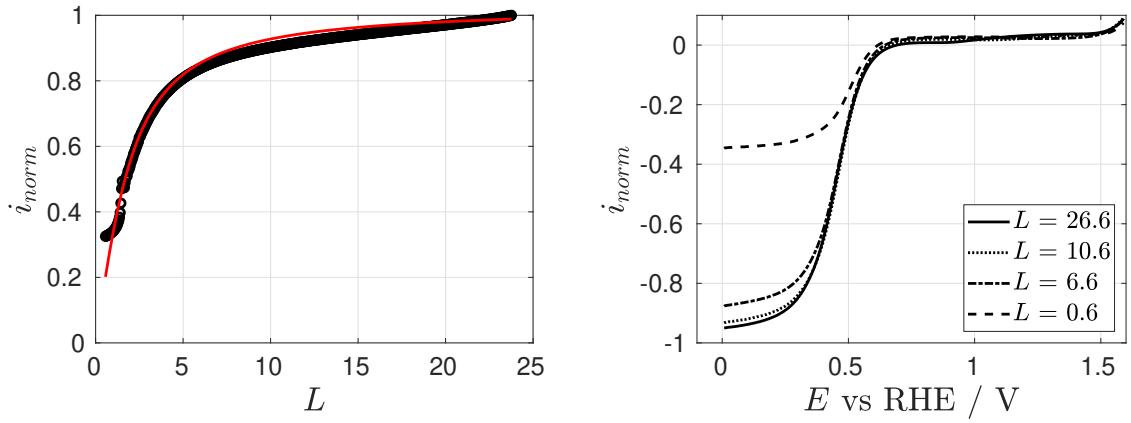

Figure 4.21: Approach curve and LSVs recorded in aerated 0.1 M $KClO_4$.The solid line in the approach curve shows the fitting to Equation 1.19 The LSVs were recorded at 0.02V s^{-1}.

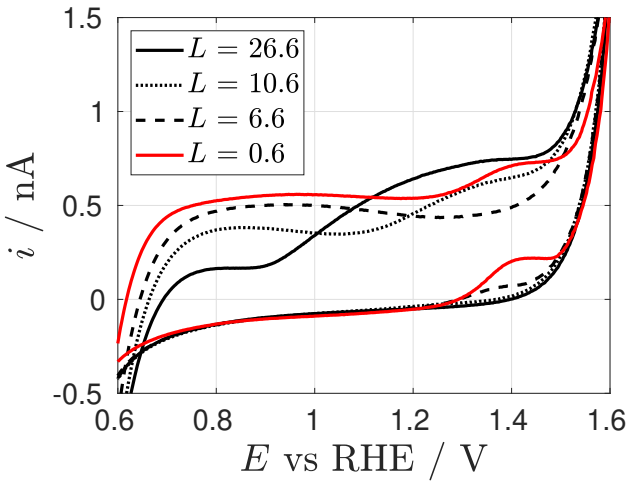

Figure 4.22: Oxide formation region obtained using the waveform from Figure 4.17 with t_s = 30 s and at different tip-substrate distances.

Overall, this section shows that the production of OH^- during the ORR affects the formation of Pt oxide. Confinement with hindered diffusion revealed a diffusion controlled reaction ascribed to OH^- oxidation.

4.4 Final remarks

This Chapter presented evidence that in neutral and unbuffered media, the oxidation of Pt is influenced by local changes of pH. During the reduction of O_2, the surface processes are strongly affected by the production of OH^-, this moves the oxide formation region to more negative potentials that correspond to oxide formation in alkaline conditions. It was suggested that these oxides are the same adsorbed oxygen species observed by Perry and Denuault. They reported a potential window that allowed for the adsorption of the adspecies; this region corresponds to the oxide formation region affected by the production of OH^- during the ORR. One fact to consider is that the ORR is not driven during the E_r; this implies that any OH^- present had to be formed before the rest. Recalling the potential waveform, the cleaning section is performed at potentials where the ORR is driven, and it occurs immediately before the rest, being this the source of OH^-. Overall, this chapter presents evidence that the adsorbed oxygen species observed by Perry and Denuault are oxides formed when the surroundings of the electrode have a higher pH than the bulk solution.

Chapter 5

Sampled current voltammetry

Sampled current voltammetry is an old technique that relies on recording current transients obtained from a range of step potentials; the current is then sampled at a certain time and plotted as a function of potential to construct a voltammogram. Perry and Denuault proposed the use of sampled current voltammetry with microelectrodes (MSCV) to study the reduction of model redox species and adsorbed oxygen species on transient conditions [1, 20]. The use of microelectrodes allowed them to discriminate non-Faradaic currents at short times and to access higher rates of mass transport. In Chapter 4, it was shown that the oxygenated species observed by Perry and Denuault are in fact oxides formed during the rest potential. It is then necessary to study the reduction of oxides in transient conditions to relate the results with those of Perry and Denuault. Sampled current voltammetry of surface processes seems to be non-existent in the literature, although some early experiments with polarography can be found [8]. This Chapter presents SCVs of platinum surface processes and the ORR at different *p*H; an equivalent Koutecky-Levich methodology is proposed to analyse the SCVs. It is believed that under certain considerations and assumptions presented here, it is possible to use sampled current voltammetry (or MSCV) as a substitute to RDE when high rates of mass transport are required. Finally, the theory of sampled current voltammetry of an adsorbed species is presented with emphasis on the analysis to obtain kinetic information.

Figure 5.1 shows the potential waveform used throughout this chapter. The waveform is similar to the one used by Perry and Denuault to study the presence of adsorbed oxygen species [1, 20]. Here, the coverage of the oxides was changed by varying the value of the rest potential.

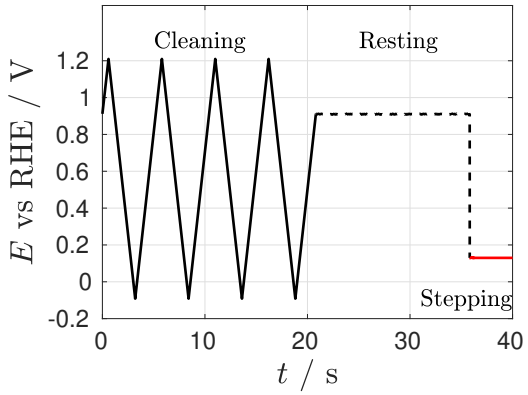

Figure 5.1: Potential waveform used throughout this chapter.

5.1 Reduction of platinum oxides

This section presents sampled current voltammograms of the reduction of platinum oxides in different electrolytes. First, experiments in acidic conditions are used to describe the general behaviour of the SCVs, then, SCVs obtained after resting at different potentials are presented and their shapes related to the oxide coverage. Finally, the general response of SCVs in different electrolytes is discussed.

Figure 5.2 shows sampled current voltammograms recorded in Ar-saturated 0.1 M $HClO_4$ solution using the waveform shown in Figure 5.1 with E_r = 1.2 V vs RHE. The first observation that can be made is that the SCVs are peak-shaped, contrary to the sigmoidal response of reactions with species in solution [1, 8, 20], although similar to what is observed with sweep voltammetry of adsorbed species [91]. For the latter, the position of the peak reveals the potential at which the coverage is half of the initial coverage [6]; as the potential is gradually decreased [1], the coverage also decreases and so each point along the voltammogram is affected by what happened at

[1]For the case of a reduction.

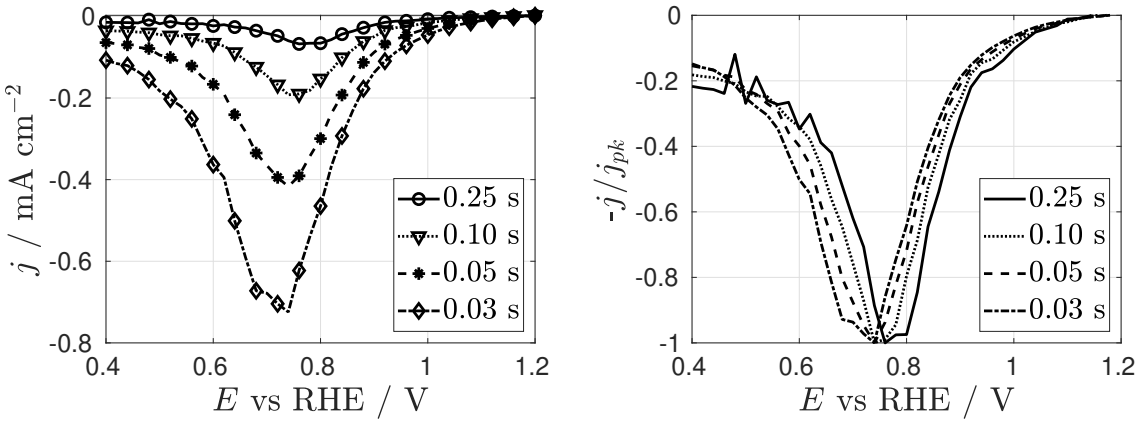

Figure 5.2: SCVs and normalised SCVs recorded in Ar-saturated 0.1 M $HClO_4$ solution using the waveform shown in Figure 5.1 with E_r = 1.2 V vs RHE. The legends show the sampling times. All SCVs started at E_r.

previous potentials. Since the rate of the reaction is dependent on potential, a higher overpotential makes the reaction proceed faster. For SCVs, a different interpretation has to be made due to the difference in methodology (steps as opposed to sweeps). For each potential step, the initial coverage is presumably the same, and as time proceeds, it decreases at a fixed rate. This implies that points along the potential axis are independent from each other, as they are recorded independently, then, the peak potential observed does not reflect the potential for half of the coverage left, as the coverage only depends on the sampling time; instead it is believed that the shape is related to the rate constant k [2]. In Section 5.3, a mathematical explanation is attempted to understand the shape of the SCVs by assuming a simple model. Figure 5.2 also shows sampled current voltammograms normalised by the peak currents [3]. The normalisation reveals a shift towards more negative potentials as time is decreased, this is similar to what is observed when using a range of scan rates on sweep voltammetry for species in solution [8, 20] and adsorbed species [91]; this effect will be addressed in Section 5.3.

Figure 5.3a shows SCVs sampled at 100 ms using different E_r. The currents increase with E_r, and the shapes change accordingly, similar to what is observed with sweep

[2]Rate constant k, not to be confused with the standard rate constant k_s.

[3]The markers were removed to facilitate visualisation.

voltammetry. It could be tempting to integrate the SCVs to obtain the coverage of the oxide; nevertheless, this is not possible due to the different integration domain (time as opposed to potential), the difference between potential steps being to big [4], the need to calculate an equivalent scan rate, and the fact that each point along the potential axis is independent of the others. If instead, the integration is performed in the direction of the current transients, the charge obtained would only reflect the charge recorded since the instrument started measuring[5], and not the total charge from $t = 0$. Due to this limitations, it is not advised to use SCVs to measure the coverage of adsorbed species, instead, sweep voltammetry should be used.

Figure 5.3b shows SCVs sampled at 100 ms and with $E_r = 1.2$ V vs RHE obtained in different electrolytes[6]. The SCV recorded in $KClO_4$ shows an increased current when compared to the SCVs obtained in extreme pH, this support the idea introduced in Chapter 4 where it was shown that experiments performed in neutral and unbuffered media are affected by local changes of pH. Here, due to the nature of the experiment (steps as opposed to sweeps), it should be noted that the change in pH occurs in the direction of the current transients, and so the local conditions in the SCV are different than those of an equivalent experiment with sweep voltammetry. The SCV in $KClO_4$ also shows a higher coverage of oxide compared to the results in NaOH and $HClO_4$[7]. Since the RHE is physically located in the bulk, it can not sense the local increase of pH occurring close to the working electrode; then, relative to the RHE, the oxide formation occurs at potentials more negative than its bulk pH. A rest potential of 0.9 V in neutral pH would then be equivalent to a higher potential in alkaline pH, effectively increasing the coverage of oxide.

This section presented sampled current voltammograms of the reduction of Pt oxides. Due to the difference in experiments, it is not advised to analyse the results in the same way as with sweep voltammetry, and it is suggested that the information be used in qualitative form instead. As shown elsewhere [8, 20], SCV for the reaction of species in

[4] $\Delta E_s = 20$ mV.

[5] The time step was 2.5 ms.

[6] The voltammograms are plotted against SHE to observe the pH dependence.

[7] Recorded at the same conditions in time (100 ms) and E_r (1.2 V vs RHE).

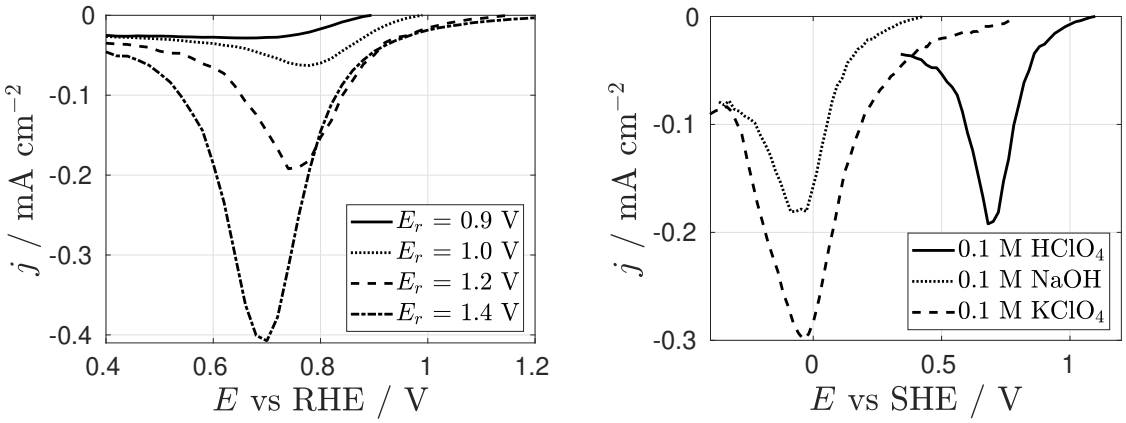

(a) 0.1 M $HClO_4$. **(b)** E_r = 1.2 V vs RHE.

Figure 5.3: SCVs sampled at 100 ms and recorded in Ar-saturated solutions. All SCVs started at E_r.

solution always show a sigmoidal wave due to the diffusion layer thickness being fixed at each sampling time, meanwhile, the results shown in this chapter seem to indicate that SCV for adsorbed species are peak-shaped; this suggests that sampled current voltammetry can be used to differentiate between reactions of species in solution and those of species adsorbed on the electrode. It can be argued that a similar effect is possible when using microelectrodes: under diffusion controlled conditions, the voltammogram is sigmoidal in shape, while surface processes are peaked in nature. Although this is true, both processes have different time scales (long and short times respectively); using low scan rates to achieve steady state and the fact that microelectrodes have a reduced electroactive area, could make the contribution of the surface processes virtually non-existent. Similarly, increasing the scan rate to enhance the response of the adsorbed species would produce a non-steady state voltammogram. This observations lead to conclude that sampled current voltammetry can be used to differentiate reactions with species in solution from those adsorbed on the electrode.

5.2 Oxygen reduction reaction

In the previous section, sampled current voltammograms of Pt oxides were obtained. Here, SCV is used to study the reduction of molecular oxygen. Compared to what was done by Perry [3], here, different electrolytes and oxide coverages are used and the results are discussed in terms of the sampling time, the state of the surface (reduced or oxidised) and the local *p*H. A Koutecky-Levich equivalent methodology to extract kinetic information is presented. Throughout this section, the potential waveform shown in Figure 5.1 was used.

5.2.1 Transient response

Perry and Denuault used sampled current voltammetry to study the reduction of an adsorbed oxygen species at short times [1], and although Perry obtained preliminary results with different *p*H [3], this was not studied further. Perry observed that when decreasing the *p*H of the solution, the adsorbed species could not be detected and suggested that the oxygenated species were affected by *p*H. In previous sections of the present work, it has been shown that these species are in fact oxides formed during the rest potential, and so the preliminary results obtained by Perry have to be reconsidered. In this section, sampled current voltammetry of the oxygen reduction reaction in acidic conditions is presented; the influence of different oxide coverages on the ORR is discussed.

Figure 5.4 shows sampled current voltammograms recorded in an O_2-saturated 0.1 M $HClO_4$ solution and obtained after applying the potential waveform shown in Figure 5.1 with $E_r = 1$ V vs RHE. The sigmoidal wave typical for reactions of species in solution and the increase in the limiting current with the sampling time can be observed. The SCVs were normalised with the Mahon-Oldham equation assuming $n = 1$ to reveal the presence of adsorbed species. The normalisation seems to indicate that in acidic conditions the adspecies are virtually non-existent, similar to what was observed in the preliminary experiments performed by Perry [3]. Even though the normalised current at the plateau seems to indicate the presence of a trend consistent with the presence

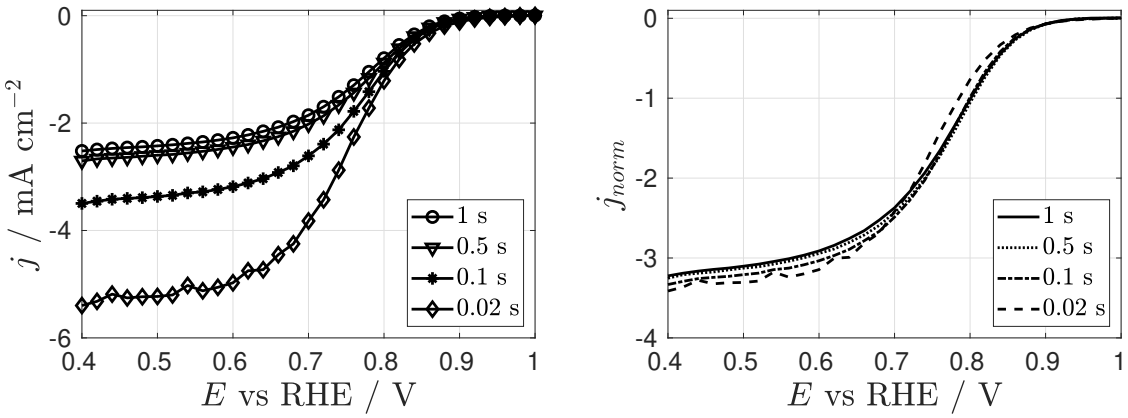

Figure 5.4: SCVs (left) and normalised SCVs (right) recorded in a solution 0.1 M $HClO_4$ saturated with O_2. The legends show the sampling times used. The potential waveform shown in Figure 5.1 was used with $E_r = 1$ V vs RHE. The SCVs were normalised with the Mahon-Oldham equation assuming $n = 1$.

of the adspecies (higher current at shorter sampling times), the values of n_{app} are not as high compared to those reported by Perry and Denuault in $KClO_4$ [1], suggesting that the coverage of the oxide is low. Comparing the SCVs in Ar-saturated solution (Figure 5.3) and that in O_2-saturated solution with $E_r = 1$ V and sampled at 100 ms, it is possible to observe that the peak current in the former is almost one order of magnitude smaller than that of the ORR at the plateau. In order to observe an effect of the oxide reduction to the current, it is necessary to increase the initial coverage.

Figure 5.5 shows normalised SCVs sampled at 0.02 s obtained after using different rest potentials. n_{app} seems to increase with E_r, consistent with the reduction of oxides at short times. A clear sign of the reduction of an oxide is the peak observed when resting at 1.4 V, this indicates that the current due to oxide reduction is comparable to that of the ORR at this sampling time; in the case of lower E_r, as that used by Perry [3], the reduction of the oxide is not evident even at short times due to the greater contribution of the ORR. Decreasing the concentration of O_2 or increasing the electroactive area of the electrode could show a peak-shaped voltammogram at all E_r and it can be a valid strategy when studying reactions that involve surface processes and dissolved species.

Figure 5.5 also shows background-subtracted SCVs sampled at 0.02 s. The background

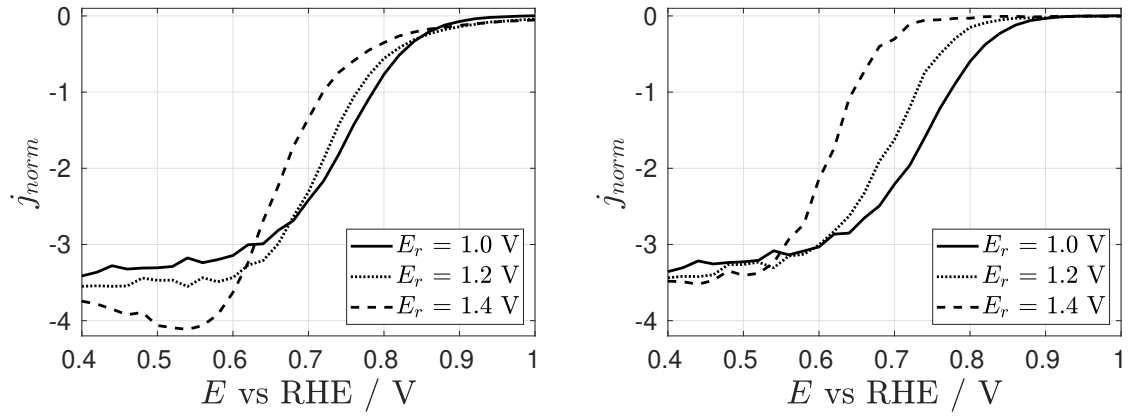

Figure 5.5: Normalised SCVs (left) and background-subtracted normalised SCVs (right) recorded in 0.1 M $HClO_4$ and sampled at 0.02 s. The potential waveform shown in Figure 5.1 was used. The SCVs were normalised with the Mahon-Oldham equation assuming $n = 1$.

subtraction removed the contribution of the reduction of the oxides; this procedure is commonly used when studying the ORR with steady state techniques [36]. After the subtraction, the normalised SCVs show values of n_{app} similar to that obtained when sampling at 1 s (considered the steady state, see Figure 5.4). The background-subtracted SCVs confirm that the extra current seen at short times is due to the reduction of oxides. The voltammograms also show that E_r strongly affects the onset potential of the ORR; this is consistent with what other groups have observed with sweep voltammetry [36, 37] and by the observations made in Chapter 4 in this work. The change in the mixed-controlled region is due to the reduction of the oxide making the ORR more difficult to proceed, and is similar to what is observed with the anodic wave obtained with sweep voltammetry. This is an important distinction between sweep voltammetry and sampled current voltammetry when studying the ORR: in the former, the anodic sweep is affected by the reduction of the oxides while the cathodic sweep is presumably oxide-free; in contrast, in SCVs, oxide-free voltammograms can only be obtained when sampling at long times, short sampling times are influenced by the reduction of the oxides.

5.2.2 Kinetic analysis

Perry and Denuault proposed an equation to obtain kinetics information from MSCV of species in solution [20]. They fitted their equation to experimental and simulated data obtaining great accuracy. Although their equation is powerful as it can be used at all sampling times and potentials, its implementation is cumbersome as the equation itself is complicated and requires non-linear fitting to three parameters (α, k_s and E^0). Instead, in this section, an analogy to the Koutecky-Levich analysis is used to obtain kinetic information.

Recalling the Koutecky-Levich analysis, a plot of the current against $\omega^{-1/2}$ would be a straight line and extrapolation to the intercept would reveal the kinetic current, i_k. The extrapolation is equivalent to obtaining the current at an infinite rate of mass transport, which is not experimentally accessible. The Koutecky-Levich plot can be generalised and rewritten in terms of the mass transfer coefficient, k_m:

$$\frac{1}{i} = \frac{1}{i_k} + \frac{1}{nFACk_m} \tag{5.1}$$

Equation 5.1 is the basis of the analysis proposed here. It can be immediately recognised that for a diffusion controlled reaction, a plot of i^{-1} against k_m^{-1} should also produce a straight line with intercept equal to i_k^{-1}. This analogy is powerful since it implies that Equation 5.1 can be used with any technique where k_m can be controlled. The simplest transient case is that of planar diffusion, where current transients plotted in this way would be the inverse to the Cotrell plot[8]. In this section, a similar analysis is attempted with a Pt microelectrode, where higher rates of mass transfer can be accessed.

To use the Koutecky-Levich analysis, it is necessary to first plot the current transients as a function of the mass transfer coefficient; recalling k_m for a microdisc elec-

[8]In a Cotrell plot, the current is proportional to t^{-1}, the equivalent Koutecky-Levich plot would be its inverse.

trode:

$$k_m = \frac{D}{a} f(Dt/a) \tag{5.2}$$

where $f(Dt/a)$ is the dimensionless function proposed by Mahon and Oldham to account for the evolution of the diffusion field in transient conditions [13]. At the ORR plateau, a plot of i against k_m should produce a straight line if the current is diffusion controlled. For RDE, this would correspond to the Levich plot, since k_m is linearly dependent on $\omega^{1/2}$ while for planar diffusion it would correspond to the Cotrell plot with k_m being proportional to $t^{-1/2}$. In the case of steady state with microelectrodes, this would correspond to a plot of i against a, although it has been reported that the use of the Koutecky-Levich analysis with hemispherical diffusion is not possible due to the non-uniformity of the current in the surface of the electrode [16, 17][9]. Instead, here, it is proposed to exploit the planar diffusion of a microdisc obtained at short times to ensure that the edge effect is minimised.

Figure 5.6 shows current transients obtained in O_2-saturated $HClO_4$ solution after resting at 0.9 V; this value of E_r was used to minimise oxide coverage. The plot shows that at low step potentials the current is mostly diffusion controlled, as expected from high overpotentials ($E_s < 0.5$ V vs RHE). When using potentials along the mixed controlled and kinetically limited region, the current tends towards a constant value at high k_m, which indicates the presence of an electron transfer step [8]; this maximum current would correspond to i_k, and although it can be obtained for potentials in the kinetically limited region, it is not accessible for more negative potentials. Instead, an equivalent Koutecky-Levich plot would allow for the recovery of i_k.

[9]With hemispherical diffusion, the current at the edges is always higher than that at the centre of the disc.

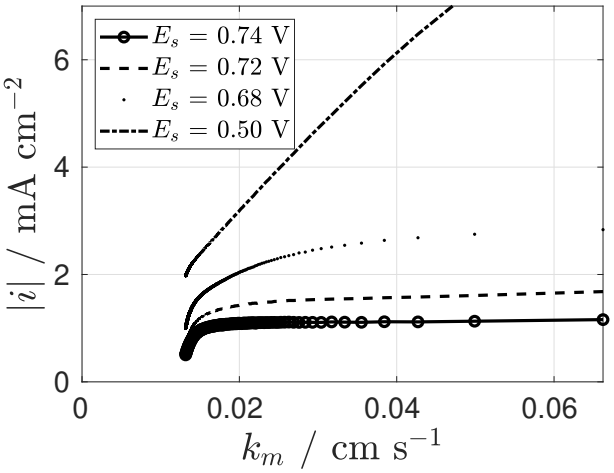

Figure 5.6: Current transients obtained by using the potential waveform shown in Figure 5.1. Air-saturated 0.1 M $KClO_4$ solution, with a Pt microelectrode (a = 25 μm).

The plot shown in Figure 5.6 can be transformed into an equivalent Koutecky-Levich plot by taking the inverse of both axis, this is represented by the black lines from Figure 5.7.

Two regions can be observed. First, a linear region is observed up to around 60 cm^{-1} s; this region corresponds to 0.0025 to 0.320 s. Recalling Figure 1.4, at the millisecond scale, the diffusion field of a microdisc with a = 25 μm is starting to deviate from planar diffusion due to edge effects. To ensure that planar diffusion dominates the current, the microsecond scale is needed, although at this time scale, the current can be affected by non-Faradaic processes, and, in the case of the ORR, by the reduction of oxides. These complications can make the measurement of i_k difficult; here, in the time scale used, it is assumed that edge effects have a small influence on the current, that the coverage of oxide is low (E_r = 0.9 V vs RHE) and that the charge and discharge of the double layer occurs in the microsecond scale. The second region that can be observed appears after the linear region as a sudden increase in i^{-1} and is due to the decrease in current at long times. In this timescale ($t > 0.32$ s) edge effects dominate the current and can not be used to access kinetic information. The following analysis concerns the linear region of the equivalent Koutecky-Levich plots.

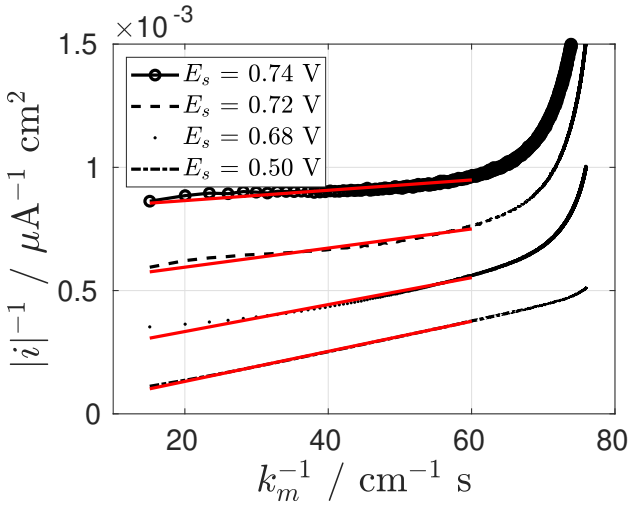

Figure 5.7: Equivalent Koutecky-Levich plots obtained from Figure 5.6. The solid lines show the Fitting to Equation 5.1.

To obtain i_k, the linear region was fitted to Equation 5.1, represented in Figure 5.7 with red solid lines. Following the Koutecky-Levich methodology, a Tafel plot was constructed by plotting i_k against E_s in a semi-log scale, see Raw curve from Figure 5.8. At high potentials a straight line can be observed; noting that this region corresponds to the kinetic and mixed controlled regions, this plot can give information about the kinetic parameters k_s and α. In the case of the ORR, it is commonly accepted to report the inverse of the slope. Here, a fitting to the linear region (red solid line) resulted in an inverse slope of 104 mV dec^{-1}, close to the expected value of 120 mV dec^{-1}; discrepancy may be due to the assumptions mentioned earlier with respect to the quasi-planar diffusion. Figure 5.8 also shows the Tafel plot obtained from background subtracted SCVs, the obtained inverse slope was 106 mV dec^{-1}. The similarity between values validates the assumption of having a low oxide coverage.

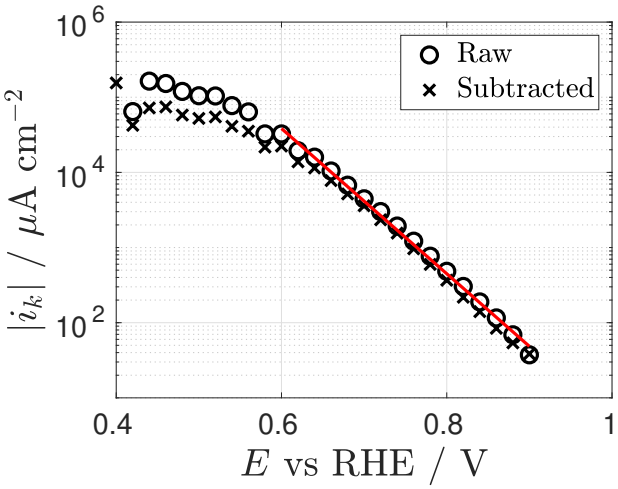

Figure 5.8: Tafel plots obtained from the Koutecky-Levich methodology for SCV. The solid line shows the linear region from where the Tafel slope can be extracted. See Figure 5.6 for details.

5.2.3 *p*H comparison

This section presents results obtained with different electrolytes. SCVs are discussed in terms of the sampling time and n_{app} followed by the use of the equivalent Koutecky-Levich analysis to obtain kinetic information of the ORR.

Figure 5.9 shows SCVs sampled at 15 s. The shift in potential due to changes of *p*H observed in $KClO_4$ is similar to the response when using sweep voltammetry (see Chapter 4). Since every point of the SCV is independent of each other, the shift in potential suggests that the local production of OH^- is too high in transient conditions, even at low overpotentials and long times (15 s), and that mass transport can not compensate it. The SCVs were normalised with the Mahon-Oldham equation assuming $n = 1$ to reveal the apparent number of electrons at the ORR plateau; this is also shown in Figure 5.9. The values of n_{app} obtained are consistent with those reported in the literature for the different electrolytes used [4, 66] and suggests that SCVs at the steady state can be used as a replacement to other steady state techniques (rotating disc, flow cells, microelectrodes) to calculate the number of electrons. Another observation can be made regarding the potential to drive the ORR: in $KClO_4$, a higher overpotential is needed than in solutions with extreme *p*H due to the ORR proceeding in alkaline

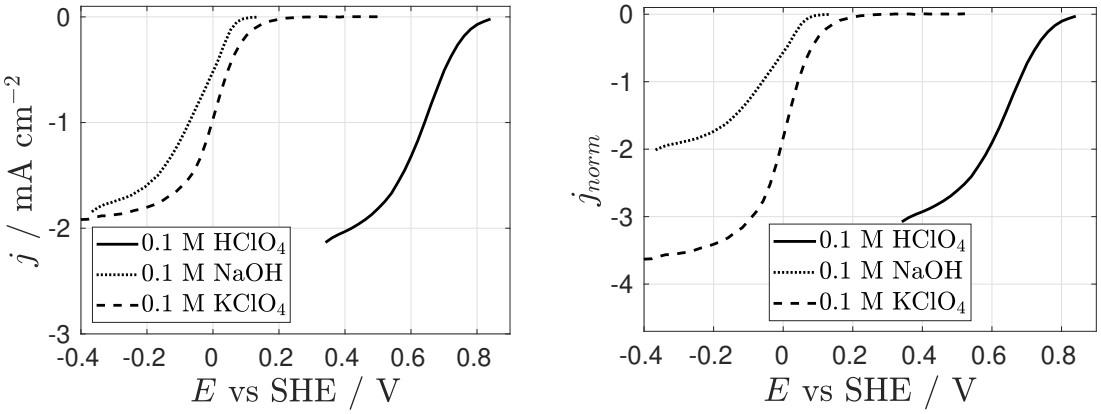

Figure 5.9: SCVs (left) and normalised SCVs (right) sampled at 15 s and recorded in O_2-saturated solutions. The potential waveform shown in Figure 5.1 was used with $E_r = 0.9$ V vs RHE. The SCVs were normalised with the Mahon-Oldham equation assuming $n = 1$.

conditions.

Figure 5.10 shows normalised SCVs sampled at 20 ms after resting at 0.9 V. All the SCVs show an increase in n_{app} from their expected value that can be related to the reduction of oxides at short times. Here, the SCV in $KClO_4$ is peak-shaped, suggesting that the contribution of oxide reduction to the total current is comparable to that of the ORR. Even though in all cases the same rest potential was used ($E_r = 0.9$ V vs RHE), the higher value of n_{app} and the peak voltammogram obtained in $KClO_4$ suggests that the coverage of the oxide is higher than that of the other electrolytes.

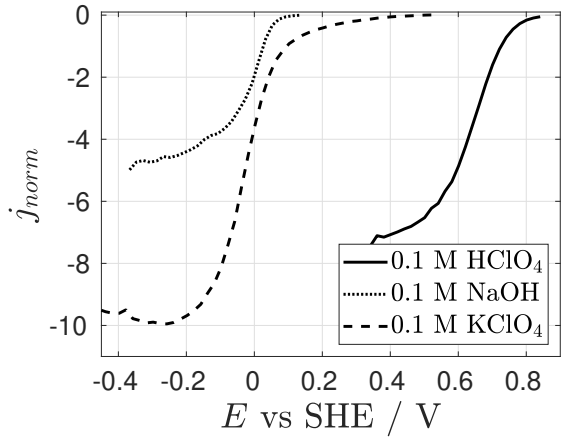

Figure 5.10: Normalised SCVs sampled at 20 ms. See Figure 5.9 for the experimental details.

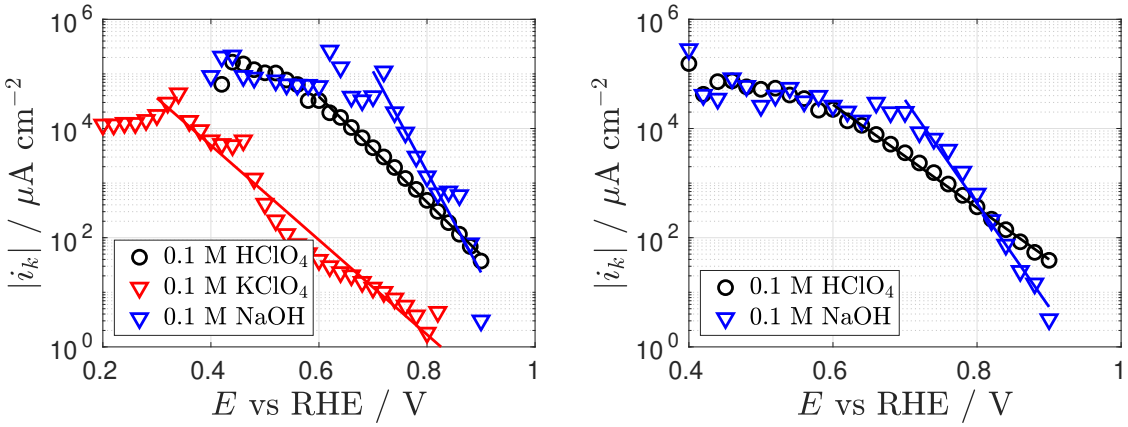

(a) Raw currents.

(b) Subtracted currents.

Figure 5.11: Tafel plots obtained from the raw and subtracted currents of SCVs. The solid line shows the linear regions from where the Tafel slopes can be extracted. See Figure 5.9 for the experimental details.

Koutecky-Levich analysis was performed with the results obtained in different electrolytes. Figure 5.11 shows the Tafel plots obtained with the raw and subtracted results. The analysis in subtracted $KClO_4$ was not performed due to the observations made in Chapter 4 regarding the different states of the surface in the presence and absence of O_2. Still, it can be observed that linear regions are present in all three electrolytes that can be related to the mixed and kinetically controlled regions; more negative potentials fall into the mass transport controlled region, where kinetic information can not be accessed. Table 5.1 shows the inverse slopes obtained from the linear regions of Figure 5.11; the results are similar to the expected values of 60 and 120 mV dec^{-1} for the ORR that are related to the higher presence of adsorbed OH^- on NaOH than in $HClO_4$ [60].

slope^{-1} / mV dec^{-1}	Raw	Subtracted
$HClO_4$	104	106
$KClO_4$	115	-
NaOH	54	53

Table 5.1: Tafel slopes obtained from Figure 5.11.

This section presented the comparison of SCVs at different pH and their relation with

the reduction of oxide and the ORR. It was shown that, similar to the results with sweep voltammetry, SCVs in $KClO_4$ are also shifted in potential due to the local changes of pH. Kinetic analysis through the equivalent Koutecky-Levich methodology resulted in Tafel slopes similar to the ones reported elsewhere [60]. It is important to stress that the analysis of the SCV in $KClO_4$ is complicated due to the continue production of OH^-. At any given time, during the reduction, the electrode behaves as a source of OH^-, effectively increasing the pH at its surface; as time is increased, OH^- diffuses away from the electrode, also increasing the pH of the surroundings while still being produced at the source. This generates a pH profile, with higher values at shorter distances from the electrode. This has several implications: the ORR always proceeds in alkaline conditions since the reaction occurs at the OH^- source (the Pt electrode), the RHE takes into account the pH at the bulk of the solution and not the pH in the surroundings of the working electrode which increases the overpotential needed to drive the reaction, and the diffusion coefficient of O_2 is affected when O_2 reaches the diffusion layer of OH^-. Due to this complications, the results obtained in $KClO_4$ have to be taken with care.

5.3 Analytical derivation of SCV of adsorbed species

The electrochemical response of adsorbed species has been well described by Laviron when he proposed a simple methodology to extract kinetic information that relies on sweeping the potential at different scan rates ν and plotting the peak potential against $\ln(\nu)$ [91]. This methodology assumes that the species is irreversibly adsorbed, that the coverage follows a first order rate law and that the rate constant has a dependency on potential according to Butler-Volmer kinetics. Following Laviron's methodology, other groups have developed methodologies to investigate the response of adsorbed species using transient and differential techniques, although their implementation and analysis to extract kinetic information is cumbersome [92, 93, 94, 95]. Voltammetric techniques are easy to implement and visually descriptive. The double layer current contribution is easy to observe, and generally, it can be subtracted by assuming that its value is

constant over the potential window of interest. Nevertheless, it is well known that adsorbed layers modify the capacitance response of electrodes [8], and the subtraction procedure may lead to errors when calculating the coverage of the adspecies. Transient techniques, on the other hand, are not as visually powerful and the extraction of kinetic information and coverage is cumbersome as it requires mathematical treatment of the data by fitting to a model [96]; on the other hand, they have the advantage that their capacitive contribution has an exponential decay. By minimising the electroactive area, the timescales of the capacitive and Faradaic currents can be separated, allowing one to record only the latter without resorting to subtraction, as it is the case for voltammetry. Furthermore, if the current at different potentials is recorded, sampled current voltammograms can be obtained, providing a visually powerful mean to obtain kinetic information that can rival classical voltammetric techniques. To construct SCVs, the current is sampled at a specific time and plotted against its respective potential. A special case is called normal pulse voltammetry (NPV), and it was introduced with the use of polarographic methods, where the current was sampled at the end of the potential step, just before the detachment of the mercury drop [8]. Due to the difficulty to implement them, NPV and SCV were replaced by more user-friendly techniques (cyclic voltammetry, chronoamperometry, etc); now, with the advent of digital potentiostats and the use of solid electrodes, sampled current voltammograms can be easily constructed and analysed.

SCV has been sporadically used to study diffusion controlled species, mostly by sampling at long times to obtain a quasi-steady state response when true steady state techniques can not be used (rotating disc electrodes, thin layer, flow cell, microelectrodes, etc.) [18, 28]. The ability to extract information at different time regimes makes SCV a powerful technique, and, although the theory to obtain kinetic information of diffusion controlled species is already developed [8, 18], its implementation can be difficult since the current sampled at short times could be influenced by the charge of the double layer. Recently, the use of microelectrodes to minimise this effect was proposed, and it was shown that this combination of techniques is specially useful to compare kinetic information at different diffusion regimes [1, 20]. In previous sections, sampled current voltammetry was used to study the presence of Pt oxides and it was revealed

that the voltammograms are peak-shaped as opposed to being sigmoidal for the case of reactions with species in solution; the present section tries to give a mathematical support to this response.

5.3.1 Theory

The following reaction where O and R are both adsorbed on the electrode surface is assumed:

$$\mathrm{O_{ads}} + n\mathrm{e}^- \underset{k_b}{\overset{k_f}{\rightleftharpoons}} \mathrm{R_{ads}} \tag{5.3}$$

where the equilibrium is controlled by the relative magnitude of the forward and backward rate constants, k_f and k_b respectively. Assuming a first order reaction, the differential equation describing the dependence of the coverage of O on time is:

$$\frac{\mathrm{d}\Gamma_{\mathrm{O}}^t}{\mathrm{d}t} = -k_f\Gamma_{\mathrm{O}}^t + k_b\Gamma_{\mathrm{R}}^t \tag{5.4}$$

It is also assumed that at $t = 0$ the coverage of O in mol cm^{-2} is given by Γ_{O}^0 and that $\Gamma_{\mathrm{R}}^0 = 0$, so that at any given time:

$$\Gamma_{\mathrm{O}}^t + \Gamma_{\mathrm{R}}^t = \Gamma_{\mathrm{O}}^0 \tag{5.5}$$

With these definitions, the differential equation is then:

$$\frac{\mathrm{d}\Gamma_{\mathrm{O}}^t}{\mathrm{d}t} = -k_f\Gamma_{\mathrm{O}}^t + k_b(\Gamma_{\mathrm{O}}^0 - \Gamma_{\mathrm{O}}^t) \tag{5.6}$$

Rearranging and by defining $K = k_f + k_b$:

$$\frac{\mathrm{d}\Gamma_{\mathrm{O}}^t}{\mathrm{d}t} = -K\Gamma_{\mathrm{O}}^t + k_b\Gamma_{\mathrm{O}}^0 \tag{5.7}$$

Solving the differential equation by change of variable:

$$\int_0^t \frac{\mathrm{d}\Gamma_{\mathrm{O}}^t}{k_b\Gamma_{\mathrm{O}}^0 - K\Gamma_{\mathrm{O}}^t} = \int_0^t \mathrm{d}t \tag{5.8}$$

$$u = k_b\Gamma_{\mathrm{O}}^0 - K\Gamma_{\mathrm{O}}^t \tag{5.9}$$

$$\mathrm{d}u = -K\mathrm{d}\Gamma_{\mathrm{O}}^{t} \tag{5.10}$$

$$-\frac{1}{K}\int \frac{\mathrm{d}u}{u} = -\frac{1}{K}\ln(u) \tag{5.11}$$

evaluating:

$$-\frac{1}{K}\ln(k_b\Gamma_{\mathrm{O}}^{0} - K\Gamma_{\mathrm{O}}^{t})\Big|_{\Gamma_{\mathrm{O}}^{0}}^{\Gamma_{\mathrm{O}}^{t}} = -\frac{1}{K}\ln\Big(\frac{k_b\Gamma_{\mathrm{O}}^{0} - K\Gamma_{\mathrm{O}}^{t}}{k_b\Gamma_{\mathrm{O}}^{0} - K\Gamma_{\mathrm{O}}^{0}}\Big) = t \tag{5.12}$$

Solving for Γ_{O}^{t} and rearranging:

$$-\frac{k_b\Gamma_{\mathrm{O}}^{0} - K\Gamma_{\mathrm{O}}^{t}}{k_f\Gamma_{\mathrm{O}}^{0}} = \exp(-Kt) \tag{5.13}$$

$$\Gamma_{\mathrm{O}}^{t} = \frac{k_b\Gamma_{\mathrm{O}}^{0} + k_f\Gamma_{\mathrm{O}}^{0}\exp(-Kt)}{K} \tag{5.14}$$

Equation 5.14 describes the coverage of O as a function of time. Since the charge describes the coverage of R:

$$Q = nF\Gamma_{\mathrm{R}}^{t} = nF(\Gamma_{\mathrm{O}}^{0} - \Gamma_{\mathrm{O}}^{t}) \tag{5.15}$$

Introducing Equation 5.14 and by defining $Q^0 = nF\Gamma_{\mathrm{O}}^{0}$, the charge is now:

$$Q = Q^0\Big[1 - \frac{k_b + k_f\exp(-Kt)}{K}\Big] \tag{5.16}$$

It is also assumed that the rate constants have a potential dependence following Butler-Volmer kinetics:

$$k_f = k_s\exp\Big(-\alpha\frac{nF}{RT}\eta\Big) \tag{5.17}$$

$$k_b = k_s\exp\Big[(1-\alpha)\frac{nF}{RT}\eta\Big] \tag{5.18}$$

where k_s is the standard rate constant for electron transfer, α is the transfer coefficient, $\eta = E - E^0$ is the overpotential, E^0 is the equilibrium potential, n is the number of electrons, F is the Faraday's constant, R is the gas constant and T is the temperature. The solution to Equation 5.7 requires that only O is present (initial condition), this is only possible through the application of an infinite positive potential before the experiment starts. Here, it is assumed that this initial potential is sufficiently positive so that the initial coverage of R is negligible.

To simplify the potential dependence on the charge, it is convenient to express the rate constants k_f and k_b as a function of ϵ according to:

$$\epsilon = \exp\Big(\frac{nF}{RT}\eta\Big) \tag{5.19}$$

$$k_f = k_s\epsilon^{-\alpha} \tag{5.20}$$

$$k_b = k_s\epsilon\epsilon^{-\alpha} \tag{5.21}$$

At infinitely long times, Q then can be expressed as:

$$Q_{lim} = Q^0\Big(1 - \frac{k_b}{k_f + k_b}\Big) = Q^0\Big(1 - \frac{\epsilon}{1+\epsilon}\Big) \tag{5.22}$$

which can be rearranged to obtain the Nernst Equation:

$$Q_{lim} = Q^0\Big(1 - \frac{1}{1+\exp(-nF\eta/RT)}\Big) \tag{5.23}$$

$$E = E^0 + \frac{RT}{nF}\ln\Big(\frac{Q^0 - Q_{lim}}{Q^0}\Big) \tag{5.24}$$

With these definitions, Equation 5.16 can be rearranged and simplified:

$$Q = Q^0\Big[1 - \frac{\epsilon}{1+\epsilon} - \frac{\exp(-Kt)}{1+\epsilon}\Big] \tag{5.25}$$

$$Q = Q_{lim} - \frac{Q^0}{1+\epsilon}\exp(-Kt) \tag{5.26}$$

noting that

$$Q_{lim} = \frac{Q^0}{1+\epsilon} \tag{5.27}$$

the charge Q at any given potential and time can be described by:

$$Q = Q_{lim}[1 - \exp(-Kt)] \tag{5.28}$$

Equation 5.28 is akin to the charge of a pseudo-capacitor where its time constant is given by $1/K$ and can be used to estimate the rate constant K with a non-linear fitting of Q/Q_{lim} against t; the mathematical treatment to obtain kinetic parameters will be

presented in following sections. With $j = \mathrm{d}Q/\mathrm{d}t$ and Equation 5.22, the current density as a function of potential and time is:

$$j = Q^0 k_f \exp(-Kt) \tag{5.29}$$

Equation 5.29 has the same form as the one reported for the complete irreversible case, when $K = k_f$ [96, 97, 98, 99]; the main difference is that it takes into account the backward reaction.

Figure 5.12 shows the charge and current transient responses according to Equations 5.28 and 5.29. Only two potentials are shown to facilitate the comparison. This plot shows the relationship between charge and current with the reaction given by Equation 5.3, where the current shows the consumption rate of species O while the charge shows the increase in coverage of R. The plateau reached by the charge density does not correspond to Q^0, instead, it shows a dependence on potential and is a result of the backward reaction controlling the ratio of O and R as given by the Nernst equation, then, at infinite times it is possible to use Equation 5.23 to calculate Q^0 and E^0 by recording the charge at two different potentials.

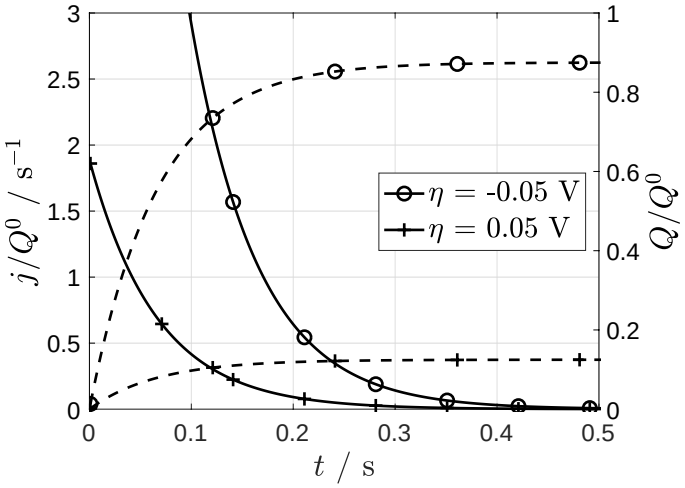

Figure 5.12: Normalised charge (right axis, dashed lines) and current (left axis, solid lines) transients from Equations 5.28 and 5.29 respectively, calculated with $n = 1$, $\alpha = 0.5$ and $k_s = 5$ s^{-1}. The legend indicates the overpotentials used.

Figure 5.13 shows the plots of Equations 5.28 and 5.29 as a function of time and potential. The projections show selected sampled and transient plots. Figure 5.13

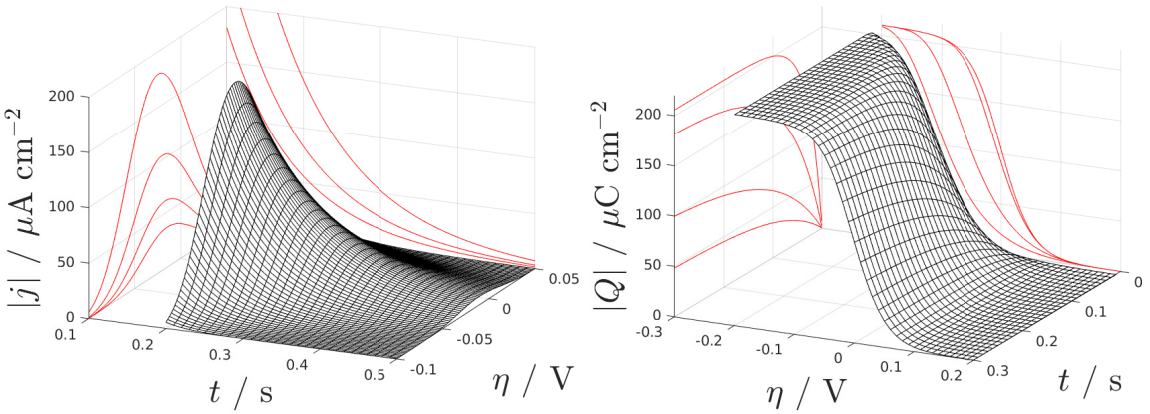

(a) j - t - η plot. **(b)** Q - t - η plot.

Figure 5.13: Plots of j (left) and Q (right) as a function of t and η. $Q^0 = 210$ μC cm^{-2}. See Figure 5.12 for the rest of the parameters used.

shows that sampled current voltammograms are peak shaped, while sampled charge voltacoulograms are sigmoidal. In order to obtain kinetics information, it is necessary to analyse the transients at short times, since at long times the charge reaches Q_{lim} while the current reaches zero due to the full consumption of O; a timescale that allows for the quantification of kinetic information has to be estimated.

Figure 5.14 shows the projection of Q and j onto the t-η plane normalised by Q^0 and j_{peak} respectively. The SCVs and SQVs can be recovered by sampling the plots at a fixed time, while the chronocoulograms can be recovered by keeping a potential constant and moving along the t axis. Due to the normalisation, the chronoamperograms can not be visualised in this way, as the current at short times would be several orders of magnitude higher than in the rest of the plot. The transition region observed in the charge plots correspond to the rising part of the sigmoidal SQVs. This region contains the dependence of Q on η. At long times, kinetic information is not accessible, as the charge reached Q_{lim}. Focusing on a fixed value of the charge, $Q/Q^0 = 0.5$ represented in the plot in cyan, it can be seen that a combination of short times and negative potentials are needed to achieved that charge, and the shorter the time, the more negative the potential required, for more positive potentials, the charge reaches the equilibrium and do not depend on time any more. Then, kinetics information is only accessible at short sampling times and negative potentials. For a system with a lower

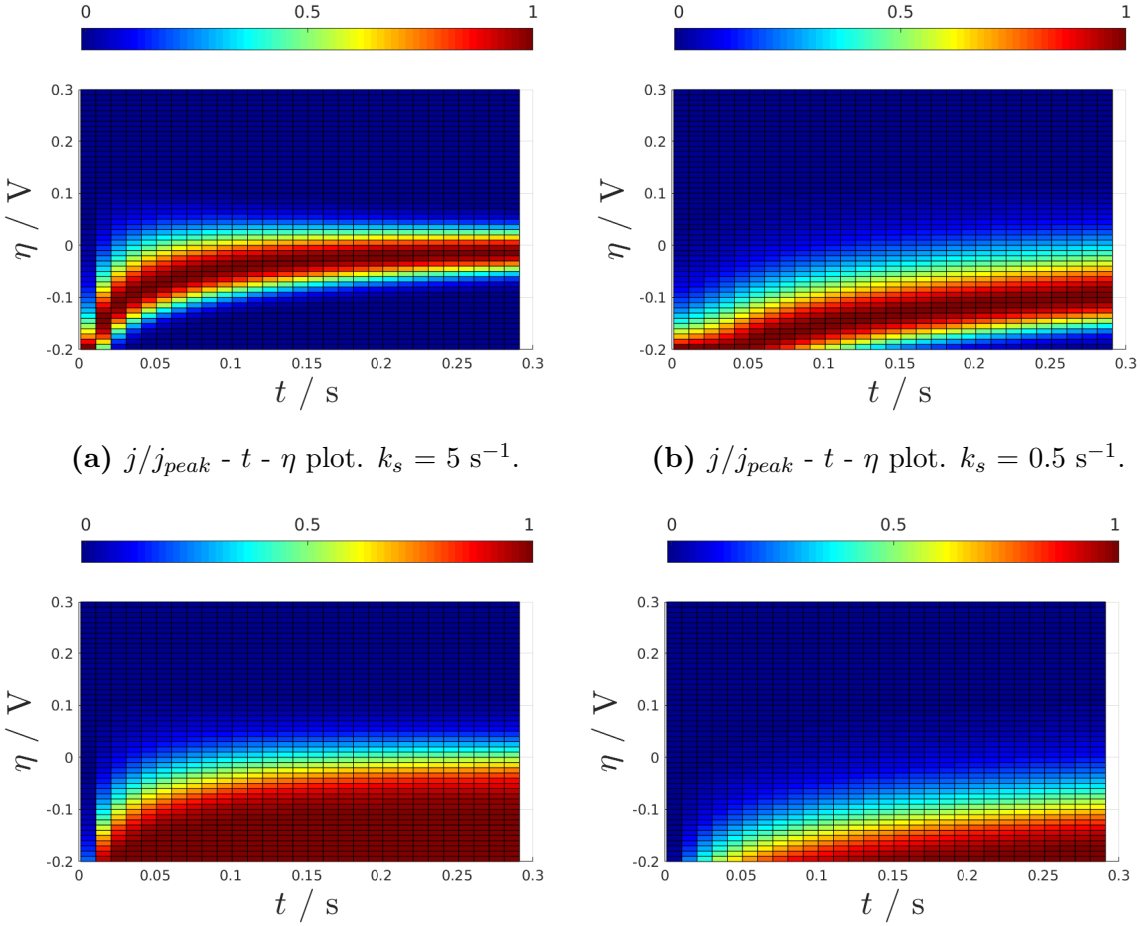

(a) j/j_{peak} - t - η plot. $k_s = 5\ \mathrm{s}^{-1}$.

(b) j/j_{peak} - t - η plot. $k_s = 0.5\ \mathrm{s}^{-1}$.

(c) Q/Q^0 - t - η plot. $k_s = 5\ \mathrm{s}^{-1}$.

(d) Q^0 - t - η plot. $k_s = 0.5\ \mathrm{s}^{-1}$.

Figure 5.14: Projection of j/j_{peak}, Q/Q^0 and Q/Q_{lim} onto the t-η plane with different k_s. See Figure 5.12 for the rest of the parameters used.

k_s, as in Figures 5.14b and 5.14d, the time where kinetic information can be accessed is increased. A similar analysis can be made with the plots of the current. Here, the transition region represents the peak of the SCVs. At long times, the peak current ($j/j_{peak} = 1$) approaches the equilibrium potential and so lower times are required to obtain kinetic information, in agreement with the charge plots. In the following sections, different methodologies to obtain kinetic information from current transients are presented.

5.3.2 Tafel analysis

Equation 5.28 is akin to the charge of a pseudo-capacitor with a time constant $1/K$. To reach approximately 95 % of the final coverage, a characteristic time can be defined as $\tau = 3/K$; this would correspond to the maximum time where kinetic information can be obtained. A plot of τ against overpotential is given in the left axis of Figure 5.15, where it can be seen that this characteristic time is maximised at the equilibrium potential for $\alpha = 0.5$ and shifts up to $E^0 + 25$ mV for transfer coefficients between 0.3 and 0.7 (see Figure 5.16); applying a potential in this region would make the reaction proceed slowly enough to make the kinetic regime last longer with the drawback of reaching only 50 % of a monolayer, as allowed by the Nernst equation.

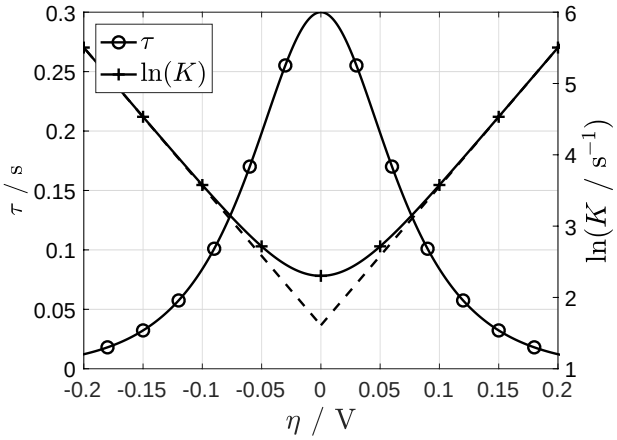

Figure 5.15: Plots of $\ln(K)$ (right axis) and τ (left axis) against η calculated with $n = 1$, $\alpha = 0.5$ and $k_s = 5$ s^{-1}. The dashed lines show the extrapolation to E^0.

Figure 5.15 also shows a plot of $\ln(K)$ against overpotential (right axis), where a linear region at high overpotentials is present. The branches seen correspond to the logarithmic plots of k_f and k_b and the values of k_s and α can be obtained, as traditionally done with Tafel plots, from the intercept and slope respectively (Equations 5.17 and 5.18). The dashed lines show the extrapolation of the linear regimes; E^0 would correspond to the potential where both lines intersect and, contrary to the plot of the characteristic time, it does not depend on the value of the transfer coefficient (see Figure 5.16). Experimentally, K can be obtained by fitting Equation 5.28 to chronocoulograms normalised by their respective plateau or by linearisation of the current transients. For a

process with slow kinetics, this methodology may suffice, however, for a system with higher k_s, obtaining K from Equation 5.28 can lead to errors, since it requires a wide range of overpotentials to ensure that the branches can be clearly distinguished. In the following sections, the analysis of sampled current voltammograms is introduced and shows that kinetic information can be obtained at any range of overpotentials, provided the value of τ falls into the timescale of the instrument.

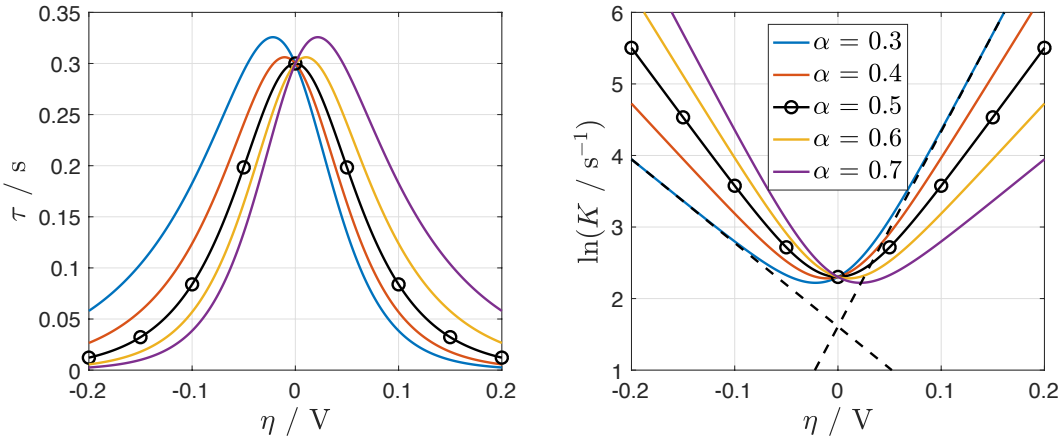

Figure 5.16: Effect of the transfer coefficient α on the characteristic time τ (left) and on $\ln(K)$ (right). Calculated from Equations 5.17 and 5.18 with $k_s = 5$ s^{-1} and $n = 1$. The dashed line in plot of $\ln(K)$ shows the extrapolation to E^0 of the cathodic and anodic branches.

5.3.3 Laviron analysis

This section concerns with the analysis of SCVs to obtain kinetic parameters of adsorbed species in the absence of diffusion. SCVs and SQVs for an adsorbed species at different sampling times are shown in Figure 5.17. As the sampling time is decreased, the waves shift to more negative potentials away from the equilibrium potential. A similar behaviour is observed with voltammetric techniques when the scan rate ν is increased; in this case, the values of k_s and α can be obtained by extrapolating the linear region observed in plots of E_{peak} against $\ln(\nu)$ [91]. This requires obtaining voltammograms at a wide range of ν to ensure that the linear region is not mistaken with the quasi-reversible behaviour.

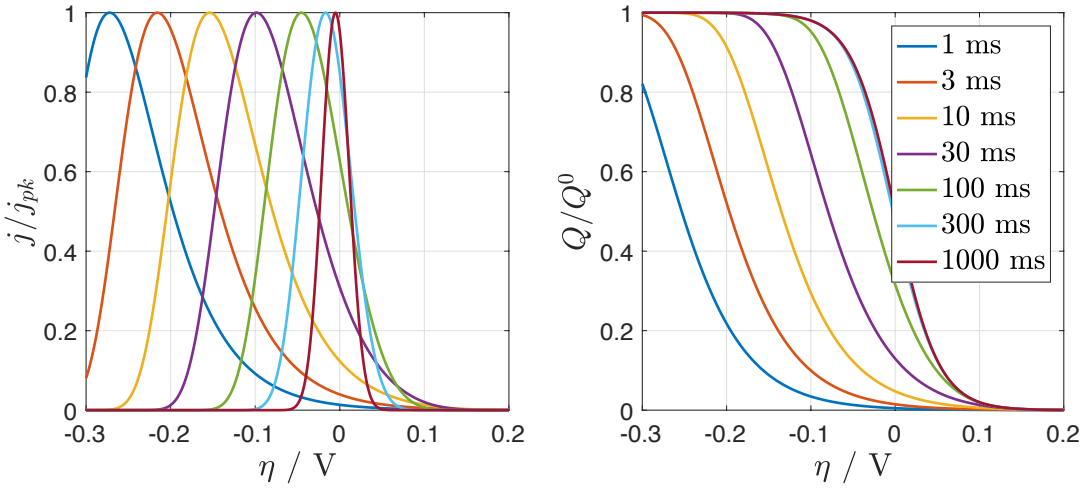

Figure 5.17: Sampled current voltammograms (left) and sampled charge voltacoulograms (right) for different sampling times. Calculated from Equations 5.29 and 5.28 respectively with $Q^0 = 210\ \mu\text{C cm}^{-2}$, $n = 1$, $k_s = 5$ and $\alpha = 0.5$. The SCV is more sensitive to kinetics than the SQV, as seen by the greater shift of the waves at long sampling times.

Following a similar approach as that reported by Laviron for voltammetry [91], the peak potential and current of an SCV can be obtained analytically if only the forward reaction is taken into account:

$$\text{O}_{\text{ads}} + n\text{e}^- \xrightarrow{k_f} \text{R}_{\text{ads}} \tag{5.30}$$

the equation for the coverage is:

$$\frac{\text{d}\Gamma_{\text{O}}^t}{\text{d}t} = -k_f \Gamma_{\text{O}}^t \tag{5.31}$$

and its solution is straight forward:

$$\Gamma_{\text{O}}^t = \Gamma_{\text{O}}^0 \exp(-k_f t) \tag{5.32}$$

with charge and current given by:

$$Q = Q^0[1 - \exp(-k_f t)] \tag{5.33}$$

$$j = Q^0 k_f \exp(-k_f t) \tag{5.34}$$

The initial charge Q^0 is always reached for the case of no backward reaction, provided enough time is given to the experiment; this is contrary to the case when the backward

reaction is taken into account, Equation 5.28, where the final charge reached after infinite time is controlled by the ratio between the oxidised and reduced adsorbed species.

The second derivative of the coverage on potential carries the information of the peak potential (E_{peak}) and current (j_{peak}) as a function of the sampling time:

$$\frac{\mathrm{d}^2\Gamma_{\mathrm{O}}^t}{\mathrm{d}\eta^2} = 0 \tag{5.35}$$

Obtaining first and second derivatives:

$$\frac{\mathrm{d}\Gamma_{\mathrm{O}}^t}{\mathrm{d}\eta} = \Gamma_{\mathrm{O}}^0 \frac{\alpha n F t}{RT} k_f \exp(-k_f t) \tag{5.36}$$

$$\frac{\mathrm{d}^2\Gamma_{\mathrm{O}}^t}{\mathrm{d}\eta^2} = \Gamma_{\mathrm{O}}^0 \Big(\frac{\alpha n F}{RT}\Big)^2 k_f t (k_f t - 1) \exp(-k_f t) \tag{5.37}$$

To fulfil the condition given by Equation 5.35, it is necessary to set $k_f t = 1$ so that the term $(k_f t - 1) = 0$. Substituting $k_f = 1/t$ in Equation 5.20 and solving for E_{pk}:

$$\frac{1}{t} = k_s \exp(-\alpha \frac{nF}{RT} \eta_{pk}) \tag{5.38}$$

$$\ln\Big(\frac{1}{k_s t}\Big) = -\alpha \frac{nF}{RT} \eta_{pk} \tag{5.39}$$

$$E_{pk} = E^0 - \frac{RT}{\alpha n F} \ln\Big(\frac{1}{k_s t}\Big) \tag{5.40}$$

After substituting Equation 5.40 in Equation 5.34:

$$j_{pk} = \frac{Q^0}{t} \exp(-1) \tag{5.41}$$

Equation 5.41 describe the peak potential and peak currents respectively as a function of the sampling time. Figure 5.18 shows this at short (left) and long (right) times for a system that contains both forward and backward reactions; it can be seen that Equation 5.41 predicts the peak currents only at short times, where it can be assumed that the backward reaction does not influence the current.

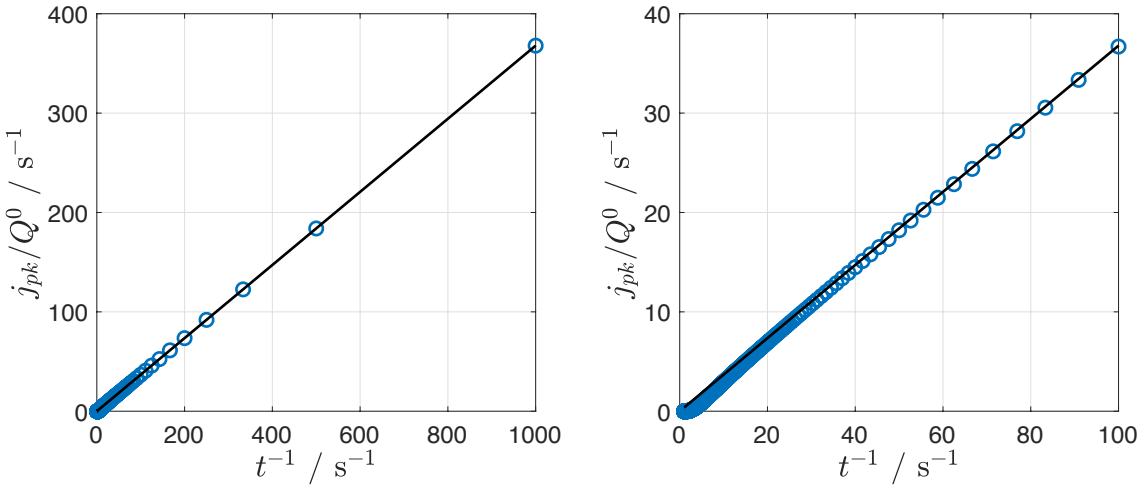

Figure 5.18: Peak current from SCVs as a function of the sampling time, the right plot shows longer times. SCVs obtained from Equation 5.29 with $Q^0 = 210$ μC cm^{-2}, $n = 1$, $k_s = 5$ s^{-1} and $\alpha = 0.5$. The solid line represents Equation 5.41 and it shows a good agreement at short times (left plot, irreversible behaviour) but not at long times (right plot, quasi-reversible and reversible behaviours).

To obtain kinetic information, it is possible to construct an equivalent Laviron plot as E_{pk} against $\ln(1/t)$. Figure 5.19 shows some examples obtained with different values of k_s. The linear region seen at short times can be extrapolated to $\eta = 0$ to obtain a characteristic time $t_{Laviron}$, that is, Equation 5.39 is now:

$$\ln\left(\frac{1}{k_s t_{Laviron}}\right) = 0 \tag{5.42}$$

which can only be true if $k_s = 1/t_{Laviron}$. The value of the transfer coefficient can be readily obtained from the slope of the linear region, by noting from Equation 5.40:

$$s = -\frac{RT}{\alpha n F} \tag{5.43}$$

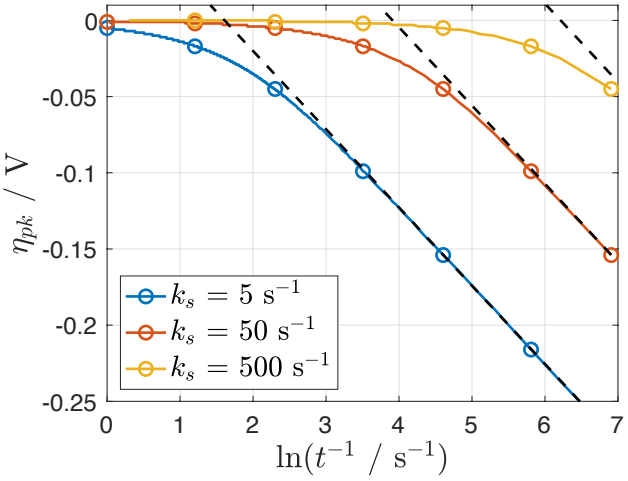

Figure 5.19: Equivalent Laviron plots for different rate constants. SCVs obtained from Equation 5.29 with $Q^0 = 210\ \mu\mathrm{C\ cm}^{-2}$, $n = 1$ and $\alpha = 0.5$. The dashed line represents Equation 5.40 for each k_s.

This methodology is presented as an analogy of that proposed by Laviron for voltammetric techniques [91], and as such, has similar constraints. For a system with high k_s, short sampling times are required to ensure that the plot of η_{pk} against $\ln(t^{-1})$ shows the linear region. In addition, a high number of potential steps are required to resolve the peaks. The following section introduces a new methodology that exploits SCVs to obtain kinetic information for systems with higher k_s.

5.3.4 Logarithmic SCVs

This section presents a methodology to extract kinetic information with sampled current voltammograms. Figure 5.20 shows the comparison between normalised sampled current voltammograms and normalised sampled charge voltacoulograms. The sigmoidal shape of the SQV is a direct consequence of the charge being proportional to the amount of O that has reacted, Equation 5.28. Kinetic limitations are seen as a shift in the potential for short sampling times, while at long times the wave tends towards the equilibrium, Equation 5.23. Experimentally, the equilibrium can only be seen in SQVs sampled at long times due to the cumulative nature of the charge; in contrast, at long times the current decays to zero as the process is finished.

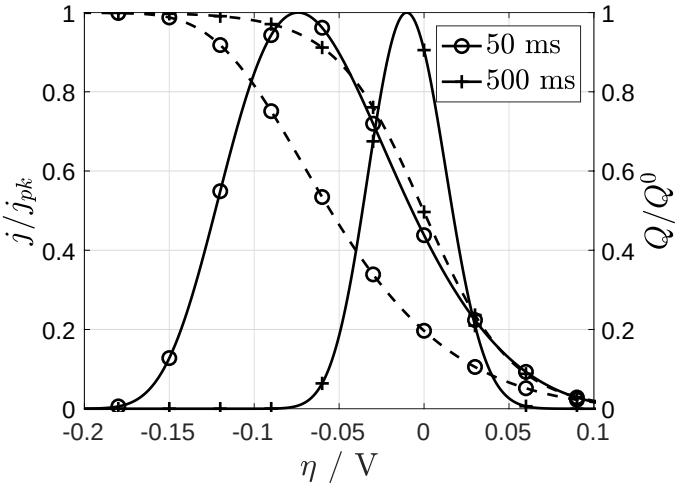

Figure 5.20: Normalised sampled current voltammograms (left axis, solid lines) and normalised sampled charge voltacoulograms (right axis, dashed lines) calculated with $n = 1$, $\alpha = 0.5$ and $k_s = 5$ s^{-1}.

In this section a methodology is proposed to analyse sampled current voltammograms in order to obtain kinetic information without the need to apply a large number of potential steps. First, linearising Equation 5.29:

$$\ln(|j|) = \ln(Q^0 k_f) - Kt \tag{5.44}$$

Equation 5.44 indicates that $\ln(|j|)$ should be a linear function of time; while this is true and it can be used to obtain the value of the rate constants through the plot of $\ln(K)$ againts E (Figure 5.15), this is only possible for systems with low k_s or when a wide range of potentials can be applied. Applying Equation 5.44 to sampled current voltammograms is visually more powerful, since the evolution of the kinetic regime as a function of the sampling time is revealed. This is shown in Figure 5.21, where the peaks seen in the sampled current voltammograms are now turned into parabolas with an increasing flattened region as the sampling time decreases.

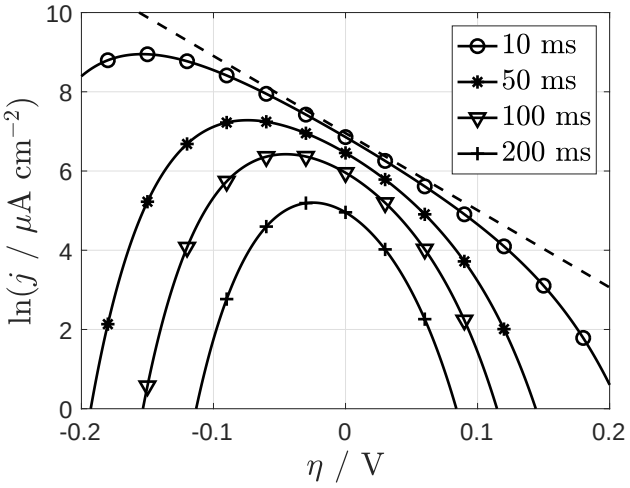

Figure 5.21: Logarithmic sampled current voltammograms calculated with $n = 1$, $\alpha = 0.5$ and $k_s = 5\ \mathrm{s}^{-1}$. The dashed line represents the irreversible case, Equation 5.45.

At the limiting case when $t = 0$, the second term in Equation 5.44 disappears and the intercept can be simplified to:

$$\ln(|j^0|) = \ln(Q^0 k_s) - \alpha \frac{nF}{RT}\eta \tag{5.45}$$

where j^0 refers to the extrapolated current at $t = 0$. Equation 5.45 would correspond to the case when no backward reaction is assumed, where $\ln(j^0)$ is a linear function of potential (this has been represented in Figure 5.21 with a dashed line). In this way, by recording current transients at different potentials and extrapolating them to the no backward reaction case that would be obtained at infinitely short sampling times, the transfer coefficient can be obtained from the slope of Equation 5.45. Once the value of α is known, it can be used to obtain k_s from $K = k_f + k_b$, and finally, the value of Q^0 from the intercept.

The analysis of SCVs has a clear advantage over traditional voltammetry: in SCV, the current transients can be extrapolated to $t = 0$. This can be seen graphically in logarithmic SCVs, as they are sensitive to k_s, contrary to normal SCVs or even SQVs (see Figure 5.17); as long as an effect in the logarithmic SCV is shown, kinetic information can be obtained by extrapolating to the complete no backward reaction case. In contrast, Laviron's methodology for voltammetry requires the use of a wide window of scan rates to clearly distinguish the kinetic regimes that can be limited by

the instrument and so high k_s may not be accessible. Using Laviron's methodology with SCV (Equations 5.40 to 5.43) has similar constraints: a wide range of sampling times is needed, in addition to a high number of potential steps to be able to resolve the peaks.

5.3.5 Double layer capacitance

An important issue to assess is the impact of the double layer capacitance that appears at short sampling times. Similar to electroadsorbed species, capacitive currents follow an exponential decay [8]:

$$i = \frac{E}{R_s}\exp(-t/R_sC_d) \tag{5.46}$$

where E is the potential applied, R_s is the solution resistance, and C_d is the double layer capacitance. Equation 5.46 indicates that the sampled current voltammogram of a capacitor would be a linear function of potential, with an intercept at $i = 0$ and slope $R_s^{-1}\exp(-t/R_sC_d)$, where t is the sampling time. Furthermore, Equation 5.46 can be linearised to obtain the values of R_s and C_d from the intercept and slope respectively:

$$\ln(i) = \ln\Big(\frac{E}{R_s}\Big) - \frac{t}{R_sC_d} \tag{5.47}$$

In this way, SCVs sampled at short times would reveal capacitive currents as linear regions, as opposed to peaks for adsorbed species (this work) and sigmoidal waves for diffusion controlled reactions [8, 20]. If the value of C_d and R_s can be obtained, a safe time constant to start measuring kinetics of electroadsorbed species independently would be $\tau = 5\,C_dR_s$; this imposes an upper limit on the rate constants that can be measured, corresponding to $K = 1/\tau$. Experimentally, to reduce the time constant τ and to access higher rates of electron transfer, smaller electrode areas need to be used. The methodology proposed here is then directly applicable to microelectrodes, since their time constants are typically in the microsecond scale. In fact, this methodology can be used with any electrode such that the charge and discharge of its double layer is over within the first current data point acquired by the instrument.

In order to access kinetic information from high rate constants, a short timescale is

needed (high ν for LSV, short τ for transients); at this time scales, the charging of the double layer may affect the measurement of the kinetic parameters. The charge of the double layer is a function of both, the applied potential E, and time t and it depends on the capacitance C in F cm^{-2} and the solution resistance R_s according to Equation 5.48:

$$Q_{DL} = ECR_f\Big[1 - \exp\Big(-\frac{t}{R_sCAR_f}\Big)\Big] \tag{5.48}$$

where A is the geometrical area and R_f is the roughness factor. The characteristic time of a capacitor is then R_sCAR_f, and it can be proved that to charge the capacitor up to approximately 95 % of its maximum value, the time needed is $\tau_{DL} = 3R_sCAR_f$. The solution resistance R_s has to be calculated; for the case of a macroelectrode:

$$R_s = \frac{x}{\kappa A} \tag{5.49}$$

and for a microelectrode:

$$R_s = \frac{1}{4\kappa a} \tag{5.50}$$

where x is the distance between the Luggin capillary and the working electrode, a is the radius of the microelectrode and κ is the conductivity of the solution. With these definitions, the expressions for the charge of the double layer for both electrodes are:

$$Q_{macro} = ECR_f\Big[1 - \exp\Big(-\frac{\kappa t}{xCR_f}\Big)\Big] \tag{5.51}$$

$$Q_{micro} = ECR_f\Big[1 - \exp\Big(-\frac{4\kappa t}{\pi aCR_f}\Big)\Big] \tag{5.52}$$

In both cases, the time constant depends on a characteristic length, being the Luggin-electrode distance for the macroelectrode (x) and the radius for the microelectrode (a). The smaller time constant for the latter is one of the advantages of using small electrode sizes, this allows the exploration of shorter time scales without the influence of the charging of the double layer. Figure 5.22 shows the charges as a function of time for different electrode sizes assuming $C = 20\,\mu F$ cm^{-2}, typical for Pt in H_2O, κ = 0.0632 Ω^{-1} cm^{-1}, typical for 0.5 M NaCl, $A_{macro} = 1\,\text{cm}^2$, $E = 0.1$ V, $R_f = 5$ and x = 0.1 cm. As expected, the characteristic time decreases with the size of the electrode, going from 1 ms for a macroelectrode to about 20 μs for a microelectrode with $\phi = 50$ μm.

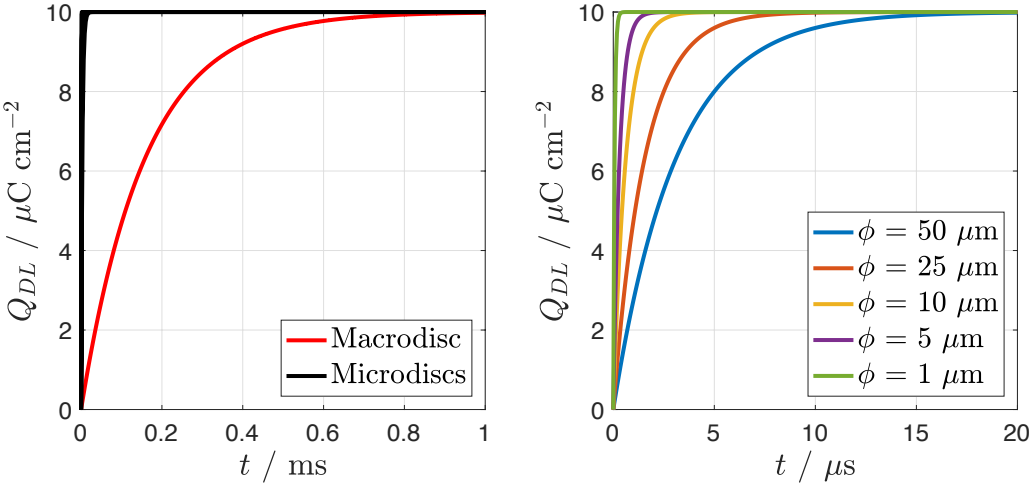

Figure 5.22: Charging of the double layer for different sizes of electrodes, calculated with Equations 5.51 and 5.52 assuming $C = 20\ \mu F\ \text{cm}^{-2}$, typical for Pt in H_2O, $\kappa = 0.0632\ \Omega^{-1}\ \text{cm}^{-1}$, typical for 0.5 M NaCl, $A_{macro} = 1\ \text{cm}^2$, $E = 0.1$ V, $R_f = 5$ and $x = 0.1$ cm.

The charge of an adsorbed layer, according to Equation 5.28 and reproduced here is:

$$Q = Q_{lim}[1 - \exp(-Kt)] \tag{5.53}$$

this equation has the same form as that for the double layer, Equation 5.48, and gives the ability to treat the consumption of species O as a pseudo-capacitor. By analogy, the time constant to reduce 95 % of the oxidised species is:

$$\tau_{ads} = \frac{3}{K} \tag{5.54}$$

contrary to the time constant for the double layer, $\tau_{DL} = 3R_uCAR_f$, τ_{ads} depends on potential due to $\epsilon = \exp(nF\eta/RT)$ and the standard rate constant for electron transfer, k_s. Figure 5.23 shows this plot, where τ_{ads} goes through a maximum at E^0, and its magnitude is controlled by the rate constant.

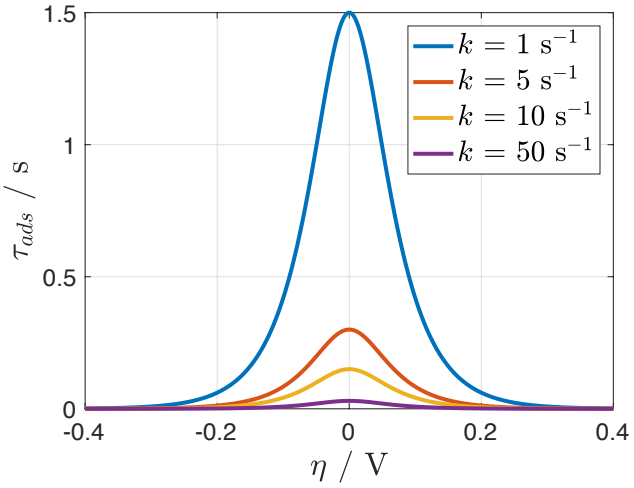

Figure 5.23: Dependence of the characteristic time of an adsorbed layer, τ_{ads}, as a function of potential, according to Equation 5.54. k in the plot refers to k_s.

The potential dependence can be explained as follows. At $E >> E^0$, the driving force for the reaction is small, but also, only a small amount of Γ_O can react at that potential according to the Nernst equation, and so τ_{ads} is small. When $E << E^0$, the equilibrium requires more coverage to react but the driving force is high and so the characteristic time is also small, that is, O is reduced faster. At precisely $E = E^0$, a balance is achieved and τ_{ads} is maximum. This implies that the reaction takes longer to complete at E^0, giving more time to obtain kinetic information than at other potentials. The dependence of τ_{ads} on potential can also be seen in the chronocoulograms. Figure 5.24 shows chronocoulograms normalised by the Nernst equation for different potentials. The time for 95 % of the charge agrees with what is predicted by Equation 5.54 and Figure 5.23, where the maximum τ_{ads} is obtained at E^0 (Equation 5.55), and the time constants decrease as E moves away from E^0. If the value of E^0 is known, then k_s can be obtained directly from Equation 5.55; in fact, the general expression for the time constant, Equation 5.54, has a dependency on α and k_s and if two chronocoulograms at different potentials are recorded, the problem can be treated as a system of two equations with two unknowns (α and k_s) to solve for both parameters. This is a fast way of obtaining kinetic information but it requires a non-linear fit to Equation 5.28 to obtain each time constant.

$$\tau_{E^0} = 1.5/k_s \tag{5.55}$$

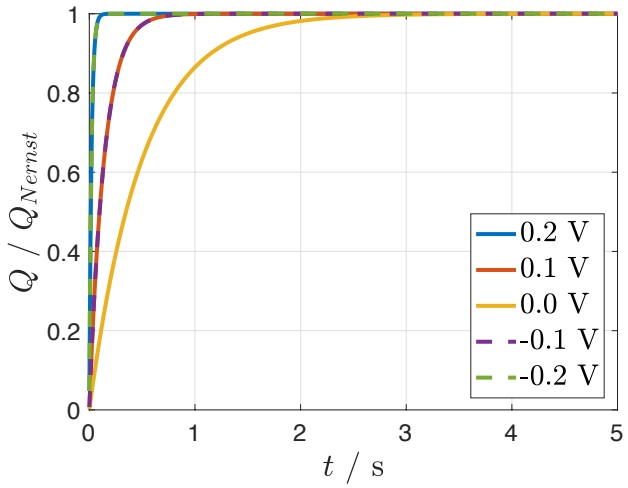

Figure 5.24: Chronocoulograms normalised by Q_{lim} for different η.

With the analysis made so far, it is clear that the charge of the double layer and the charge of the pseudo-capacitor due to the adsorbed species can occur at different timescales. To study the latter, the shortest time that can be used would be limited by the characteristic time of the double layer, while the longest would be limited by the potential used and it will be maximum at E^0. To see the range of k_s that can be studied on transient conditions, the characteristic time of the adsorbed species at E^0 was plotted against the standard rate constant and compared with the characteristic time of the double layer. In Figure 5.25 the plot shows that a macroelectrode can be used even at $k_s = 50$ s^{-1}, this is because the charge of the double layer was completed in less than 1 ms, while 50 s^{-1} would correspond to $\tau_{ads} = 30$ ms (Equation 5.55), that is $\tau_{DL} << \tau_{ads}$.

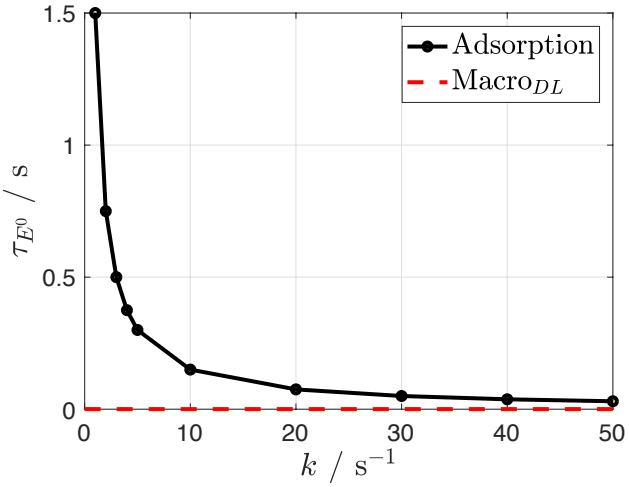

Figure 5.25: Calculated time constants at E^0 for the adsorption process and the charging of the double layer of a macroelectrode for different values of k_s. k in the plot refers to k_s.

The time constants obtained for higher values of k_s are shown in Figure 5.26, where the time for the double layer of microelectrodes is also included. Due to the fast charging of the microelectrodes giving by the expression of the solution resistance, Equation 5.50, higher values of rate constant ($k_s > 100\text{x}10^3$ s^{-1}) can be accessed.

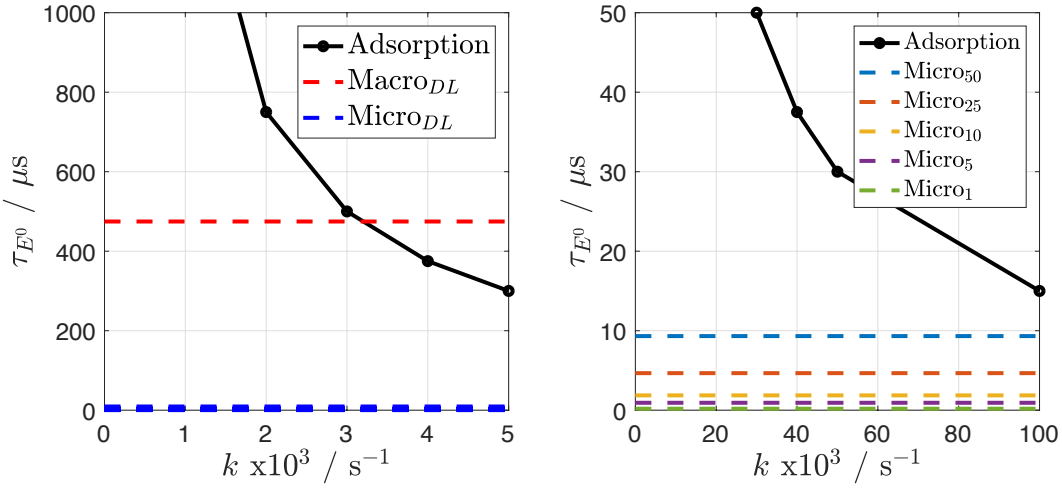

Figure 5.26: Calculated time constants at E^0 for the adsorption process and the charging of the double layer of a macroelectrode for high values of k_s. The time constants for the double layer charging of different sizes of electrodes is also included. k in the plot refers to k_s.

Chapter 6

Conclusions and future work

This work is a continuation of the project started by Perry and Denuault, where it was observed that an oxygenated species was adsorbed on Pt microelectrodes after exposure to dissolved oxygen [1, 2, 3]. The adsorbed species were detected due to the specific conditions used, namely the use of a neutral and unbuffered electrolyte (0.1 M $KClO_4$), the analysis of current transients in the millisecond scale, the use of microelectrodes that were not affected by capacitive currents in transient conditions, as well as the potential waveform used. One of the major problems was the difficulty to separate the current contribution of the adsorbed and dissolved oxygen species, as their reduction occurs at similar potentials. To solve this, Perry and Denuault subtracted a theoretical diffusion controlled current that assumed a constant value of n_{app}; this theoretical current was used as a substitute to the reduction of dissolved oxygen. The integration of the subtraction allowed them to obtain a charge ascribed to the reduction of the adsorbed species. Although this methodology showed promising results, it was believed that the charge was underestimated due to the value of n_{app} decreasing with increasing mass transfer coefficients, and also, the identity and source of the adspecies was unknown.

In Chapter 3 of this work, their methodology was improved by exploiting the mass transfer coefficient. The use of small microelectrodes ensured that the mass transport controlled rate of the oxygen reduction reaction was quickly established. In this way the

current due to the ORR remained almost constant in the timescale of the experiment and any deviations corresponded to the reduction of the adsorbed species. This was confirmed with the use of a sub-micron spherical electrode and a carbon fibre microdisc electrode with Pt nanoparticles. In this way, a more precise value of Q was obtained using electrodes that allowed the assumption of a constant n_{app} to be valid.

Chapter 3 also introduced a stripping voltammetry methodology to measure the charge of adsorption in a more visual and fast way that does not depend on a theoretical equation. The methodology relies on recording several cycles after the oxygen species were adsorbed on the electrode; the current of the first cycle would have the contribution of the adsorbed oxygen species and the reduction of molecular oxygen, while subsequent cycles would only have the contribution of the latter. In this way, a direct subtraction of the cycles would generate a voltammogram for the reduction of the adsorbed species. As this methodology does not depend on a theoretical equation, it can be used with any diffusion regime (planar, hemispherical, hindered). The methodology has the added advantage of subtracting non-Faradaic currents and so it can be used with electrodes that possess a high electroactive area (macroelectrodes, nanoparticle-based catalysts), as well as with systems where adsorbed and dissolved species have similar redox potentials. The use of different electrode geometries is proposed as future work, specifically, using nanoparticle-based catalysts to test for the presence of the adsorbed oxygen species, as it is believed that nanoparticles adsorb oxygenated species too strongly.

Chapter 4 studied the relationship between the adsorbed species, the presence of O_2 in solution and pH. First, it was observed that the reduction of oxide in $KClO_4$ occurred at more negative potentials due to a local increase in pH; in a similar manner, steady state voltammograms for the oxygen reduction reaction appeared at potentials closer to the expected potentials for alkaline conditions. The ORR waves were shown to be affected by the presence of the adsorbed species formed in $KClO_4$ in a similar way as with other electrolytes: higher coverages inhibited the ORR. These results, along with the observations made in respect to the reactions being affected by local changes of pH, suggested that the adsorbed oxygen species observed by Perry and Denuault were

oxides formed during the rest, specifically, PtOH due to the low potentials used. It is believed that a smiliar effect would be observed when studying other *p*H dependent reactions, namely hydrogen evolution, hydrogen peroxide oxidation and reduction and oxygen evolution, etc.

In Chapter 4 it was also observed that the oxide formation region in alkaline and acidic conditions was not influenced by the presence of molecular oxygen, as reported elsewhere [52, 53]; in contrast, in neutral and unbuffered media, the oxide formation region was strongly affected by O_2, as reported by Perry and Denuault [1, 2]. These observations suggested that the adsorbed species were related to local changes in *p*H and not to the presence of O_2. Voltammograms recorded at high scan rate in O_2-saturated $KClO_4$ showed the presence of two oxidation peaks, the first one ascribed to the formation of the adsorbed oxygen species reported by Perry and Denuault, while the second one was ascribed to the formation of thicker oxides. By comparing the oxide formation region in different electrolytes, it was suggested that the first peak was related to the formation of oxides in alkaline conditions while the second peak was related to oxides being formed in more acidic media. This change in local *p*H is ascribed to the high production of OH^- during the ORR that can not be compensated by mass transport. In an anodic sweep, after the reduction of O_2, oxide formation occurs in a highly alkaline local environment, forming the first oxidation peak; after the OH^- is exhausted by either its diffusion or the production of H^+ during the oxidation itself, the second peak appears at potentials closer to acidic conditions. As future work, it is proposed to perform these experiments with a rotating disc electrode: the oxidation region in neutral and unbuffered media in the presence of O_2 should be mass transport dependent due to the production of OH^-, this in turn would control the relative magnitude of both oxidation peaks.

To probe for the presence of OH^-, hindered diffusion was exploited. This was done to minimise the current contribution of the ORR to the total current by decreasing the flux of oxygen. These experiments were designed to simulate a degassing process, where the bulk position would correspond to a fully aerated solution while the hindered position would simulate a degassed one. Experiments performed in highly acidic media were not

influenced by the different oxygen fluxes, confirming what other groups reported with flow cells and quartz crystal microbalance regarding the presence of O_2 not affecting Pt oxide formation [52, 53]. This is an important result, as it is the first time that this has been observed with the use of SECM; in addition, hindered diffusion allowed the experiment to be performed in the presence of O_2 at all times, contrary to the literature reports where the solution is changed before the stripping. These experiments can be generalised and used to study adsorbed species when a dissolved species with a similar redox potential is present; a short electrode-substrate separation would decrease the contibution of the diffusion controlled species to the overall current.

Voltammograms in $KClO_4$ were shown to be strongly affected by the tip-substrate distance. The oxide formation region in the hindered position showed the presence of a diffusion controlled oxidation wave that was affected by the amount of OH^- produced and the tip-substrate distance. Although no direct confirmation exists, this wave is consistent with the oxidation of OH^- that occurs in slightly alkaline conditions [90]; a quick calculation showed that the local *p*H was about 9. More importantly, the voltammograms seemed affected by the tip-substrate distance; the magnitude of the two oxidation peaks changed with distance, and in the hindered position, only one continuous peak appeared along with the OH^- oxidation wave. This change in the oxide formation region is ascribed to different mass transport regimes; in the bulk, a high amount of OH^- can diffuse away from the electrode, producing two oxidation peaks, while in the hindered position the OH^- formed is trapped between the substrate and the electrode, greatly increasing the local *p*H and producing a continuous oxidation peak that would correspond to oxide being formed in alkaline conditions. Overall, these experiments show evidence that the adsorbed oxygen species observed by Perry and Denuault, are in fact oxides formed in alkaline conditions. Even though the results strongly suggest that the oxides are PtOH, spectroscopic evidence is needed and is proposed as future work. It is important to state that although this methodology was designed to be used with the specific conditions of this work, it can be used to study any adsorbed species when their redox potential is similar to that of species in solution.

Chapter 5 focused on the use of sampled current voltammetry to study the oxygen reduction reaction and adsorbed species. First, SCVs of Pt oxides were obtained, observing that the voltammograms were peak-shaped, as opposed to the sigmoidal waves observed when studying reactions of species in solution [8]. This suggested that SCVs for the ORR with an oxidised electrode would show a peak at short times, as the reduction of the oxide would contribute more to the current. This was observed when using high oxide coverages: normalisation to obtain an apparent number of electrons showed a value higher than 4, similar to what was observed by Perry and Denuault, supporting the idea of the adsorbed oxygen species being an oxide. After subtracting SCVs in the absence of O_2 and in electrolytes with extreme pH, n_{app} remained constant independently of the sampling time. In neutral and unbuffered media, the subtraction was not possible due to the differences in local pH when working in the presence and absence of O_2. This methodology opens up the posibility of decoupling adsorbed and dissolved species with sampled current voltammetry, where short sampling times would enhance the current contribution of any adspecies present, while long sampling times would ensure the steady state response of the diffusion controlled species.

Chapter 5 also introduces a kinetic analysis equivalent to the Koutecky-Levich approach. Noting that the mass transfer coefficient varies in transient conditions, equivalent Levich plots were constructed with current transients and transformed into Koutecky-Levich plots by plotting i^{-1} against k_m^{-1}. Extrapolation to the Y axis allowed for the determination of kinetic currents for each potential step; this in turn allowed for the construction of Tafel plots where the values of the Tafel slopes obtained were similar to the reported ones for the ORR. Perry and Denuault proposed the fitting of an equation to obtain kinetic parameters with microelectrode SCVs [20]. Compared to their methodology, the Koutecky-Levich approach does not depend on a complicated equation and is easier to implement, as the methodology is essentially the same as when using RDE. Furthermore, it can be used with any mass transport technique, provided the electrode is uniformly accessible; here, this was ensured by using timescales where planar diffusion dominated.

The last section of Chapter 5 and of this work, tries to give mathematical support

to the observation made previously regarding the SCVs for oxides being peak-shaped. As formation and reduction of Pt oxides are complicated reactions, it was decided to assume simpler conditions, specifically, that the redox species do not desorb and are quasi reversible, that the reaction follows a first order process and that the rate constant follows Butler-Volmer kinetics. With this assumptions, an analytical solution for the transient response of the coverage was obtained and turned into charge and current. The obtained sampled current voltammograms showed a Gaussian peak where its potential depended on the sampling time, while the sampled charge voltacoulograms showed sigmoidal waves. For the simple reaction studied here, kinetic information can be extracted by extrapolating the current transients to $t = 0$. It is proposed to convert SCVs into logarithmic SCVs, that is, plotting $\ln(i)$ against E; this is visually more powerful as kinetics limitations are shown as a linear regime. Although the system studied here is simple, it is believed that it can be improved by the addition of charging current and solution resistance to the differential equation, as well as including the possibility of different isotherms; this is left as future work.

Overall, in this work, strong evidence was shown that the adsorbed oxygen species observed by Perry and Denuault are in fact oxides formed at a higher local pH. Methodologies to obtain kinetic information from sampled current voltammograms of species in solution and adsorbed species were also proposed. It is believed that the work presented here can influence the way electrocatalysis is studied; as this is normally done with the use of steady-state techniques, the effect of adsorbed species is generally ignored. The main contributions of this work are listed below.

- Chapter 3: Reduction of oxygenated species at high rates of mass transport.
  - The use of electrodes with high rates of mass transport where the assumption of n_{app} to be constant is valid.
  - The use of a stripping voltammetric technique to obtain the charge of adsorption from purely experimental results.
- Chapter 4: Interaction between adsorbed oxygen species, O_2 and pH.
  - The voltammograms obtained in neutral media are shifted to alkaline po-

tentials due to local changes of pH.

- O_2 does not affect Pt oxide formation and reduction.
- Under hindered conditions and in neutral unbuffered media, a diffusion controlled oxidation wave appears that is ascribed to OH^- oxidation.
- The adsorbed oxygen species are oxides formed in an alkaline environment.

- Chapter 5: Sampled current voltammetry.
  - The SCV of the reduction of Pt oxides is peak-shaped.
  - The SCV for the ORR shows a peak at short sampling times due to the reduction of the oxides contributing to the current.
  - An equivalent Koutecky-Levich analysis can be used with sampled current voltammograms provided planar diffusion controls the current.
  - An analytical solution to SCV of adsorbed species was derived.

Bibliography

[1] S. C. Perry and G. Denuault, "Transient study of the oxygen reduction reaction on reduced pt and pt alloys microelectrodes: evidence for the reduction of pre-adsorbed oxygen species linked to dissolved oxygen," *Physical Chemistry Chemical Physics*, vol. 17, no. 44, pp. 30005–30012, 2015.

[2] S. C. Perry and G. Denuault, "The oxygen reduction reaction (ORR) on reduced metals: evidence for a unique relationship between the coverage of adsorbed oxygen species and adsorption energy," *Physical Chemistry Chemical Physics*, vol. 18, no. 15, pp. 10218–10223, 2016.

[3] S. C. Perry, *Transient Studies at Microelectrodes*. PhD thesis, University of Southampton, 2015.

[4] D. Pletcher and S. Sotiropoulos, "A study of cathodic oxygen reduction at platinum using microelectrodes," *Journal of Electroanalytical Chemistry*, vol. 356, pp. 109–119, sep 1993.

[5] S. Chen and A. Kucernak, "Electrocatalysis under conditions of high mass transport rate: oxygen reduction on single submicrometer-sized pt particles supported on carbon," *The Journal of Physical Chemistry B*, vol. 108, pp. 3262–3276, mar 2004.

[6] D. Pletcher, *A First Course in Electrode Processes*. The Royal Society of Chemistry, 2009.

[7] R. J. Forster, "Microelectrodes: new dimensions in electrochemistry," *Chemical Society Reviews*, vol. 23, no. 4, p. 289, 1994.

[8] A. J. Bard and L. R. Faulkner, *Electrochemical Methods: Fundamentals and Applications*. Wiley: New York, 2001.

[9] G. Denuault, M. V. Mirkin, and A. J. Bard, "Direct determination of diffusion coefficients by chronoamperometry at microdisk electrodes," *Journal of Electroanalytical Chemistry and Interfacial Electrochemistry*, vol. 308, pp. 27–38, jun 1991.

[10] M. Sosna, *Oxygen reduction at microelectrodes: application to the dissolved oxygen sensor for in situ oceanography measurements*. PhD thesis, University of Southampton, 2006.

[11] N. A. Abass, *Electrodeposition of metallic and semiconducting nanocentres*. PhD thesis, University of Southampton, 2014.

[12] D. Shoup and A. Szabo, "Chronoamperometry at an ensemble of microdisk electrodes," *Journal of Electroanalytical Chemistry and Interfacial Electrochemistry*, vol. 160, pp. 19–26, jan 1984.

[13] P. J. Mahon and K. B. Oldham, "Diffusion-controlled chronoamperometry at a disk electrode," *Analytical Chemistry*, vol. 77, pp. 6100–6101, sep 2005.

[14] S. Chen and A. Kucernak, "The voltammetric response of nanometer-sized carbon electrodes," *The Journal of Physical Chemistry B*, vol. 106, pp. 9396–9404, sep 2002.

[15] J. Chen and K. Aoki, "Overestimation of heterogeneous rate constants of hexacyanoferrate at nanometer-sized ultramicroelectrodes," *Electrochemistry Communications*, vol. 4, pp. 24–29, jan 2002.

[16] D. Li, C. Lin, C. Batchelor-McAuley, L. Chen, and R. G. Compton, "Tafel analysis in practice," *Journal of Electroanalytical Chemistry*, vol. 826, pp. 117–124, oct 2018.

[17] I. Streeter and R. G. Compton, "Mass transport corrected tafel analysis of voltammetric waves: When can it be applied?," *Electrochimica Acta*, vol. 52, pp. 4305–4311, mar 2007.

[18] M. V. Mirkin and A. J. Bard, "Simple analysis of quasi-reversible steady-state voltammograms," *Analytical Chemistry*, vol. 64, pp. 2293–2302, oct 1992.

[19] J. L. Conyers and H. S. White, "Electrochemical characterization of electrodes with submicrometer dimensions," *Analytical chemistry*, vol. 72, no. 18, pp. 4441–4446, 2000.

[20] S. C. Perry, L. M. A. Shandoudi, and G. Denuault, "Sampled-current voltammetry at microdisk electrodes: Kinetic information from pseudo steady state voltammograms," *Analytical Chemistry*, vol. 86, pp. 9917–9923, sep 2014.

[21] K. B. Oldham, J. C. Myland, C. G. Zoski, and A. M. Bond, "Kinetic parameters from steady-state voltammograms at microdisc electrodes," *Journal of Electroanalytical Chemistry and Interfacial Electrochemistry*, vol. 270, pp. 79–101, oct 1989.

[22] A. J. Bard and M. V. Mirkin, *Scanning Electrochemical Microscopy*. CRC Press, 2012.

[23] J. L. Amphlett and G. Denuault, "Scanning electrochemical microscopy (SECM): an investigation of the effects of tip geometry on amperometric tip response," *The Journal of Physical Chemistry B*, vol. 102, pp. 9946–9951, dec 1998.

[24] C. Lefrou and R. Cornut, "Analytical expressions for quantitative scanning electrochemical microscopy (SECM)," *ChemPhysChem*, vol. 11, pp. 547–556, jan 2010.

[25] M. V. Mirkin, T. C. Richards, and A. J. Bard, "Scanning electrochemical microscopy. 20. steady-state measurements of the fast heterogeneous kinetics in the ferrocene/acetonitrile system," *The Journal of Physical Chemistry*, vol. 97, pp. 7672–7677, jul 1993.

[26] R. D. Martin and P. R. Unwin, "Theory and experiment for the substrate generation/tip collection mode of the scanning electrochemical microscope: application as an approach for measuring the diffusion coefficient ratio of a redox couple," *Analytical Chemistry*, vol. 70, pp. 276–284, jan 1998.

[27] C. M. Sánchez-Sánchez, J. Rodríguez-López, and A. J. Bard, "Scanning electrochemical microscopy. 60. quantitative calibration of the SECM substrate generation/tip collection mode and its use for the study of the oxygen reduction mechanism," *Analytical Chemistry*, vol. 80, pp. 3254–3260, may 2008.

[28] Y.-J. Deng, G. K. H. Wiberg, A. Zana, and M. Arenz, "On the oxygen reduction reaction in phosphoric acid electrolyte: Evidence of significantly increased inhibition at steady state conditions," *Electrochimica Acta*, vol. 204, pp. 78–83, jun 2016.

[29] N. Garcia-Araez, V. Climent, E. Herrero, J. Feliu, and J. Lipkowski, "Thermodynamic studies of chloride adsorption at the Pt(111) electrode surface from 0.1 M $HClO_4$ solution," *Journal of Electroanalytical Chemistry*, vol. 576, pp. 33–41, feb 2005.

[30] I. Katsounaros, J. C. Meier, and K. J. Mayrhofer, "The impact of chloride ions and the catalyst loading on the reduction of H_2O_2 on high-surface-area platinum catalysts," *Electrochimica Acta*, vol. 110, pp. 790–795, nov 2013.

[31] D. Chen, Q. Tao, L. W. Liao, S. X. Liu, Y. X. Chen, and S. Ye, "Determining the active surface area for various platinum electrodes," *Electrocatalysis*, vol. 2, pp. 207–219, may 2011.

[32] O. Diaz-Morales, T. J. P. Hersbach, C. Badan, A. C. Garcia, and M. T. M. Koper, "Hydrogen adsorption on nano-structured platinum electrodes," *Faraday Discussions*, vol. 210, pp. 301–315, 2018.

[33] L. W. Liao, M. F. Li, J. Kang, D. Chen, Y.-X. Chen, and S. Ye, "Electrode reaction induced pH change at the Pt electrode/electrolyte interface and its impact on electrode processes," *Journal of Electroanalytical Chemistry*, vol. 688, pp. 207–215, jan 2013.

[34] T. Biegler, D. Rand, and R. Woods, "Limiting oxygen coverage on platinized platinum: Relevance to determination of real platinum area by hydrogen adsorption," *Journal of Electroanalytical Chemistry and Interfacial Electrochemistry*, vol. 29, pp. 269–277, feb 1971.

[35] I. Katsounaros, W. B. Schneider, J. C. Meier, U. Benedikt, P. U. Biedermann, A. A. Auer, and K. J. J. Mayrhofer, "Hydrogen peroxide electrochemistry on platinum: towards understanding the oxygen reduction reaction mechanism," *Physical Chemistry Chemical Physics*, vol. 14, no. 20, p. 7384, 2012.

[36] E. J. Coleman and A. C. Co, "The complex inhibiting role of surface oxide in the oxygen reduction reaction," *ACS Catalysis*, vol. 5, pp. 7299–7311, nov 2015.

[37] Y.-J. Deng, M. Arenz, and G. K. Wiberg, "Equilibrium coverage of OH ad in correlation with platinum catalyzed fuel cell reactions in $HClO_4$," *Electrochemistry Communications*, vol. 53, pp. 41–44, apr 2015.

[38] N.-T. Suen, S.-F. Hung, Q. Quan, N. Zhang, Y.-J. Xu, and H. M. Chen, "Electrocatalysis for the oxygen evolution reaction: recent development and future perspectives," *Chemical Society Reviews*, vol. 46, no. 2, pp. 337–365, 2017.

[39] M. Alsabet, M. Grden, and G. Jerkiewicz, "Comprehensive study of the growth of thin oxide layers on Pt electrodes under well-defined temperature, potential, and time conditions," *Journal of Electroanalytical Chemistry*, vol. 589, pp. 120–127, apr 2006.

[40] N. M. Marković, T. J. Schmidt, B. N. Grgur, H. A. Gasteiger, R. J. Behm, and P. N. Ross, "Effect of temperature on surface processes at the Pt(111)-liquid interface: hydrogen adsorption, oxide formation, and CO oxidation," *The Journal of Physical Chemistry B*, vol. 103, pp. 8568–8577, oct 1999.

[41] S. Strbac, "The effect of pH on oxygen and hydrogen peroxide reduction on polycrystalline Pt electrode," *Electrochimica Acta*, vol. 56, pp. 1597–1604, jan 2011.

[42] H. Y. H. Chan, S. Zou, and M. J. Weaver, "Mechanistic differences between electrochemical and gas-phase thermal oxidation of platinum-group transition metals as discerned by surface-enhanced raman spectroscopy," *The Journal of Physical Chemistry B*, vol. 103, pp. 11141–11151, dec 1999.

[43] H. S. Casalongue, S. Kaya, V. Viswanathan, D. J. Miller, D. Friebel, H. A. Hansen, J. K. Nørskov, A. Nilsson, and H. Ogasawara, "Direct observation of the oxy-

genated species during oxygen reduction on a platinum fuel cell cathode," *Nature Communications*, vol. 4, dec 2013.

[44] M. Wakisaka, H. Suzuki, S. Mitsui, H. Uchida, and M. Watanabe, "Increased oxygen coverage at Pt-Fe alloy cathode for the enhanced oxygen reduction reaction studied by EC-XPS," *The Journal of Physical Chemistry C*, vol. 112, pp. 2750–2755, feb 2008.

[45] M. Wakisaka, H. Suzuki, S. Mitsui, H. Uchida, and M. Watanabe, "Identification and quantification of oxygen species adsorbed on Pt(111) single-crystal and polycrystalline Pt electrodes by photoelectron spectroscopy," *Langmuir*, vol. 25, pp. 1897–1900, feb 2009.

[46] D. E. Icenhower, H. B. Urbach, and J. H. Harrison, "Use of the potential-step method to measure surface oxides," *Journal of The Electrochemical Society*, vol. 117, no. 12, p. 1500, 1970.

[47] G. Jerkiewicz, G. Vatankhah, J. Lessard, M. P. Soriaga, and Y.-S. Park, "Surface-oxide growth at platinum electrodes in aqueous H_2SO_4: Reexamination of its mechanism through combined cyclic-voltammetry, electrochemical quartz-crystal nanobalance, and Auger electron spectroscopy measurements," *Electrochimica Acta*, vol. 49, pp. 1451–1459, apr 2004.

[48] G. K. Wiberg and M. Arenz, "Establishing the potential dependent equilibrium oxide coverage on platinum in alkaline solution and its influence on the oxygen reduction," *Journal of Power Sources*, vol. 217, pp. 262–267, nov 2012.

[49] T. Biegler, "An electrochemical and electron microscopic study of activation and roughening of platinum electrodes," *Journal of The Electrochemical Society*, vol. 116, no. 8, p. 1131, 1969.

[50] Y. Huang, F. T. Wagner, J. Zhang, and J. Jorn, "On the nature of platinum oxides on carbon-supported catalysts," *Journal of Electroanalytical Chemistry*, vol. 728, pp. 112–117, aug 2014.

[51] B. E. Conway, B. Barnett, H. Angerstein-Kozlowska, and B. V. Tilak, "A surface-electrochemical basis for the direct logarithmic growth law for initial stages of extension of anodic oxide films formed at noble metals," *The Journal of Chemical Physics*, vol. 93, pp. 8361–8373, dec 1990.

[52] A. Kongkanand and J. M. Ziegelbauer, "Surface platinum electrooxidation in the presence of oxygen," *The Journal of Physical Chemistry C*, vol. 116, pp. 3684–3693, jan 2012.

[53] Y. Liu, M. Mathias, and J. Zhang, "Measurement of platinum oxide coverage in a proton exchange membrane fuel cell," *Electrochemical and Solid-State Letters*, vol. 13, no. 1, p. B1, 2010.

[54] G. A. Attard, A. Brew, K. Hunter, J. Sharman, and E. Wright, "Specific adsorption of perchlorate anions on Pt{hkl} single crystal electrodes," *Phys. Chem. Chem. Phys.*, vol. 16, no. 27, pp. 13689–13698, 2014.

[55] A. Zolfaghari, "Elucidation of the effects of competitive adsorption of Cl-and Br-ions on the initial stages of Pt surface oxidation by means of electrochemical nanogravimetry," *Electrochimica Acta*, vol. 47, pp. 1173–1187, feb 2002.

[56] B. R. Shrestha, E. Tada, and A. Nishikata, "Effect of chloride on platinum dissolution," *Electrochimica Acta*, vol. 143, pp. 161–167, oct 2014.

[57] P. P. Lopes, D. Tripkovic, P. F. Martins, D. Strmcnik, E. A. Ticianelli, V. R. Stamenkovic, and N. M. Markovic, "Dynamics of electrochemical Pt dissolution at atomic and molecular levels," *Journal of Electroanalytical Chemistry*, vol. 819, pp. 123–129, jun 2018.

[58] K. Shinozaki, J. W. Zack, R. M. Richards, B. S. Pivovar, and S. S. Kocha, "Oxygen reduction reaction measurements on platinum electrocatalysts utilizing rotating disk electrode technique i. impact of impurities, measurement protocols and applied corrections," *Journal of The Electrochemical Society*, vol. 162, no. 10, pp. F1144–F1158, 2015.

[59] L. Jacobse, S. J. Raaijman, and M. T. M. Koper, "The reactivity of platinum microelectrodes," *Physical Chemistry Chemical Physics*, vol. 18, no. 41, pp. 28451–28457, 2016.

[60] J. Zhang, ed., *PEM Fuel Cell Electrocatalysts and Catalyst Layers*. Springer London, 2008.

[61] C. M. Zalitis, D. Kramer, and A. R. Kucernak, "Electrocatalytic performance of fuel cell reactions at low catalyst loading and high mass transport," *Physical Chemistry Chemical Physics*, vol. 15, no. 12, p. 4329, 2013.

[62] M. Obradović, B. Grgur, and L. Vračar, "Adsorption of oxygen containing species and their effect on oxygen reduction on Pt3Co electrode," *Journal of Electroanalytical Chemistry*, vol. 548, pp. 69–78, may 2003.

[63] I. Katsounaros, W. B. Schneider, J. C. Meier, U. Benedikt, P. U. Biedermann, A. Cuesta, A. A. Auer, and K. J. J. Mayrhofer, "The impact of spectator species on the interaction of H_2O_2 with platinum – implications for the oxygen reduction reaction pathways," *Physical Chemistry Chemical Physics*, vol. 15, no. 21, p. 8058, 2013.

[64] A. M. Gmez-Marn, R. Rizo, and J. M. Feliu, "Oxygen reduction reaction at Pt single crystals: a critical overview," *Catalysis Science & Technology*, vol. 4, no. 6, pp. 1685–1698, 2014.

[65] A. M. Gmez-Marn and J. M. Feliu, "Oxygen reduction at platinum electrodes: The interplay between surface and surroundings properties," *Current Opinion in Electrochemistry*, mar 2018.

[66] C. Zhang, F.-R. F. Fan, and A. J. Bard, "Electrochemistry of oxygen in concentrated NaOH solutions: Solubility, diffusion coefficients, and superoxide formation," *Journal of the American Chemical Society*, vol. 131, pp. 177–181, jan 2009.

[67] N. Ramaswamy and S. Mukerjee, "Fundamental mechanistic understanding of electrocatalysis of oxygen reduction on Pt and non-Pt surfaces: Acid versus alka-

line media," *Advances in Physical Chemistry*, vol. 2012, pp. 1–17, mar 2012.

[68] F. Gao, Y. Yang, J. Liu, and H. Shao, "Method for preparing a novel type of Ptcarbon fiber disk ultramicroelectrode," *Ionics*, vol. 16, pp. 45–50, apr 2009.

[69] H. M. Yasin, G. Denuault, and D. Pletcher, "Studies of the electrodeposition of platinum metal from a hexachloroplatinic acid bath," *J. Electroanal. Chem.*, vol. 633, no. 2, pp. 327–332, 2009.

[70] P. Actis, S. Tokar, J. Clausmeyer, B. Babakinejad, S. Mikhaleva, R. Cornut, Y. Takahashi, A. López Córdoba, P. Novak, A. I. Shevchuck, J. A. Dougan, S. G. Kazarian, P. V. Gorelkin, A. S. Erofeev, I. V. Yaminsky, P. R. Unwin, W. Schuhmann, D. Klenerman, D. A. Rusakov, E. V. Sviderskaya, and Y. E. Korchev, "Electrochemical nanoprobes for single-cell analysis," *ACS Nano*, vol. 8, no. 1, pp. 875–884, 2014.

[71] M. Sen, Y. Takahashi, Y. Matsumae, Y. Horiguchi, A. Kumatani, K. Ino, H. Shiku, and T. Matsue, "Improving the Electrochemical Imaging Sensitivity of Scanning Electrochemical Microscopy-Scanning Ion Conductance Microscopy by Using Electrochemical Pt Deposition," *Anal. Chem.*, vol. 87, no. 6, pp. 3484–3489, 2015.

[72] N. Nioradze, R. Chen, J. Kim, M. Shen, P. Santhosh, and S. Amemiya, "Origins of nanoscale damage to glass-sealed platinum electrodes with submicrometer and nanometer size," *Anal. Chem.*, vol. 85, no. 13, pp. 6198–6202, 2013.

[73] N. Wakabayashi, M. Takeichi, M. Itagaki, H. Uchida, and M. Watanabe, "Temperature-dependence of oxygen reduction activity at a platinum electrode in an acidic electrolyte solution investigated with a channel flow double electrode," *Journal of Electroanalytical Chemistry*, vol. 574, pp. 339–346, jan 2005.

[74] J. Colt, *Computation of Dissolved Gas Concentrations As Functions of Temperature, Salinity and Pressure*. Amer Fisheries Society, 1984.

[75] M. Sosna, G. Denuault, R. W. Pascal, R. D. Prien, and M. Mowlem, "Development of a reliable microelectrode dissolved oxygen sensor," *Sensors and Actuators B: Chemical*, vol. 123, pp. 344–351, apr 2007.

[76] M. Maci, J. Campia, E. Herrero, and J. Feliu, "On the kinetics of oxygen reduction on platinum stepped surfaces in acidic media," *Journal of Electroanalytical Chemistry*, vol. 564, pp. 141–150, mar 2004.

[77] A. Kuzume, E. Herrero, and J. M. Feliu, "Oxygen reduction on stepped platinum surfaces in acidic media," *Journal of electroanalytical chemistry*, vol. 599, no. 2, pp. 333–343, 2007.

[78] N. M. Markovic, H. A. Gasteiger, and P. N. Ross, "Oxygen reduction on platinum low-index single-crystal surfaces in sulfuric acid solution: Rotating ring-Pt(hkl) disk studies," *The Journal of Physical Chemistry*, vol. 99, pp. 3411–3415, mar 1995.

[79] J. Kibsgaard, Y. Gorlin, Z. Chen, and T. F. Jaramillo, "Meso-structured platinum thin films : active and stable electrocatalysts for the oxygen reduction reaction," *J. Am. Chem. Soc.*, vol. 134, pp. 7758–7765, 2012.

[80] E. J. Coleman, M. H. Chowdhury, and A. C. Co, "Insights into the oxygen reduction reaction activity of Pt/C and PtCu/C catalysts," *ACS Catal.*, vol. 5, no. 2, pp. 1245–1253, 2015.

[81] B. Geboes, J. Ustarroz, K. Sentosun, H. Vanrompay, A. Hubin, S. Bals, and T. Breugelmans, "Electrochemical behavior of electrodeposited nanoporous Pt catalysts for the oxygen reduction reaction," *ACS Catal.*, vol. 17, no. i, pp. 5856–5864, 2016.

[82] R. H. Wopschall and I. Shain, "Effects of adsorption of electroactive species in stationary electrode polarography," *Anal. Chem.*, vol. 39, no. 13, pp. 1514–1527, 1967.

[83] Y.-F. Yang and G. Denuault, "Scanning electrochemical microscopy (SECM) : study of the adsorption and desorption of hydrogen on platinum electrodes in Na_2SO_4 solution (pH = 7)," *Journal of Electroanalytical Chemistry*, vol. 418, pp. 99–107, nov 1996.

[84] D. Pletcher and S. Sotiropoulos, "Hydrogen adsorptiondesorption and oxide formationreduction on polycrystalline platinum in unbuffered aqueous solutions," *J. Chem. Soc., Faraday Trans.*, vol. 90, no. 24, pp. 3663–3668, 1994.

[85] P. Daubinger, J. Kieninger, T. Unmssig, and G. A. Urban, "Electrochemical characteristics of nanostructured platinum electrodes a cyclic voltammetry study," *Phys. Chem. Chem. Phys.*, vol. 16, no. 18, pp. 8392–8399, 2014.

[86] J. Rodríguez-López, M. A. Alpuche-Avilés, and A. J. Bard, "Interrogation of surfaces for the quantification of adsorbed species on electrodes: oxygen on gold and platinum in neutral media," *Journal of the American Chemical Society*, vol. 130, pp. 16985–16995, dec 2008.

[87] W. Sheng, Z. Zhuang, M. Gao, J. Zheng, J. G. Chen, and Y. Yan, "Correlating hydrogen oxidation and evolution activity on platinum at different pH with measured hydrogen binding energy," *Nature Communications*, vol. 6, jan 2015.

[88] B. Conway, "Electrochemical oxide film formation at noble metals as a surface-chemical process," *Progress in Surface Science*, vol. 49, pp. 331–452, aug 1995.

[89] A. J. J. Jebaraj, N. S. Georgescu, and D. A. Scherson, "Oxygen and hydrogen peroxide reduction on polycrystalline platinum in acid electrolytes: Effects of bromide adsorption," *The Journal of Physical Chemistry C*, vol. 120, pp. 16090–16099, apr 2016.

[90] M. E. Abdelsalam, G. Denuault, M. A. Baldo, C. Bragato, and S. Daniele, "Detection of hydroxide ions in aqueous solutions by steady-state voltammetry," *Electroanalysis*, vol. 13, pp. 289–294, mar 2001.

[91] E. Laviron, "General expression of the linear potential sweep voltammogram in the case of diffusionless electrochemical systems," *Journal of Electroanalytical Chemistry and Interfacial Electrochemistry*, vol. 101, pp. 19–28, jul 1979.

[92] J. J. ODea and J. G. Osteryoung, "Characterization of quasi-reversible surface processes by square-wave voltammetry," *Analytical Chemistry*, vol. 65, pp. 3090–3097, nov 1993.

[93] H. A. Heering, M. S. Mondal, and F. A. Armstrong, "Using the pulsed nature of staircase cyclic voltammetry to determine interfacial electron-transfer rates of adsorbed species," *Analytical Chemistry*, vol. 71, pp. 174–182, jan 1999.

[94] M. A. Mann and L. A. Bottomley, "Cyclic square wave voltammetry of surface-confined quasireversible electron transfer reactions," *Langmuir*, vol. 31, pp. 9511–9520, aug 2015.

[95] C. Montella, "Further investigation of the equivalence of staircase and linear scan voltammograms. III-averaged-current staircase voltammetry applied to electrochemical reactions involving adsorbed species," *Journal of Electroanalytical Chemistry*, vol. 808, pp. 348–361, jan 2018.

[96] R. J. Forster, "Reversibly adsorbed monolayers on microelectrodes: Effect of potential on the adsorption thermodynamics," *Analytical Chemistry*, vol. 68, pp. 3143–3150, jan 1996.

[97] H. O. Finklea and D. D. Hanshew, "Electron-transfer kinetics in organized thiol monolayers with attached pentaammine(pyridine)ruthenium redox centers," *Journal of the American Chemical Society*, vol. 114, pp. 3173–3181, apr 1992.

[98] R. J. Forster and L. R. Faulkner, "Electrochemistry of spontaneously adsorbed monolayers. equilibrium properties and fundamental electron transfer characteristics," *Journal of the American Chemical Society*, vol. 116, pp. 5444–5452, jun 1994.

[99] R. J. Forster, "Heterogeneous kinetics of metal- and ligand-based redox reactions within adsorbed monolayers," *Inorganic Chemistry*, vol. 35, pp. 3394–3403, jan 1996.